A Thesis Submitted for the Degree of PhD at the University of Warwick

http://go.warwick.ac.uk/wrap/57731

THE UNIVERSITY OF WARWICK

Library Declaration and Deposit Agreement

1. STUDENT DETAILS

Please complete the following:

Full name: David Charles John Higgins…………………………………………………………………

University ID number: 0852594…………………………………………………………………………

2. THESIS DEPOSIT

2.1 I understand that under my registration at the University, I am required to deposit my thesis with the University in BOTH hard copy and in digital format. The digital version should normally be saved as a single pdf file.

2.2 The hard copy will be housed in the University Library. The digital version will be deposited in the University's Institutional Repository (WRAP). Unless otherwise indicated (see 2.3 below) this will be made openly accessible on the Internet and will be supplied to the British Library to be made available online via its Electronic Theses Online Service (EThOS) service.
[At present, theses submitted for a Master's degree by Research (MA, MSc, LLM, MS or MMedSci) are not being deposited in WRAP and not being made available via EthOS. This may change in future.]

2.3 In exceptional circumstances, the Chair of the Board of Graduate Studies may grant permission for an embargo to be placed on public access to the hard copy thesis for a limited period. It is also possible to apply separately for an embargo on the digital version. (Further information is available in the *Guide to Examinations for Higher Degrees by Research*.)

2.4 *If you are depositing a thesis for a Master's degree by Research, please complete section (a) below. For all other research degrees, please complete both sections (a) and (b) below:*

(a) Hard Copy

I hereby deposit a hard copy of my thesis in the University Library to be made publicly available to readers (please delete as appropriate) EITHER immediately OR after an embargo period of ………..................... months/years as agreed by the Chair of the Board of Graduate Studies.

I agree that my thesis may be photocopied. YES /~~NO~~ (*Please delete as appropriate*)

(b) Digital Copy

I hereby deposit a digital copy of my thesis to be held in WRAP and made available via EThOS.

Please choose one of the following options:

EITHER My thesis can be made publicly available online. YES /~~NO~~ (*Please delete as appropriate*)

OR My thesis can be made publicly available only after…..[date] (Please give date)
YES / NO (*Please delete as appropriate*)

OR My full thesis cannot be made publicly available online but I am submitting a separately identified additional, abridged version that can be made available online.
YES / NO (*Please delete as appropriate*)

OR My thesis cannot be made publicly available online. YES / NO (*Please delete as appropriate*)

3. GRANTING OF NON-EXCLUSIVE RIGHTS

Whether I deposit my Work personally or through an assistant or other agent, I agree to the following:

Rights granted to the University of Warwick and the British Library and the user of the thesis through this agreement are non-exclusive. I retain all rights in the thesis in its present version or future versions. I agree that the institutional repository administrators and the British Library or their agents may, without changing content, digitise and migrate the thesis to any medium or format for the purpose of future preservation and accessibility.

4. DECLARATIONS

(a) I DECLARE THAT:

- I am the author and owner of the copyright in the thesis and/or I have the authority of the authors and owners of the copyright in the thesis to make this agreement. Reproduction of any part of this thesis for teaching or in academic or other forms of publication is subject to the normal limitations on the use of copyrighted materials and to the proper and full acknowledgement of its source.

- The digital version of the thesis I am supplying is the same version as the final, hard-bound copy submitted in completion of my degree, once any minor corrections have been completed.

- I have exercised reasonable care to ensure that the thesis is original, and does not to the best of my knowledge break any UK law or other Intellectual Property Right, or contain any confidential material.

- I understand that, through the medium of the Internet, files will be available to automated agents, and may be searched and copied by, for example, text mining and plagiarism detection software.

(b) IF I HAVE AGREED (in Section 2 above) TO MAKE MY THESIS PUBLICLY AVAILABLE DIGITALLY, I ALSO DECLARE THAT:

- I grant the University of Warwick and the British Library a licence to make available on the Internet the thesis in digitised format through the Institutional Repository and through the British Library via the EThOS service.

- If my thesis does include any substantial subsidiary material owned by third-party copyright holders, I have sought and obtained permission to include it in any version of my thesis available in digital format and that this permission encompasses the rights that I have granted to the University of Warwick and to the British Library.

5. LEGAL INFRINGEMENTS

I understand that neither the University of Warwick nor the British Library have any obligation to take legal action on behalf of myself, or other rights holders, in the event of infringement of intellectual property rights, breach of contract or of any other right, in the thesis.

Please sign this agreement and return it to the Graduate School Office when you submit your thesis.

Student's signature: [redacted]… Date: 09/06/2013

Dynamics and Statistical Features of Coherent Plasma Structures in the SOL of a Tokamak

by

David Higgins

Thesis

Submitted to the University of Warwick

for the degree of

Doctor of Philosophy

Department of Physics

December 2012

THE UNIVERSITY OF
WARWICK

Contents

List of Tables

List of Figures

Acknowledgments

I am most thankful for the support of my supervisor Bogdan Hnat, who has patiently guided me through my PhD journey.

I would also like to thank Andrew Kirk and Patrick Tamain for their support and collaboration, without which much of my progress could not have been made. Similarly, my thanks goes out to the MAST experiments and SOL-DIV team for insightful discussions.

I would like to thank everyone at CFSA for regular discussion of mathematical and computational problems, and in particular I would like to thank Chris Brady for access to his extensive knowledge of computational simulation.

Finally, I would like to acknowledge the support and encouragement from my friends and family, and thank Sian for all her love and support.

Declarations

I declare that the work presented in this thesis is my own except where stated otherwise, and was carried out at the University of Warwick during the period of October 2008 to December 2012, under the supervision of Dr. B. Hnat. The research reported here has not been submitted, either wholly or in part, at this or any other academic institution for admission to a higher degree. Some parts of the work reported in this thesis have been published in peer reviewed journals:

D Higgins, B Hnat, A Kirk, P Tamain, N Ben Ayed, and the MAST Team. *Determining advection mechanism of plasma filaments in the scrape-off layer of MAST.* Plasma Phys. Control. Fusion, 54(1):015002, 2012.

This publication covers some of the theory presented in chapter 2, and most of the results presented in chapters 3 and 5.

Abstract

Understanding surface erosion in tokamaks due to contact with hot plasma is critical in designing new high power devices. The propagation of the plasma through the scrape off layer (SOL) ultimately defines the spatio-temporal characteristics of this erosion, hence modelling of this region is an important area of research.

Transport in the SOL is attributed to advective motions of plasma blobs, for which the advective velocity is estimated in the literature. A new paradigm for comparing the theory of plasma blobs with experimental data is developed, which treats density and velocity data as sets of coherent structures via a peak detection algorithm. The phase difference of plasma density and radial velocity peaks take values depending on the dominating physics of the blob motion. Values of this phase difference are predicted in the interchange and drift wave cases for a strongly nonlinear plasma. Analysis of MAST data reveals interchange activity in the edge and SOL, and a phase structure typical of sheath limited models in the SOL.

A further application of the paradigm examines the blob velocity-density scaling $v \propto n^{\alpha}$. A new sheath limited model for blob advection with divertor density n_t constant gives $\alpha = 1$. Predictions in the zero parallel current case depend on the blob nonlinearity; we examine the dependency of α on the nonlinearity by solving the time independent equation of blob motion for a range of density profiles, finding $\alpha \sim 0.3$ for MAST nonlinearity strength. The α parameter is estimated statistically from MAST data, and it found to peak at $\alpha \sim 1$ near the last closed flux surface (LCFS) and fall to zero further from the plasma. The scaling behaviour is further examined using the TOKER code.

A numerical model, hTOKER, is developed. A subgrid model is employed that terminates the plasma at a chosen scale with defined spectral properties, which allows a physically accurate way to reduce resolution and computational burden. We examine sheath potential drop (SPD) and finite ion temperature (FTI) effects on SOL transport in the cases of constant (CTI) and flute (SI) n_t boundary conditions. For the advection of individual blobs, SPD effects that are stable in the SI case are found to be unstable in the CTI case, and FTI effects are found to be stabilising in all cases. SOL plasma simulations are used to examine the differences in particle-energy flux and peak phase difference using floating or plasma potential. Floating potential overestimates flux by a factor 2, and shifts phase differences from 0° to $\sim -30°$. FTI effects are without cancellation from the gyro-viscous counterparts.

Abbreviations

SOL	Scrape off layer
LCFS	Last closed flux surface
MAST	Mega-amp spherical tokamak
FTI	Finite ion temperature
SI	Standard interchange
CTI	Constant target interchange
SPD	Sheath potential drop
MCF	Magnetic confinement fusion
RMS	Root mean squared
tRMS	Thresholded root mean squared
RP	Reciprocating probe
MPI	Message passing interface

Chapter 1

Introduction

Since the industrial revolution mankind has searched for increasingly effective ways to supply the energy needed by increasingly effective machines, and toward the end of the 20th century the focus has progressively shifted toward machines that are economical and sources of power that are clean; it has become clear that the resources our environment provides are finite and will not be available in the future. In this context, nuclear fusion has become a holy grail of power sources as the abundance and efficiency of the fuel is orders of magnitude greater than any other known source, and the environmental impact comparatively small.

There are many approaches to achieve nuclear fusion, all of which rely on different ways to accelerate nuclei to high enough velocities, so that their stopping distance is within the range of influence of the strong nuclear force. It is thermonuclear fusion, in which the nuclei achieve a high relative velocity by virtue of being part of a high temperature gas that this thesis pertains to.

The principle reaction in question is between a deuterium and tritium nucleus; with enough relative velocity, the nuclei will be able to overcome the electrostatic repulsion of their positive charges and the strong nuclear force will invoke the following reaction:

$$D_1^2 + T_1^3 \rightarrow He_2^4(3.5MeV) + n_0^1(14.1MeV). \tag{1.1}$$

Deuterium is naturally occurring in sea water, and tritium may be bred for example via the reaction

$$Li_3^6 + n_0^1 \rightarrow T_1^3 + He_2^4. \tag{1.2}$$

One litre of sea water contains 0.033g of deuterium or $\sim 10^{22}$ deuterium atoms accounting for 0.015% of the water, which when fused equates to an energy released in the form of neutrons of $22.6GJ$, compared to the energy stored in a looter of crude oil which is $\sim 0.38GJ$.

The reaction (1.1) is selected in the context of thermonuclear fusion because it achieves the highest peak cross-section of nuclear reactions. In a plasma, collisionality is not a monotonic function of temperature and has a maximum peak value, and will reduce for higher temperatures, due to Landau damping [Wesson, 1987; Landau, 1946].

1.1 Plasma and the Tokamak

At the temperatures needed to achieve thermonuclear fusion, electrons will have too much energy to be bound to their ions (nuclei) and a new state of matter known as a plasma, distinguished by the new electromagnetic properties acquired as compared to the atomic state, is created. In order to reach, and sustain these temperatures the plasma must be well isolated from the local ambient temperature since any contact will quickly dissipate these temperatures. One approach would be to fuse most of the nuclear fuel in a time shorter than the thermal transfer rate to the environment, as is the approach in inertial confinement fusion and some nuclear weapons. Another approach to confinement takes advantage of the electromagnetic response of the plasma, by confining the plasma in a magnetic field so that the Lorentz force

$$\vec{F}_L = q_s\vec{E} + q_s\vec{v}_s \times \vec{B}, \tag{1.3}$$

with subscript s denoting species (proton,electron,ion...) causes individual particle trajectories to become orbital in the plane perpendicular to the magnetic field $\vec{B}$. This significantly reduces the collision rates in the perpendicular direction compared to the unmagnetised case, and by constructing the magnetic field that closes on itself the system becomes effectively confined. The simplest structure of isolated magnetic fields that can be constructed is the torus; a device that uses this type of magnetic field to confine plasma is called a tokamak an acronym given to it by the Soviet inventors Igor Tamm and Andrei Sakharov. Practical tokamaks are of course much more complicated than the above description, and in particular there must be magnetic field pointing in both of the angular directions of the torus, however, this description will serve until expanded upon later in this thesis.

1.1.1 Quasi-neutrality

The high mobility of electrons in a plasma allow them to respond to any electric field, which makes plasmas highly conductive and act to maintain a state of volume neutrality. More precisely, if we consider a plasma of electrons and protons (a hydrogen plasma), we may write the Poisson equation as

$$\vec{\nabla}^2\phi = \frac{e}{\epsilon_0}\left(n_e - n_i\right), \tag{1.4}$$

which informs us of the potential given number densities of electrons n_e and protons n_i. Electrons have a high mobility due to their small mass, and their density will be governed by

$$n_e = n_0 \exp\left(\frac{e\phi}{k_B T_e}\right), \tag{1.5}$$

a result of the unmagnetised electron momentum equation in the inertia-less limit, which shall be derived in section 1.2.2. Then, equation (1.4) becomes the non-liner relation

$$\vec{\nabla}^2\phi = \frac{en_0}{\epsilon_0}\left(\exp\left(\frac{e\phi}{k_B T_e}\right) - 1\right), \tag{1.6}$$

where the protons are relatively immobile and retain the background density distribution n_0. Equation (1.6) can be simplified in the limit of high temperature so that for $e\phi \ll k_B T_e$

$$\vec{\nabla}^2\phi = \frac{en_0}{\epsilon_0}\left(\frac{e\phi}{k_B T_e}\right), \tag{1.7}$$

where the solution for ϕ is exponential with the length scale known as the Debye length

$$\lambda_D = \sqrt{\frac{\epsilon_0 k_B T_e}{n_0 e^2}}, \tag{1.8}$$

which gives the e-folding length at which electrostatic potential due to charge density dies away. Scales much larger than this length can be considered neutral plasmas - this is quasi-neutrality.

1.1.2 Particle Drifts

Charged particles with finite velocity in the presence of a magnetic field follow a circular trajectory, which is easily shown by taking the Lorentz force in the limit of zero electric field [Miyamoto, 2007], and the magnetic field in the $\hat{z}$ direction,

$$\frac{dv_x}{dt} = \frac{q}{m}v_y B_z, \tag{1.9}$$

$$\frac{dv_y}{dt} = -\frac{q}{m} v_x B_z, \tag{1.10}$$

and via substitution,

$$\frac{d^2 v_y}{dt^2} = -\left(\frac{qB_z}{m}\right)^2 v_y, \tag{1.11}$$

$$\frac{d^2 v_x}{dt^2} = -\left(\frac{qB_z}{m}\right)^2 v_x, \tag{1.12}$$

which defines a harmonic motion, taking an arbitrary phase with $v_x = v_0 \sin(\omega t)$, we find $v_y = v_0 \cos(\omega t)$ with $\omega = \frac{qB_z}{m}$, where the solution is not related to an initial condition in x or y. In cylindrical coordinates with r the radial coordinate,

$$\frac{dr}{dt} = \frac{d}{dt}\sqrt{\cos^2 \omega t + \sin^2 \omega t} = 0, \tag{1.13}$$

and equations (1.9) and (1.10) become

$$r\frac{d^2 \cos\theta}{dt^2} = r\omega \frac{d \sin\theta}{dt}, \tag{1.14}$$

$$r\frac{d^2 \sin\theta}{dt^2} = -r\omega \frac{d \cos\theta}{dt}, \tag{1.15}$$

so that we find

$$\frac{d\theta}{dt} = \frac{d}{dt}\omega t = \omega. \tag{1.16}$$

This frequency is known as the cyclotron frequency, and is usually labelled ω_c.

Consider the dynamics of a charged particle under Lorentz force and an external force $\vec{F}_{ext}$

$$m\frac{d\vec{v}}{dt} = q\left(\vec{v} \times \vec{B}\right) + \vec{F}_{ext}, \tag{1.17}$$

and averaging over the fast gyro motion, with $\vec{F}_{ext}$ constant in time

$$m\left\langle \frac{d\vec{v}}{dt} \right\rangle \approx 0 = q\left(< \vec{v} > \times \vec{B}\right) + <\vec{F}_{ext}>, \tag{1.18}$$

The time derivative has been set to zero by assuming that $\vec{F}_{ext}$ causes an increase in velocity while $\vec{v} \cdot \vec{F}_{ext} > 0$, which is equal to the decrease in velocity while $\vec{v} \cdot \vec{F}_{ext} < 0$ in the direction of the force. Then $< \vec{v} >$ is the (time constant) guiding centre velocity, which we will label $\vec{v}_g$, which may be solved for by taking the cross product with $\vec{B}$

$$\vec{v}_g = \frac{<\vec{F}_{ext}> \times \vec{B}}{qB^2}; \tag{1.19}$$

such a velocity is known as a drift velocity, and when the force in question is due to an electric field, $\vec{F}_{ext} = q\vec{E}$, this drift velocity is known as the "E cross B drift", and $\vec{v}_E$ is not a function of charge. When the external force is a function of time, setting the time derivative to zero in (1.18) is of course invalid. In this context, the guiding centre approximation requires that the order of $\left\langle \frac{d\vec{F}ext}{dt} \right\rangle$ is the same as the order of $\left\langle \frac{d\vec{v}}{dt} \right\rangle$ in time, so that if

$$\vec{F}_{ext} \in \mathcal{O}(t) \tag{1.20}$$

then the LHS of (1.18), which is a derivative in t, is a constant ($\mathcal{O}(1)$), meaning we find another drift velocity

$$\vec{v}_g = \frac{\vec{F}_{ext} \times \vec{B}}{qB^2} - \frac{m}{qB^2}\frac{d\vec{v}_g}{dt} \times \vec{B}, \tag{1.21}$$

which is known as an inertial drift, and when the force is due to an electric field , the polarisation drift. This hierarchy continues for each order in time the external force possesses. A particular force to consider is the force due to gradients in magnetic field. Clearly, there will be a force directed down the slope of the magnetic field on the average of the gyro-period due to the imbalance of the Lorentz force on the approximately circular orbit. With

$$\vec{B}(x) = B_0\hat{z} + \frac{\partial B}{\partial x}x\hat{z} \tag{1.22}$$

the perpendicular components of the Lorentz force are

$$\vec{F}_x = q\vec{v}_y\left(B_0 + \frac{\partial B}{\partial x}x\right) \tag{1.23}$$

$$\vec{F}_y = -q\vec{v}_x\left(B_0 + \frac{\partial B}{\partial x}x\right) \tag{1.24}$$

and we have expressions for the (circular) gyration, so that

$$F_x = qv_0\cos\omega t\left(B_0 - \frac{v_0}{\omega}\frac{\partial B}{\partial x}\cos\omega t\right) \tag{1.25}$$

$$F_y = -qv_0\sin\omega t\left(B_0 + \frac{v_0}{\omega}\frac{\partial B}{\partial x}\cos\omega t\right) \tag{1.26}$$

given the period averages of the harmonic functions, we conclude that on time scales larger than the gyro-period there is zero net force in the y direction, and a net force in the x direction of

$$\langle F_x \rangle_\omega = -\frac{qv_0^2}{2\omega}\frac{\partial B}{\partial x} \tag{1.27}$$

which is typically written in terms of the thermal velocity $v_0 = v_{th} = \sqrt{\frac{\gamma T}{m}}$,

$$\langle F_x \rangle_\omega = -\frac{\gamma T}{2B}\frac{\partial B}{\partial x}. \tag{1.28}$$

This force, along with a force due to any gradient in magnetic field in the y direction will result in a guiding centre drift of the form specified in (1.19), which can be written as

$$\vec{v}_{\nabla B} = \frac{T}{qB}\frac{\vec{B} \times \vec{\nabla} B}{B^2} \tag{1.29}$$

with $\gamma = 1 + 2/f = 2$ for a system with two degrees of freedom f.

Another type of drift velocity, closely linked to 1.29, arises from a charged particle moving along a curved magnetic field. Such a particle will experience a centrifugal force of

$$\vec{F}_c = \frac{mv_\|^2}{R_c}\hat{r}, \tag{1.30}$$

where R_c is the radius of curvature. In conjunction with the pattern (1.19), the drift velocity due to curved magnetic fields (or simply curvature drift) is found as

$$\vec{v}_c = \frac{mv_\|^2}{qR_c}\frac{\hat{r} \times \vec{B}}{B^2}. \tag{1.31}$$

Under the approximation that the magnetic field is cylindrically symmetric, there is a common unification of magnetic gradient and curvature drifts. We consider a magnetic field of the form $\vec{B} = B_\theta(r)\hat{\theta}$, and an electrostatic vacuum Ohm's law giving $\vec{\nabla} \times \vec{B} = 0$, giving

$$\vec{\nabla} \times \vec{B} = \frac{1}{r}\frac{\partial}{\partial r} rB_\theta(r) = 0, \tag{1.32}$$

meaning that $rB_\theta(r)$ is a constant, or $B_\theta = \frac{BR_c}{r}$. Since this gives

$$\vec{\nabla}\vec{B} = -\frac{B}{R_c}\hat{r}, \tag{1.33}$$

the curvature drift (1.31), under these conditions, becomes

$$\vec{v}_c = \frac{T}{qB}\frac{\vec{B} \times \vec{\nabla}\vec{B}}{B^2}, \tag{1.34}$$

with the assumption of isotropic thermal velocities so that $T = \left\langle \frac{1}{2} m v_\perp^2 \right\rangle = \left\langle m v_\parallel^2 \right\rangle$.

1.2 Collective Description

A collective description of plasma is required in order to study the behaviour of the large numbers of particles present in fusion plasmas and their collective behaviours. The governing equations for single particles are the Lorentz force

$$m_s \frac{d\vec{v}_s}{dt} = q_s \left(\vec{v}_s \times \vec{B} + \vec{E} \right), \tag{1.35}$$

which governs the position and velocity of the particle, and Maxwell's equations,

$$\vec{\nabla} \cdot \vec{E} = \frac{\rho}{\epsilon_0}, \tag{1.36}$$

$$\vec{\nabla} \cdot \vec{B} = 0, \tag{1.37}$$

$$\vec{\nabla} \times \vec{E} = -\frac{\partial \vec{B}}{\partial t}, \tag{1.38}$$

$$\vec{\nabla} \times \vec{B} = \mu_0 \vec{J} + \mu_0 \epsilon_0 \frac{\partial \vec{E}}{\partial t}, \tag{1.39}$$

which govern the fields $\vec{E}$ and $\vec{B}$ generated by the charges and currents. To describe a multitude of particles each with a distinct $\vec{V}_i(t)$ and $\vec{X}_i(t)$ (a total of 6 dimensions of freedom for each particle), we write the contribution to a density distribution in this space as

$$N_i(\vec{x}, \vec{v}, t) = \delta(\vec{x} - \vec{X}_i(t)) \delta(\vec{v} - \vec{V}_i(t)), \tag{1.40}$$

where $\delta()$ is the Dirac delta function, and for a plasma species s (distinct mass and charge) the total density distribution is written

$$N_s(\vec{x}, \vec{v}, t) = \sum_{i=0}^{N_{0s}} N_i(\vec{x}, \vec{v}, t), \tag{1.41}$$

so that the charge and current densities may be written as

$$\rho = \sum_s q_s \int N_s(\vec{x}, \vec{v}, t) d^3v, \tag{1.42}$$

$$\vec{J} = \sum_s q_s \int N_s(\vec{x}, \vec{v}, t) \vec{v} d^3v. \tag{1.43}$$

1.2.1 Kinetic

A kinetic description of plasma describes the system using distribution functions in position space and time, and statistical approximations to describe effects generally called "collisions" due to their short range nature. Evaluating the time derivative of the particle density distribution,

$$\frac{\partial N_s}{\partial t} = \sum_{i=0}^{N_{0s}} \delta(\vec{x} - \vec{X}_i(t)) \frac{\partial}{\partial t} \delta(\vec{v} - \vec{V}_i(t)) + \sum_{i=0}^{N_{0s}} \delta(\vec{v} - \vec{V}_i(t)) \frac{\partial}{\partial t} \delta(\vec{x} - \vec{X}_i(t)), \tag{1.44}$$

where we may write

$$\frac{\partial}{\partial t} \delta(\vec{x} - \vec{X}_i(t)) = \left(\frac{\partial \delta(\vec{x} - \vec{X}_i(t))}{\partial \vec{x}} \right) \left(\frac{-\partial X_i(t)}{\partial t} \right), \tag{1.45}$$

$$\frac{\partial}{\partial t} \delta(\vec{v} - \vec{V}_i(t)) = \left(\frac{\partial \delta(\vec{v} - \vec{V}_i(t))}{\partial \vec{v}} \right) \left(\frac{-\partial V_i(t)}{\partial t} \right), \tag{1.46}$$

which combined with the property of the delta function

$$\delta(A - B)A = \delta(A - B)B, \tag{1.47}$$

allows us to write (1.44) as

$$\frac{\partial N_s}{\partial t} + \vec{v} \cdot \frac{\partial N_s}{\partial \vec{x}} + \frac{q_s}{m_s} \left(\vec{E} + \vec{v} \times \vec{B} \right) \cdot \frac{\partial N_s}{\partial \vec{v}} = 0, \tag{1.48}$$

which is the Klimontovich equation, describing the plasma down to the microscopic scale for the quantities $N_s, \vec{E}, \vec{B}$, which amounts to a kinetic description of the many body particle problem, and is completely intractable. We can write

$$N_s = f_s + \delta N_s, \tag{1.49}$$

$$\vec{E} = \vec{E} + \delta \vec{E}, \tag{1.50}$$

$$\vec{B} = \vec{B} + \delta \vec{B}, \tag{1.51}$$

where the quantities have had the microscopic parts due to short range interactions moved into a new term denoted by δ (not to be confused with the Dirac delta function). We define also an ensemble average $\langle\rangle_e$ which is sufficient to remove this microscopic part from these quantities,

$$\langle \delta N_s \rangle_e = \left\langle \delta \vec{E} \right\rangle_e = \left\langle \delta \vec{B} \right\rangle_e = 0, \tag{1.52}$$

and apply it to the Klimontovich equation, obtaining

$$\frac{\partial f_s}{\partial t} + \vec{v} \cdot \frac{\partial f_s}{\partial \vec{x}} + \frac{q_s}{m_s} \left(\vec{E} + \vec{v} \times \vec{B} \right) \cdot \frac{\partial f_s}{\partial \vec{v}} = - \left\langle \frac{q_s}{m_s} \left(\delta \vec{E} + \vec{v} \times \delta \vec{B} \right) \cdot \frac{\partial \delta N_s}{\partial \vec{v}} \right\rangle_e . \tag{1.53}$$

Equation (1.53) is often referred to as the Boltzmann equation for a plasma, in which the RHS represents the microscopic particle behaviour (often referred to simply as "collisions"), the treatment of which not only is highly difficult to classify and describe but also highly dependent on the specific physical system being described. Many statistical approximations must be made for a solution to be tractable leading to many forms of the collision term, each valid for a different type of plasma. When the RHS of (1.53) is set to zero, this is known as the Vlasov equation.

1.2.2 Two-Fluid

The description of a plasma in (1.53) may be dimensionally reduced by describing averaged values, known as moments, of the Boltzmann distribution f_s in (1.53), starting by rewriting as

$$\frac{\partial f_s}{\partial t} + \frac{\partial}{\partial \vec{x}} \cdot \vec{v} f_s + \frac{q_s}{m_s} \frac{\partial}{\partial \vec{v}} \cdot \left(\vec{E} + \vec{v} \times \vec{B} \right) f_s = C_s(f_s) \tag{1.54}$$

where velocity and force terms have been moved inside derivatives, and the microscopic fluctuations are written in the Boltzmann form $C_s(f_s) = \sum_{s'} C_{ss'}$ where only binary collisions are considered. In this it is assumed that x and v are independent variables, and the electromagnetic force is incompressible in velocity space. The process of writing the kinetic equation in terms of moments may be thought of as a more efficient representation of the distribution function. As an example, consider that f_s was Maxwelliean in each dimension; only 6 scalars as opposed to a 6 dimensional function are required to describe f_s. Intrinsic to this approach is the fact that for a truly general f_s, an infinite number of such moments will be required to fully expand f_s, which is an introduction to the problem of closure that will be expanded upon soon. Typically four moments of f_s are defined that have simple physical interpretations,

$$n_s = \int f_s d\vec{v}, \tag{1.55}$$

$$\vec{V}_s = \frac{1}{n_s}\int \vec{v} f_s d\vec{v}, \tag{1.56}$$

$$\boldsymbol{P}_s = \int m_s \vec{v} \otimes \vec{v} f_s d\vec{v}, \tag{1.57}$$

$$\vec{Q}_s = \int \frac{1}{2} m_s v^2 \vec{v} f_s d\vec{v}, \tag{1.58}$$

which are the particle density, mean particle velocity, stress tensor (describing the mean momentum flux) and energy density flux (describing the mean energy flux), respectively. Now we look for equations that govern these moment quantities, and in doing so we will assume that the distribution function is close to the maxwelliean, that is $f_s \propto e^{-v^2}$ such that $\int_{-\infty}^{\infty} \frac{\partial}{\partial \vec{v}} f_s = 0$. The zeroth moment equation is then generated by integrating (1.54) over the velocity coordinates $\vec{v}$ giving

$$\frac{\partial n_s}{\partial t} + \frac{\partial}{\partial \vec{x}} \cdot \left(n_s \vec{V}_s\right) = \int C_s d\vec{v}. \tag{1.59}$$

We see that the evolution equation for the zeroth moment depends on the value of the first moment. The first moment equation is generated by multiplying (1.54) by $m_s\vec{v}$ and integrating over $\vec{v}$

$$\frac{\partial}{\partial t} m_s n_s \vec{V}_s + \frac{\partial}{\partial \vec{x}} \cdot \boldsymbol{P}_s - q_s n_s \left(\vec{E} + \vec{V}_s \times \vec{B}\right) = \int m_s \vec{v} C_s d\vec{v}, \tag{1.60}$$

again we see that the evolution equation for the first moment depends on the value of the second moment, this pattern continues for all moment equations, and the final moment evolution equation we consider is for the second moment, which will require the value of the third moment, and is obtained by integrating (1.54) by $\frac{1}{2} m_s v_s^2$

$$\frac{\partial}{\partial t} \int \frac{1}{2} m_s v_s^2 f_s d\vec{v} + \vec{\nabla} \cdot \vec{Q}_s - q_s n_s \vec{E} \cdot \vec{V}_s = \int \frac{1}{2} m_s v_s^2 C_s d\vec{v}. \tag{1.61}$$

The first term in (1.61) is left unintegrated, because we do not have a definition for it at present. We define the velocity in the reference frame of the particle, $\vec{w}_s = \vec{v} - \vec{V}_s$, as it is relative to the mean particle velocity (i.e. the fluid velocity). Then, the stress and energy fluxes measured in this frame are

$$\boldsymbol{p}_s = \int m_s \vec{w}_s \otimes \vec{w}_s f_s d\vec{v}, \tag{1.62}$$

$$\vec{h}_s = \int m_s w_s^2 \vec{w}_s f_s d\vec{v}, \tag{1.63}$$

which are called the pressure tensor and heat flux, respectively, and the velocity $\vec{w}_s(\vec{v})$ is a random thermal motion so that $\int \vec{w}_s f_s d\vec{v} = 0$. The diagonal part of $\boldsymbol{p}_s$ are the ordinary 1D gas pressures, so that the scalar pressure is

$$p_s = \frac{1}{3}\,\mathrm{Tr}(\boldsymbol{p}_s), \tag{1.64}$$

and taking the inner product instead of the outer product in (1.62) yields an expression for the scalar pressure, which is related to the kinetic energy density

$$\frac{3}{2}p_s = \int \frac{1}{2}m_s w_s^2 f_s d\vec{v}, \tag{1.65}$$

and as such, (1.61) is written as

$$\frac{\partial}{\partial t}\left(\frac{3}{2}p_s + \frac{1}{2}m_s n_s V_s^2\right) + \vec{\nabla}\cdot\vec{Q}_s - q_s n_s \vec{E}\cdot\vec{V}_s = \int \frac{1}{2}m_s v_s^2 C_s d\vec{v}. \tag{1.66}$$

The billinear collision integrals define the quantities

$$\int C_s d\vec{v} = 0, \tag{1.67}$$

$$\int m_s \vec{v} C_s d\vec{v} = \vec{F}_s, \tag{1.68}$$

$$\int \frac{1}{2}m_s v_s^2 C_s d\vec{v} = W_s + \vec{V}_s\cdot\vec{F}_s, \tag{1.69}$$

which arise from conservation of particles, momentum and energy and F_s is the frictional force due to collisions, W_s the frictional heating. Using these relations, writing the stress tensor and energy flux density in terms of $\boldsymbol{p}_s$ and $\vec{h}_s$ and splitting the pressure tensor into scalar pressure p_s and a general viscosity tensor $\boldsymbol{\pi}_s$ (which governs the damping of velocity shear) equations (1.59),(1.60) and (1.66) are written

$$\frac{\partial n_s}{\partial t} + \vec{\nabla}\cdot\left(n_s\vec{V}_s\right) = 0, \tag{1.70}$$

$$m_s n_s\left(\frac{\partial}{\partial t} + \vec{V}_s\cdot\vec{\nabla}\right)\vec{V}_s + \vec{\nabla}p_s + \vec{\nabla}\cdot\boldsymbol{\pi}_s - q_s n_s\left(\vec{E} + \vec{V}_s\times\vec{B}\right) = \vec{F}_s, \tag{1.71}$$

$$\begin{aligned}&\tfrac{\partial}{\partial t}\left(\tfrac{3}{2}p_s + \tfrac{1}{2}m_s n_s V_s^2\right) + \vec{\nabla}\cdot\left(\left[\tfrac{5}{2}p_s + \tfrac{1}{2}m_s n_s V_s^2\right]\vec{V}_s\right)\\ &+\vec{\nabla}\cdot\vec{h}_s + \vec{\nabla}\cdot\left(\boldsymbol{\pi}_s\cdot\vec{V}_s\right) - q_s n_s\vec{E}\cdot\vec{V}_s = W_s + \vec{F}_s\cdot\vec{V}_s,\end{aligned} \tag{1.72}$$

which are the continuity equation, momentum equation and energy equation respectively. We may write (1.72) in terms of temperature rather than energy using (1.70) and (1.71), since the time derivative of the kinetic energy density may be written as

$$\begin{gathered}\frac{\partial}{\partial t}\frac{1}{2}m_s n_s V_s^2 = -\vec{\nabla} p_s \cdot \vec{V}_s - \left(\vec{\nabla}\cdot\boldsymbol{\pi}_s\right)\cdot\vec{V}_s + q_s n_s \vec{E}\cdot\vec{V}_s \\ +\vec{F}_s\cdot\vec{V}_s - \left[m_s n_s\left(\vec{V}_s\cdot\vec{\nabla}\right)\vec{V}_s\right]\cdot\vec{V}_s - \frac{1}{2}m_s V_s^2\left(\vec{\nabla}\cdot n_s\vec{V}_s\right), \qquad (1.73)\end{gathered}$$

which transforms (1.72), with another substitution of (1.70) into

$$\frac{3}{2}n_s\left(\frac{\partial}{\partial t} + \vec{V}_s\cdot\vec{\nabla}\right)T_s + p_s\vec{\nabla}\cdot\vec{V}_s + \pi : \vec{\nabla}\vec{V}_s + \vec{\nabla}\cdot\vec{h}_s = W_s, \qquad (1.74)$$

where we have made use of a definition of kinetic temperature $p_s = n_s T_s$, and the operator : represents the tensor inner product. The equations (1.70),(1.71) and (1.74) are the Braginskii equations for transport in a simple plasma [Braginskii, 1965], which further assume that the collisional mean free path is much smaller than the macroscopic length scale.

The problem of closure is still present in equation (1.74), since we do not have a fluid description of the quantity $\vec{h}_s$, only a kinetic one. Also, we do not have a description for the collisional terms W_s and F_s, or the components of the viscosity tensor $\boldsymbol{\pi}_s$; these forms are summarised in [Braginskii, 1965] for a strongly magnetised plasma where the collision rate is lower than the ion cyclotron frequency. The heat fluxes contain terms that redistribute the temperatures along their gradients and are proportional to $\nu\nabla T$ (ν is the collision rate), with a reduction dependent on $|B|$ perpendicular to $\vec{B}$, and the electron heat flux has an additional component dependent on $\nu\nabla(\vec{V}_i - \vec{V}_e)$ due to the thermal force felt by the relatively light electrons. The friction terms have a resistive part, which is due to the drag felt by the electrons in collisions with ions, and a thermal part due to an imbalance of thermal force felt in ion electron collisions when not in isothermal conditions. Resistivity of plasma is larger in the perpendicular direction, and the effect of the magnetic field on the thermal force is to generate a force perpendicular to both $\vec{B}$ and the temperature gradient due to the gyro motion of electrons. The frictional heating transfers heat from the hotter fluid to the colder one due to collisions, and the electron frictional heating term contains heating due to dissipation of currents, again in the limit of small electron mass. The viscosity tensor takes a specific form in strongly magnetised plasmas, with specific coefficients given in [Braginskii, 1965], and generally, acts to reduce gradients of velocity perpendicular to the direction of the velocity - the energy dissipated by this viscosity becomes thermal energy, and appears as the viscous heating term in the temperature equation (1.74).

We present a brief summary of the MHD equations, that will introduce the concept of magnetic confinement of plasma pressure in an equilibrium magnetic field. Multiplying (1.70) by the species mass and summing over species we find

$$\frac{\partial \rho}{\partial t} + \vec{\nabla} \cdot \rho \vec{u} = 0 \tag{1.75}$$

where $\rho = \sum_s m_s n_s$, and centre of mass velocity $\vec{u} = \sum_s n_s m_s V_s / \rho$. Summing the velocity equations, using neutrality to write $n_i \sim n_e \sim n$ and using the continuity equations to write the convective derivatives in their alternative form we find

$$\sum_s \left(\frac{\partial n_s m_s V_s}{\partial t} + \vec{\nabla} \cdot n_s m_s \vec{V}_s \otimes \vec{V}_s \right) + \vec{\nabla} n (T_i + T_e) + \vec{\nabla} \cdot (\boldsymbol{\pi}_i + \boldsymbol{\pi}_e) - en \left(\vec{V}_i - \vec{V}_e \right) \times \vec{B} = 0, \tag{1.76}$$

which is, under the MHD assumption $V_i \sim V_e$,

$$\left(\frac{\partial \rho \vec{u}}{\partial t} + \vec{\nabla} \cdot \rho \vec{u} \otimes \vec{u} \right) + \vec{\nabla} n (T_i + T_e) + \vec{\nabla} \cdot (\boldsymbol{\pi}_i + \boldsymbol{\pi}_e) - en \left(\vec{V}_i - \vec{V}_e \right) \times \vec{B} = 0, \tag{1.77}$$

and in addition, the plasma is assumed collisional enough to neglect the divergence of viscosity tensor. Total gas pressure $p = p_i + p_e$, and the flow of mass is given by the ion velocity, leaving

$$\rho \left(\frac{\partial}{\partial t} + \vec{u} \cdot \vec{\nabla} \right) \vec{u} = -\vec{\nabla} p + \vec{J} \times \vec{B}. \tag{1.78}$$

For completeness, the heat equations sum to

$$\left(\frac{\partial}{\partial t} + \vec{u} \cdot \vec{\nabla} \right) \frac{p}{\rho} = -\frac{2}{3} \frac{p}{\rho} \vec{\nabla} \cdot \vec{u}. \tag{1.79}$$

In the equilibrium limit, we assume that the convective derivative goes to zero, leaving the momentum equation as

$$\vec{\nabla} p = \vec{J} \times \vec{B}, \tag{1.80}$$

which is the equation defining magnetostatic configurations, which via the use of Ampere's law may be written as

$$\vec{\nabla} p = \frac{1}{\mu_0} \left(\vec{B} \cdot \vec{\nabla} \vec{B} - \frac{\vec{\nabla} B^2}{2} \right). \tag{1.81}$$

From these equations we can glean a few important points; first, for a plasma to be confined there must be current perpendicular to the magnetic field, and second, the equation is nonlinear in the components of the magnetic field B, so that solutions for a general plasma pressure may not exist and are unlikely to be unique. In the case of a tokamak, any current by the plasma alone will be insufficient for confinement, since this very current will tend to violate the force balance or another way, no solution for B can be found for a torus in (1.81) when the constant of integration is set to zero. A simplified tokamak configuration is shown in (1.1) that qualitatively describes the equilibrium magnetic field and general plasma quantities.

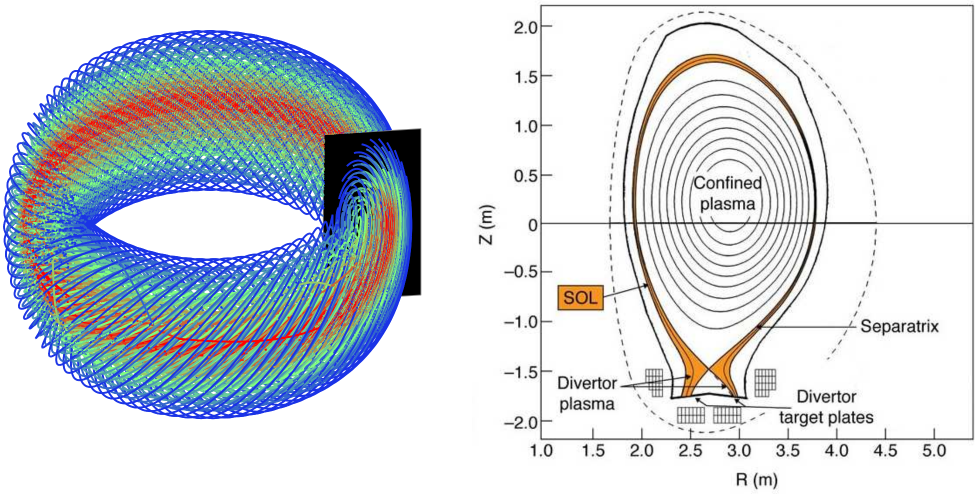

Figure 1.1: Schematic drawings of a tokamak, showing 3D equilibrium, closed and open flux surfaces, 2D cross section and region names. (left) Schematic equilibrium of closed field lines, in which to first approximation, plasma is only able to move along the field lines and, hence, is confined. (right) Collisional and anomalous transport violate this approximation, and plasma may move into the unconfined scrape off layer (SOL) where its journey along field lines terminates with the walls of the machine at the target plates.

1.3 Stability, Transport and Turbulence

Global stability of plasmas comes from MHD theory, and has progressed to the point that we are able to control the global equilibrium parameters very well. Ideal MHD equations are collisionless, so that there will be, in any real equilibrium, transport of heat and particles out of the equilibrium. Classical theory estimates the size of the transport coefficient using collisions as the sole reason for particle transport. A better estimate can be obtained by considering mirror effects, producing, so called banana orbits, and this approach is termed neoclassical. Neoclassical theory, and MHD, do not treat the effects of fluctuating plasma parameters caused by electron and ion motions that are inherently distinct (violating the MHD assumptions), and these fluctuations can correlate in velocity and pressure to cause so called "anomalous transport". Turbulence is observed as a chaotic behaviour in the fluid velocity, which retains a number of universal characteristics. These are, a cascade of energy from large scales to a small scale defined by Kolmogorov as the respective combination of viscosity and energy dissipation rate of $\left(\frac{\mu^3}{\epsilon}\right)^{\frac{1}{4}}$, with an energy spectrum proportional to $E(k) = C\epsilon^{\frac{2}{3}}k^{\frac{-5}{3}}$, and, the mixing and rotating properties. This leads to a wide range of scales resulting from deterministic yet chaotic equations of motion that can occur in any advective system. In particular, we might write a generalised equation of (fluid) motion

$$\left(\frac{\partial}{\partial t} + \vec{v} \cdot \vec{\nabla}\right) \vec{v} = \vec{F} + \mu \nabla^2 \vec{v}, \tag{1.82}$$

where particular forces characteristic of the system in question are absorbed into the term F, and we retain an explicit viscosity with coefficient μ. Ignoring the force term, we may write the equation as a toy model

$$\dot{v} = -v^2 + \frac{\mu}{l^2} v, \tag{1.83}$$

and employ a simple Euler forward model for $\dot{v}$

$$v_{n+1} = -\tau v_n^2 + \tau\mu\nabla^2 v_n + v_n \tag{1.84}$$

to study a single harmonic mode $v = ae^{-ikx}$ with wavenumber k of the system. In the spirit of the toy model, neglecting the fact that in reality modes cannot interact non-linearly with themselves, we obtain, denoting the single mode $v_k = x$,

$$x_{n+1} = -\tau x_n^2 - \tau\mu k^2 x_n + x_n \tag{1.85}$$

which may be written with $\tau = \left(1 - \mu\tau k^2\right)$ as

$$x_{n+1} = r x_n \left(1 - x_n\right). \tag{1.86}$$

This is a well studied logistic map [Frisch, 1995] (rescaled to $v \in [0, 1]$ and $\tau \in [0, 4]$) for turbulence; although it does not produce the specific features of turbulence,

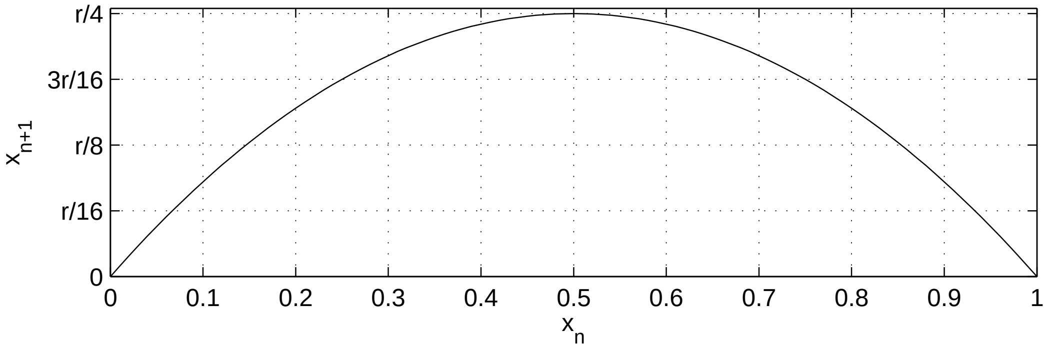

Figure 1.2: Logistic map of the system (1.86).

it demonstrates the onset of chaos from deterministic equations with a nonlinear term. The limit $\tau = 1$ (corresponding to $\tau = 4$ in the rescaled version) corresponds to zero viscosity, or alternatively, infinite Reynolds number. There are always two equilibrium values for the system at zero and $\frac{\tau-1}{\tau}$, and in figure 1.2 we can see that for $\tau < 2$ how the value might approach either equilibrium. When $\tau > 2$, it is clear that the value of x may begin to oscillate between disjoint high and low values of v and indeed there are purely orbital solutions to the system that never reach either equilibrium, but move through a repeated pattern of x values, evolution of x for the range of τ is shown in figure 1.3 for a chosen initial value. For sufficiently large τ, it becomes impossible to determine the orbit of x and the sequence of values followed becomes incredibly sensitive upon the initial value of x chosen - this is the essence of chaos. Of course, this is a nonphysical version of 1D incompressible flow with zero pressure variations, however turbulence onset occurs above a critical value of Reynolds number just as it does in real turbulence problems; there are no known solutions to determine the value of the critical Reynolds number for a particular system although rough estimates are known. The nature of the force term $\vec{F}$ has a distinct impact upon the type of turbulent path the velocity will take, and distinctions can be made between some of these different types of forces that result in turbulence with the same universal characteristics, but with different statistical scalings. Accurate estimates of "anomalous transport" require numerical modelling due to the nonlinear, turbulent nature of the fluctuations that drive it and a lack, in general, of analytical solutions to the nonlinear equations of motion. Indeed any purely analytical prediction of transport involving turbulent motions must be verified by either real data, or more commonly, numerical models; the impact of necessary analytical assumptions for nonlinear equations is often unclear.

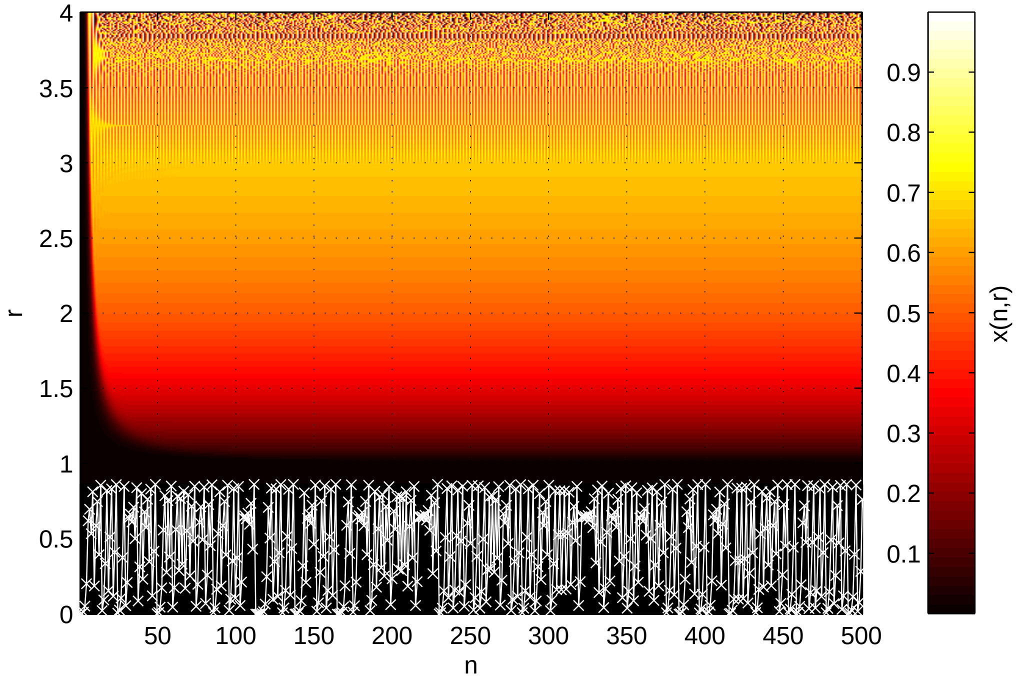

Figure 1.3: Series of initial values evolved with (1.86) mapped for a range of r showing the progress of the final state of x from equilibrium to orbital then bifurcating into turbulence. Time series for $r = 4$ shown at bottom.

The turbulent motion, laminar flows and collisional processes active in tokamak plasmas must all be taken into account if questions of stability and transport are to be addressed; in order for fusion machines to enter into the realms of practical energy sources, stability, keeping the global state of the plasma in equilibrium, must be maximised and transport, causing loss of heat and particles, minimised. The heat and particle loads experienced by the material surfaces of the device are of particular interest to engineers attempting to build the next generation of tokamaks [Loarte et al., 2007], and, the focus of this thesis is upon the transport of plasma through the SOL that will inevitably reach these surfaces. We will draw the introductory chapter to a close now by introducing two mechanisms that are responsible for such transport.

1.4 Drift Waves and Instability

Drift waves are a particular feature of electrostatic quasi-neutral plasmas, for which a short qualitative introduction is presented. The physics of drift waves can be found in many plasma theory books e.g. Miyamoto [2007]; Weiland [2000]. There are a very large number of assumptions made implicitly in this section in the interest of providing a brief and easy to understand picture of the basic physics. Fuller descriptions may be found in chapter 2 and in the referenced plasma physics books.

To begin, consider the situation of an unmagnetised, 1D hydrogen plasma with

$$n_i = n_0 + \tilde{n} \exp\left(\frac{\text{-}z^2}{2l_z^2}\right), \tag{1.87}$$

where $l_z \gg \lambda_d$: This plasma is also quasi-neutral, and therefore the electrostatic force will act upon the electrons (since the ions are far less mobile) to make $n_e = n_i$ very quickly. Assume there is no friction acting upon the electron motion, and that the electron temperature is a constant. Then, in a very short time (compared to the movement of ions) of $t = l_z/v_{th,e}$ where vth, e is the electron thermal speed, the equilibrium

$$T_e \partial_z n_e = e n_e \partial_z \phi, \tag{1.88}$$

will be reached. This means that we have

$$n_e = n_i \approx n_0 \exp\left(\frac{e\phi}{T_e}\right), \tag{1.89}$$

which is the source of the equilibrium used in the derivation of the Debye length in (1.5); this is the electric potential generated by the collective behaviour of the plasma that keeps the electrons in balance with the ions, and thus preserves quasi-neutrality. As a consequence, now consider that there is a constant magnetic field in the z direction, and that the ion density varies in the plane perpendicular to the magnetic field as

$$n_i = n_0 + \tilde{n} \exp\left(-\frac{z^2}{2l_z^2} - \frac{x^2+y^2}{2l_{xy}^2}\right), \tag{1.90}$$

where all the length scales are large compared to the Debye length. As a result of the perturbation with characteristic lengths in all three of these directions, the potential in the perpendicular plane will vary according to the variation in the density, i.e

$$\phi = \frac{T_e}{e}\left\{1 + \frac{\tilde{n}}{n_0} n \exp\left(-\frac{x^2+y^2}{2l_{xy}^2}\right)\right\}. \tag{1.91}$$

Since the plasma moves with the $\vec{E} \times \vec{B}$ drift, this constitutes a rotating vortex. Now consider that there is a gradient of the quantity n_0 in the x direction. The rotating vortex will cause a positive $\vec{v} \cdot \vec{\nabla} n_0$ flux on one side and a symmetric, negative flux on the other leading to the conservative propagation of the structure in the y direction, with leading edge on the side where the velocity is in the positive x direction. This is the drift wave. Of course, such a structure is likely to change shape due to dispersion. There are, however, many dispersionless density fluctuations: from the mundane harmonic oscillation to the more exotic soliton.

Now consider that there is some resistance to the electron parallel motion, so that the time taken to reach the equilibrium (1.89) becomes comparable, but still less than the timescale of the drift wave. In this case, the potential will tend to lag behind the density as the electrons struggle to maintain the equilibrium 1.89. This leads both to an increment of the fluctuation magnitude and a total flux in the x direction. This is most easily visualised by considering a fluctuation that only varies in the y and z directions and is singularly harmonic about n_0 in the y direction. In the zero resistivity or "adiabatic" case, v_x remains anti-symmetric about the density maxima leading to the dispersionless advection and conservation of fluctuation level. However, in the resistive case, v_x maxima moves closer to the density maxima and the amplitude of the fluctuation increases by drawing extra density to the fluctuation maxima from up the n_0 slope, and conversely to the density minima. This increases the magnitude of the potential gradients, and the process becomes self-sustaining. This is the drift wave instability. The instability will continue until the onset of turbulence, which can finally put a stop to the exponential growth of the fluctuation by destroying the regular structure.

Two things have been left out of the resistive discussion that must now be addressed: what form does turbulence resulting from $\vec{E} \times \vec{B}$ velocity take, and what happened to quasi-neutrality if the electrons mobility has been reduced by the resistivity? The answers to these questions are intimately linked. Consider that the initial values of n_e and n_i were equal, then we are forced by quasi-neutrality to state

$$\frac{\partial \rho}{\partial t} = 0 \tag{1.92}$$

where ρ is the charge density. If we then take the difference of the continuity equations and write in terms of charge density and volume currents $J = en\left(V_i - V_e\right)$ we find

$$\vec{\nabla} \cdot J = 0. \tag{1.93}$$

Therefore, any volume currents must satisfy this relation in order to conserve charge neutrality. This result may also be obtained from Maxwell's equations,

$$\vec{\nabla} \cdot \vec{D} = \rho, \tag{1.94}$$

$$\vec{\nabla} \times \vec{H} = \vec{J} + \frac{\partial \vec{D}}{\partial t}. \tag{1.95}$$

Taking the partial time derivative of 1.94 and the divergence of 1.95 allows the two equations to be combined as

$$0 = \vec{\nabla} \cdot \vec{J} + \frac{\partial \rho}{\partial t}, \tag{1.96}$$

which again, under the quasi-neutrality of 1.92 arrives at the conclusion of 1.4. In the case of the resistive drift wave, we have

$$T_e \partial_z n_e = e n_e \partial_z \phi - \eta e^2 n_e^2 \vec{V}_e \cdot \hat{z} \tag{1.97}$$

so that the divergence of the current,$J_z = -e n_e V_e$, in the z direction is

$$\frac{\partial J_z}{\partial z} = \frac{T_e}{\eta e} \partial_z^2 \left(\ln n_e - \frac{e\phi}{T_e} \right). \tag{1.98}$$

Parallel electron dynamics alone, therefore, cannot preserve quasi-neutrality in the resistive case, and so the plasma will resort to other collective effects to enforce the quasi-neutral state. This can be sketched with the particle drift picture: $\vec{E} \times \vec{B}$ drifts can carry no current, and the general force drift will only result in a divergence of J when the magnetic field is nonuniform, and in the electrostatic case, magnetic fields do not vary with time. This leaves the inertial drifts, the strongest of which tends to be the polarisation drift, leading to the current:

$$\vec{J_p} = \frac{n m_i}{e B^2} \left(\frac{\partial}{\partial t} + \frac{\vec{\nabla}\phi \times \hat{z}}{B} \cdot \vec{\nabla} \right) \vec{\nabla}\phi \tag{1.99}$$

where the electron contribution to the current is neglected, as their inertia is much smaller. This current acts in x, y plane, and must have a divergence that matches the one in the z direction to preserve the charge neutrality. We will make use of the relation

$$\vec{\nabla} \times \frac{\vec{\nabla}\phi \times \hat{z}}{B} = \frac{\partial_x^2 \phi + \partial_y^2 \phi}{B} \hat{z} = \frac{\nabla_\perp^2 \phi}{B} \hat{z} \tag{1.100}$$

to write the divergence of 1.99 in terms of the $\vec{E} \times \vec{B}$ velocity ($\vec{v}_E$) as much as possible and we assume $\vec{\nabla}_\perp \phi \cdot \vec{\nabla} n \ll \vec{\nabla}_\perp^2 \phi$,

$$n m_i \left(\frac{\partial}{\partial t} + \vec{v}_E \cdot \vec{\nabla} \right) \vec{\nabla} \times \vec{v}_E \cdot \hat{z} = \frac{B T_e}{\eta} \partial_z^2 \left(\frac{e\phi}{T_e} - \ln n \right). \tag{1.101}$$

We see that collective electric fields, giving rise to convective changes in the curl of the $\vec{E} \times \vec{B}$ drift (known as $\vec{E} \times \vec{B}$ vorticity) will act to balance the number densities of ions and electrons in the plasma - this is nothing more than the collective field in the $\hat{z}$ direction that arises to preserve quasi neutrality in equilibrium, only in this case the timescales of the parallel motion of electrons are small enough so that processes in the $\hat{x}, \hat{y}$ plane have time to to react and play a role in the preservation of quasi-neutrality. Indeed, this equation describes the lag experienced by the potential due to the resistivity; the LHS is an advection term for the vorticity, which can be slowed down by the resistive term on the RHS, leading to the unstable growth of the perturbation when there is a gradient of n_0 in the $\hat{x}$ direction as described. This is also a nonlinear advection equation, and as discussed will descend into a class of turbulent motion for $\vec{v}_E$ when the velocity grows large enough (note there is essentially zero viscosity in this equation). Thus the ion inertia is responsible for collective electric fields that maintain quasi-neutrality, which can, and usually does, result in turbulent motions for the velocity $\vec{v}_E$ - this type of turbulence is known as electrostatic plasma turbulence. Upon descent into turbulence, all fluctuating quantities are affected since they are advected by the turbulent velocity, and this leads to wild dispersion of the initial harmonic structure described; the characteristics of the non-turbulent phase (often called the linear phase) usually persist qualitatively in the turbulent (or nonlinear) phase but differ in an unpredictable manner quantitatively - this type of scenario is called drift wave turbulence [Weiland, 2000], which causes an amount of transport that can be difficult to predict.

1.5 Plasma Interchange and Instability

Plasma interchange is a particular feature of electrostatic quasi-neutral plasmas, for which a short qualitative introduction is presented. The physics of the plasma interchange can be found in many plasma theory books e.g. Miyamoto [2007]; Weiland [2000]. There are a very large number of assumptions made implicitly in this section in the interest of providing a brief and easy to understand picture of the basic physics. Fuller descriptions may be found in chapter 2 and in the referenced plasma physics books.

Consider a plasma that has no gradients in the $\hat{z}$ direction, but there is a constant gradient of the magnetic field in the $-\hat{x}$ direction. Similar to the preceding section, the assumption $\vec{\nabla}_\perp \phi \cdot \vec{\nabla} \frac{1}{B} \ll \vec{\nabla}_\perp^2 \phi$ will be used. Consider a plasma with a uniform gradient in magnetic field $\vec{\nabla} B = -g\hat{x}$, and with cold ions as a simplification, so that there is an addition to the divergence of volume current due to the electron drift in nonuniform magnetic field

$$\vec{\nabla} \cdot \vec{J}_{\nabla B} = \vec{\nabla} \cdot \left(n \frac{T_e}{B^2} g \hat{y} \right). \tag{1.102}$$

With the assumption of isothermal electrons and assuming that gradients in density are bigger than gradients in magnetic field 1.102 becomes

$$\vec{\nabla} \cdot \vec{J}_{\nabla B} = \frac{g T_e}{B^2} \frac{\partial n}{\partial y}. \tag{1.103}$$

Including the effects of curvature drifts, that are identical to the gradient drift to first approximation of a cylindrically symmetric magnetic field configuration, we may write

$$\vec{\nabla} \cdot \vec{J}_{\nabla B} = \frac{2 g T_e}{B^2} \frac{\partial n}{\partial y}. \tag{1.104}$$

In balance with the divergence of the ion polarisation current we find

$$n m_i \left(\frac{\partial}{\partial t} + \vec{v}_E \cdot \vec{\nabla} \right) \vec{\nabla} \times \vec{v}_E \cdot \hat{z} = -\frac{2 g T_e}{B^2} \frac{\partial n}{\partial y}, \tag{1.105}$$

which is the vorticity equation for the ideal electrostatic interchange, named for it's tendency to directly drive out positive density maxima while simultaneously driving in density minima, interchanging the low density plasma with the high density one [Weiland, 2000].

The ideal interchange flute mode ($\vec{k}_{\|} = 0$) is unstable for any density perturbation and is one of the most dangerous plasma instabilities which is capable of ejecting the entirety of the plasma from its confined state. This is still true when we include the parallel current 1.98 for a tokamak that has a purely torodial field, since the mode of disruption affecting the entire plasma due to interchange will not exhibit any potential variations or, of course, density variations along the field line, and quasi-neutrality will still be enforced by ion inertia alone. This is the reason that tokamak equilibrium configurations can not be made from purely torodial field, and instead, there must be a component of polodial field, connecting regions of opposing pressure gradients, and therefore of potentials with opposite sign. This allows the electrons to react to a flute mode interchange disruption and avert the collapse of the plasma. The polodial component of the parallel current in this case is called the Pfirsch-Schlter current, and stabilises the interchange instability for the low mode numbers of the order of the safety factor, but is less effective for the smaller size perturbations which will continue to cause transport on a less dramatic scale. The system of currents

$$nm_i\left(\frac{\partial}{\partial t}+\vec{v}_E\cdot\vec{\nabla}\right)\vec{\nabla}\times\vec{v}_E\cdot\hat{z}=-\frac{2gT_e}{B^2}\frac{\partial n}{\partial y}+\frac{BT_e}{\eta}\partial_z^2\left(\frac{e\phi}{T_e}-\ln n\right) \tag{1.106}$$

is known as the drift-interchange system, where the interchange component can have an enhancing effect on the drift wave turbulence.

In the tokamak edge region, following the field line the the z direction will, given an angle between z and the torodial direction, arrive back at the initial point, in one of two ways: After completing n laps of the torus when the polodial angle travelled in one lap is a rational fraction of 360°, or after an unspecified number n when this is not the case; the locations in the radial direction where such a rational fraction exists are called rational flux surfaces while the gaps in-between are known as ergodic layers and the distance travelled is known as the connection length. In either case, an estimate of the z gradients in potential and density may be made in terms of periodic harmonic perturbations with a fixed connection length. In the scrape off layer, such perturbations are not periodic and the plasma will be bounded in potential and density by the conditions of the surface the magnetic field intersects, although the connection length is more clearly defined in this case.

Chapter 2

Two Fluid Electrostatic Plasma Turbulence Theory

Some of the results of this section have been published at [Higgins et al., 2012]. The characteristic temporal and spatial scales of SOL and edge turbulence are $l > \rho_i$ and $\tau^{\text{-}1} > \omega_{c,i}$, the ion gyro-radius and gyro-frequency, respectively. This is referred to as the "low-frequency" part of the plasma turbulence, and in this context we use a technique known as drift ordering, which expands the fluid plasma equations in a power series of these scales so that we can choose to retain only the low order terms. This method is useful since it expresses the fluid equations in terms that may be considered more theoretically intuitive; a picture similar to the guiding centre drifts is obtained and the impact of each of these terms on the dynamics of the system can often be spotted from the structure of the equations alone.

2.1 Drift Ordering

The Braginskii equations introduced in section 1.2.2,

$$\partial_t n_s + \vec{\nabla} \cdot (n_s \vec{v}_s) = 0 \tag{2.1}$$

$$m_s n_s \frac{\mathrm{d}_s \vec{v}_s}{\mathrm{d}t} = -\vec{\nabla} p_s - \vec{\nabla} \cdot \pi_s + q_s n_s \left(\vec{E} + \vec{v}_s \times B \right) + \vec{R}_s \tag{2.2}$$

$$\frac{3}{2} n_s \frac{\mathrm{d}_s T_s}{\mathrm{d}t} + p_s \vec{\nabla} \cdot \vec{v}_s = -\vec{\nabla} \cdot \vec{h}_s - \pi_{s\alpha\beta} \frac{\partial v_{s\alpha}}{\partial x_\beta} + Q_s \tag{2.3}$$

are to be ordered with respect to the ion gyro-frequency, which gives a manageable analytic and numerical representation of the low-frequency drift-interchange turbulence. We begin with the simplest case where stress and collisionality are neglected, ion temperature is assumed to be zero and electron temperature to be isothermal.

The ordering is realised by first looking for an equilibrium solution to the momentum equation by setting the material derivative to zero. The momentum equation under the restrictions discussed becomes,

$$m_s n_s \left(\frac{\partial}{\partial t} + \vec{v}_s \cdot \nabla \right) \vec{v}_s = -\vec{\nabla} p_s + q_s n_s \left(\vec{E} + \vec{v}_s \times \vec{B} \right). \tag{2.4}$$

The ordering begins by finding the equilibrium velocity of the system. This is found by setting the rate of change of the velocity to zero, and rearranging for the velocity term that remains in the Lorentz force term,

$$T_s \vec{\nabla} n_s = q_s n_s \vec{E} + q_s n_s \vec{v}_s \times \vec{B}. \tag{2.5}$$

Then taking the cross product with $\vec{B}$ we find,

$$\frac{T_s}{q_s n_s} \left(\vec{\nabla} n_s \right) \times \vec{B} = \vec{E} \times \vec{B} + \left(\vec{v}_s \times \vec{B} \right) \times \vec{B}, \tag{2.6}$$

which by using the vector identity [Huba, 2006]

$$\vec{A} \times \left(\vec{B} \times \vec{C} \right) = \left(\vec{A} \cdot \vec{C} \right) \vec{B} - \left(\vec{A} \cdot \vec{B} \right) \vec{C}, \tag{2.7}$$

becomes, with $\hat{b}$ the unit vector in the direction of the magnetic field,

$$\begin{aligned} \left(\vec{v}_s \times \vec{B} \right) \times \vec{B} &= -\left(\vec{B} \cdot \vec{B} \right) v_s + \left(\vec{v}_s \cdot \vec{B} \right) \vec{B}, \\ &= -\left(B^2 \vec{v}_s - B^2 v_{s_{\parallel}} \hat{b} \right) = -B^2 \vec{v}_{s_{\perp}}. \end{aligned} \tag{2.8}$$

We are then left with equilibrium velocities perpendicular to the magnetic field,

$$\vec{v}_{\perp_1} = \frac{\vec{E} \times \vec{B}}{B^2} + \frac{T_s}{q_s B^2} \frac{\vec{B} \times \vec{\nabla} n_s}{n_s}. \tag{2.9}$$

Using the equilibrium velocities in the material derivative of the momentum equation allows us to find their inertial corrections, $v_{\perp_2}$,

$$m_s n_s \left(\frac{\partial}{\partial t} + \vec{v}_{\perp_1} \cdot \nabla \right) \vec{v}_{\perp_1} = -\vec{\nabla} p_s + q_s n_s \left(\vec{E} + \vec{v}_s \times \vec{B} \right), \tag{2.10}$$

defining $\frac{d}{dt} = \frac{\partial}{\partial t} + \vec{v}_{\perp_1} \cdot \vec{\nabla}$,

$$m_s n_s \frac{d}{dt}\left(\frac{\vec{E}\times\vec{B}}{B^2} + \frac{T_s}{q_s B^2}\frac{\vec{B}\times\vec{\nabla} n_s}{n_s}\right) = -\vec{\nabla} p_s + q_s n_s \left(\vec{E} + \vec{v}_s \times \vec{B}\right), \tag{2.11}$$

where we again take the cross product with $\vec{B}$ to arrive at

$$\vec{v}_{\perp_2} = \vec{v}_{\perp_1} - \frac{m_s}{q_s B^2}\left(\frac{d}{dt}\left[\frac{\vec{E}\times\vec{B}}{B^2} + \frac{T_s}{q_s B^2}\frac{\vec{B}\times\vec{\nabla} n_s}{n_s}\right]\right)\times\vec{B}. \tag{2.12}$$

It must be noted that drifts associated with the stress tensor π need to be included within the material derivative as they result in significant "diamagnetic cancellation" in combination with term 2 on the RHS of (2.9), discussed in e.g Chang and Callen [1992]; Weiland [2000]. Taking the $\times\vec{B}$ inside the time derivative results in

$$\begin{aligned}
\left(\vec{E}\times\vec{B}\right)\times\vec{B} &= -\left(\vec{B}\cdot\vec{B}\right)\vec{E} + \left(\vec{B}\cdot\vec{E}\right)\vec{B} \\
&= -B^2\left(\vec{E} - \vec{E}\cdot\hat{b}\right) = -B^2\vec{E}_\perp, \qquad (2.13) \\
\left(\vec{B}\times\vec{\nabla} n_s\right)\times\vec{B} &= -\left(\vec{B}\cdot\vec{\nabla} n_s\right)\vec{B} + \left(\vec{B}\cdot\vec{B}\right)\vec{\nabla} n_s \\
&= B^2\left(\vec{\nabla} n_s - \vec{\nabla}_{\parallel} n_s \hat{b}\right) = B^2\vec{\nabla}_\perp n_s, \qquad (2.14)
\end{aligned}$$

so that including inertial corrections the perpendicular velocity becomes

$$\vec{v}_\perp = \frac{\vec{E}\times\vec{B}}{B^2} - \frac{T_s}{q_s B^2}\frac{\vec{\nabla} n_s}{n_s}\times\vec{B} + \frac{m_s}{q_s B^2}\frac{dE_\perp}{dt} - \frac{m_s T_s}{q_s^2 B^2}\frac{d}{dt}\frac{\nabla_\perp n_s}{n_s}. \tag{2.15}$$

This treats the perpendicular direction only since $\hat{b}\times\hat{z} = 0$. Equation (2.15) can be viewed as an expansion in the gyro-frequency. Indeed writing (2.15) as

$$\vec{v}_\perp = \frac{\vec{E}\times\hat{b}}{|B|} - \frac{T_s}{q_s|B|}\frac{\vec{\nabla} n_s}{n_s}\times\hat{b} + \frac{1}{|B|}\omega_c^{-1}\frac{dE_\perp}{dt} - \frac{T_s}{q_s|B|}\omega_c^{-1}\frac{d}{dt}\frac{\nabla_\perp n_s}{n_s}, \tag{2.16}$$

we see that the rate of change of the density and electric field are being compared to the cyclotron frequency wherever they appear. In fact, if we had continued the series with further substitutions of this velocity into (2.4) we would obtain a series of the form

$$\vec{v}_\perp \approx \sum_{o=0}^{\infty}\left(\frac{1}{\omega_c}\right)^o \frac{d^o}{dt^o} f \approx \sum_{o=0}^{\infty}\left(\frac{\omega_f}{\omega_c}\right)^o \tag{2.17}$$

where f represents a general plasma quantity (in this case, density, density gradients and perpendicular electric fields), and ω some rate of change in these parameters.

From this it is clear that for $\omega_f > \omega_c$, the value of each term increases with the order o and hence the series is divergent. Thus we must have $\omega_f < \omega_c$ for the series to be a valid expansion at all. The limit of (2.15) where $o > 2$ are excluded becomes valid for ω_f orders of magnitude less than ω_c, so we say it is valid for $\omega_f \ll \omega_c$. This ordering is known as drift ordering, since it implies that the plasma is moving with velocities close to the familiar drift velocities. Typically the diamagnetic drift is assumed to be smaller than the $\vec{E} \times \vec{B}$ drift so that the perpendicular model is defined by,

$$\vec{v}_\perp = \frac{\vec{E} \times \vec{B}}{B^2} - \frac{T_s}{q_s B^2} \frac{\vec{\nabla} n_s}{n_s} \times \vec{B} + \frac{m_s}{q_s B^2} \frac{dE_\perp}{dt}. \tag{2.18}$$

The particle drifts resulting from gradients and curvature in the magnetic field (1.29) and (1.34) arise in the collective picture of (2.18) when considering the divergence of the term (second on the RHS) Garcia [2003]. Since the curvature and gradient drifts are approximately equal, and, curvature effects are not explicitly included in the simple geometries used in this thesis, we approximate any gradient in magnetic field with a factor 2 to include the curvature effects; often implicitly. The polarisation drift, term 3 on the RHS of (2.18), is often simplified using $m_e \ll m_i, T_i = 0$ and $\vec{v}_\| \cdot \vec{\nabla} \ll \vec{v}_\perp \cdot \vec{\nabla}$.

2.2 Parallel Current Boundary Conditions

The preceding section dealt with dynamics perpendicular to the magnetic field. Dynamics parallel to the magnetic field must be accounted for in the theory, since, the evolution equations for the plasma quantities look like

$$\partial_t n_s + \vec{\nabla} \cdot (n_s \vec{v}_{s\perp}) + \vec{\nabla} \cdot \left(n_s \vec{v}_{s\|}\right) = 0. \tag{2.19}$$

Clearly, an equation for $v_\|$, or as suggested in the title, $J_\| = env_\|$ is required in order to evaluate the evolution of the plasma quantities. In this thesis, the equations are made two dimensional by making particular assumptions about the third term of 2.19. In particular, edge plasmas are assumed to have periodic boundary conditions in $v_\|$, with a time constant harmonic representation of any gradients in the parallel direction. The SOL on the other hand is bounded by specific values for the parallel current where the magnetic field lines terminate with the walls of the device, these are specified by conducting surface sheath physics which will be discussed in this chapter, and any gradients are assumed to be linear with respect to these boundary conditions.

2.2.1 Edge Plasma

With a finite resistivity in the parallel direction, quasi-neutral electric fields will be generated in the presence of pressure gradients in the parallel direction. Assuming a simple collisional model for the resistivity, the parallel electron motion may be written, assuming ions do not carry significant parallel currents, as

$$0 = -T\vec{\nabla}_{\|}n + ne\vec{\nabla}_{\|}\phi - \eta e^2 n^2 v_{e_{\|}}, \tag{2.20}$$

given some resistivity η felt by the electrons during their parallel motion. The parallel electron current can then be written,

$$\vec{J}_{e_{\|}} = -env_{e_{\|}} = \frac{T}{\eta e}\left(\frac{\vec{\nabla}_{\|}n}{n} - \frac{e\vec{\nabla}_{\|}\phi}{T}\right). \tag{2.21}$$

The quantity of interest for equation 2.19 is the divergence of 2.21,

$$\vec{\nabla}\cdot\vec{J}_{e_{\|}} = \frac{T}{\eta e}\vec{\nabla}_{\|}\cdot\left(\frac{\vec{\nabla}_{\|}n}{n} - \frac{e\vec{\nabla}_{\|}\phi}{T}\right). \tag{2.22}$$

This can be made two dimensional by applying a local approximation, which in this case assumes the variance of the density due to gradients ($\tilde{n}$) is much smaller than it's value, and, there is a constant gradient, in the x-direction in the background quantity (n_0) which represents the equilibrium pressure gradient of the Tokamak,

$$n = n_0(x) + \tilde{n}(x, y, z); n_0(x) \gg \tilde{n}(x, y, z). \tag{2.23}$$

For the parallel current divergence 2.22, this simply gives

$$\vec{\nabla}\cdot\vec{J}_{e_{\|}} = \frac{T}{\eta e}\left(\frac{\vec{\nabla}_{\|}^2\tilde{n}}{n_0} - \frac{e\vec{\nabla}_{\|}^2\phi}{T}\right), \tag{2.24}$$

in which the dependence on the z coordinate is removed by assuming that density and potential are in phase in the z direction and obey a simple harmonic function $\propto \exp(ik_z z)$, giving

$$\vec{\nabla}\cdot\vec{J}_{e_{\|}} = -\frac{k_z^2 T}{\eta e}\left(\frac{\tilde{n}}{n_0} - \frac{e\phi}{T}\right). \tag{2.25}$$

This simple description of edge parallel dynamics produces good qualitative results of edge physics Horton [1999]; Dewhurst et al. [2009]. However, the assumption (2.23) is often questionable in the plasma edge and SOL, where fluctuations are often large. Also, the reduction of the parallel structure to a single mode is not compatible with $\vec{E} \times \vec{B}$ advection in the perpendicular plane since they may interact non-linearly.

2.2.2 Scrape Off Layer Plasma

In the scrape off layer, boundary conditions for the parallel currents are specified by consideration of the existence of a plasma sheath at two boundary points (conducting walls, often called divertors or limiters, or just target plates) in the parallel (z) direction and quasi-neutrality. The target plates are assumed to be negatively charged due the high mobility of electrons, and therefore a region of positive space charge exists in front of the wall. In order for quasi-neutrality to be enforced, this space charge must have an extent of the order of the Debye length, and, this condition places limits on some of the plasma quantities at the sheath edge.

Bohm's criterion gives the condition for a stationary plasma sheath at the conducting target plates, which may be derived using equations for ion continuity, energy conservation, electron density (Boltzmann) and Poisson's equation,

$$n_i y^{-\frac{1}{2}} = y_0^{-\frac{1}{2}} \tag{2.26}$$

$$y = y_0 + \xi \tag{2.27}$$

$$n_e = \exp\left(-\xi\right) \tag{2.28}$$

$$\frac{\partial^2 \xi}{\partial z^2} = n_i - n_e \tag{2.29}$$

i which are in normalised form of density normalised to a background n_0, kinetic energy y is normalised to the thermal energy $k_b T_e$, space to the Debye length and potential ξ normalised to the thermal potential $-e/k_b T_e$. We may evaluate the ion density from 2.26 and 2.27 as

$$n_i = \left(1 - \frac{\xi}{y_0}\right)^{-\frac{1}{2}}, \tag{2.30}$$

and then, multiplying 2.29 by $\frac{\partial z}{\partial \xi}$, we find

$$\left(\frac{\partial \xi}{\partial z}\right)^2 = 4y_0 \left[\left(1 - \frac{\xi}{y_0}\right)^{\frac{1}{2}} - 1\right] + 2\left[\exp\left(-\xi\right) - 1\right] \tag{2.31}$$

with the boundary condition $\xi = 0$ as $z \to -\infty$. Expanding about the point $\xi = 0$,

$$\left(\frac{\partial \xi}{\partial z}\right)^2 = \left(1 - \frac{1}{2y_0}\right)\xi^2 + O\left(\xi^3\right) \tag{2.32}$$

we see that unless $y_0 \geq 0.5$, the boundary condition specifying a decaying potential is violated, resulting in a contradiction. This condition can be written

$$v_0 \geq \sqrt{\frac{k_b T_e}{m_i}}, \tag{2.33}$$

specifying that ions must at least enter the sheath region with the sound speed in order to maintain a stationary sheath - this is Bohm's criterion [Bohm, 1949; Riemann, 1991]. In a situation where the ion velocity is sub-sonic, a potential known as the "pre-sheath" will develop in order to accelerate the ions to the sound speed when they reach the sheath entrance.

Considering the current flowing into the plasma sheath, taking 2.33 in the marginal form, we find

$$J_i = en\sqrt{\frac{T_e + T_i}{m_i}}. \tag{2.34}$$

The electron current to the material surface may be found by evaluating the average electron velocity through the potential difference of the sheath [Wesson, 1987]. Electrons that are too slow will simply be repelled, therefore the current is due to electrons with more kinetic energy than the potential energy of the sheath. We again assume that electrons are Boltzmann distributed

$$f(v_e) \propto \exp\left(\frac{-m_e v_e^2}{2T_e}\right), \tag{2.35}$$

and define a cut-off velocity for the electrons

$$v_{e0} = \sqrt{\frac{2e\Delta\phi}{m_e}} \tag{2.36}$$

from which we may define the average velocity of electrons that make it through the sheath

$$\langle v_e \rangle = \frac{\int_{v_{e0}}^{\infty} v_e f(v_e)}{\int_{-\infty}^{\infty} f(v_e)}. \tag{2.37}$$

Using the Gaussian integrals

$$\int x e^{-cx^2}\,\mathrm{d}x = -\frac{1}{2c}\,e^{-cx^2}, \tag{2.38}$$

$$\int_{-\infty}^{\infty} e^{-ax^2}\,\mathrm{d}x = \sqrt{\frac{\pi}{a}} \quad (a > 0), \tag{2.39}$$

the integral 2.37 may be evaluated,

$$\langle v_e \rangle = \sqrt{\frac{T_e}{2\pi m_e}} \exp\left(\frac{-e\Delta\phi}{T_e}\right), \tag{2.40}$$

which therefore gives the electron current through the sheath,

$$J_e = -en\sqrt{\frac{T_e}{2\pi m_e}} \exp\left(\frac{-e\Delta\phi}{T_e}\right). \tag{2.41}$$

From 2.41 and 2.34, assuming quasi-neutrality, we can find the difference in potential between the sheath entrance and target plate,

$$\frac{e\Delta\phi}{T_e} = 0.5\ln\left(\frac{m_i/m_e}{2\pi\left(1.0 + T_i/T_e\right)}\right), \tag{2.42}$$

which for normal plasma values reduces to the approximate form,

$$\Lambda = \Delta\phi \approx 3.0\frac{T_e}{e}. \tag{2.43}$$

This is commonly known as the sheath potential drop Λ, giving the potential drop from the sheath to the wall. The quasi-neutral assumption is altered when there are perpendicular currents involved. Here we will assume that the electrons react adiabatically in the plasma to communicate any potential down to the plasma sheath, and, that the conducting target plate sits at a constant potential in the perpendicular direction. Then, when the plasma potential varies in the perpendicular direction, electrons will be conducted in order to restore the sheath potential drop Λ. In this two-dimensional approach, we define the averaging operator

$$\langle f(z) \rangle_{\parallel} = \frac{1}{2l_{\parallel}} \int_{-l_{\parallel}}^{l_{\parallel}} f(z)dz, \tag{2.44}$$

so that equation (2.19) can be written as

$$\partial_t n_s + \vec{\nabla} \cdot (n_s \vec{v}_{s\perp}) + \frac{1}{q_s}\partial_z J_{s_{\parallel}} = 0, \tag{2.45}$$

which is operated on by the averaging operator (2.44) to give

$$\langle \partial_t n_s \rangle_{\parallel} = -\left\langle \vec{\nabla} \cdot n_s \vec{v}_{s\perp} \right\rangle_{\parallel} - \frac{1}{q_s}\left\langle \partial_z J_{s_{\parallel}} \right\rangle_{\parallel}. \tag{2.46}$$

The parallel current is then assumed to vary linearly between the two target plates at $\pm l_{\parallel}$, so that only the boundary conditions $J_{\pm l_{\parallel}}$ are needed to specify the parallel dynamics of 2.46. Taking again the equations 2.34 and 2.41 we find

$$J_{\pm l_{\parallel}} = \pm en\sqrt{\frac{T_e + \gamma T_i}{m_i}}\left(1 - \sqrt{\frac{T_e m_i}{2\pi\left(T_e + \gamma T_i\right) m_e}}\exp\left(-\frac{e\phi}{T_e}\right)\right), \tag{2.47}$$

in which, potential difference across the sheath has been written in terms of the plasma potential, assuming a reference potential of zero at the surface. Finally, the factor in front of the exponential can be recognised as the equilibrium sheath potential drop, and the averaged divergence can be then written as

$$\left\langle \partial_z J_{\parallel} \right\rangle_{\parallel} = \frac{en\sqrt{\frac{T_e+\gamma T_i}{m_i}}}{l_{\parallel}}\left\{1 - \exp\left(\frac{e\left(\Lambda - \phi\right)}{T}\right)\right\}. \tag{2.48}$$

In the isothermal regime, this term damps any potential disturbance in the bulk plasma, caused by any
$\left\langle \vec{\nabla} \cdot J_{\perp} \right\rangle_{\parallel}$ toward the equilibrium Λ. The values of the divertor quantities may be allowed to vary in a simple way so that they take time-constant values, n_t, T_t. In doing so, we may retain the simplicity of our models if the perpendicular averages are written

$$\left\langle \vec{\nabla}_{\perp} \cdot \vec{f} \right\rangle_{\parallel} = \vec{\nabla}_{\perp} \cdot \vec{f_b}, \tag{2.49}$$

so that a model with a constant-value target density (and spatio-constant temperature) could be

$$\left\langle \partial_z J_{\parallel} \right\rangle_{\parallel} = \frac{en_t\sqrt{\frac{T_e+\gamma T_i}{m_i}}}{l_{\parallel}}\left\{1 - \exp\left(\frac{e\left(\Lambda - \phi\right)}{T}\right)\right\}. \tag{2.50}$$

If electron temperature is allowed to vary transverse to the magnetic field, the sheath potential drop has another effect on the perpendicular turbulence, as reported by [Myra et al., 2004], since the parallel currents can now drive the potential toward the equilibrium

$$\phi = \frac{T}{e}\left(3.0 - \ln(1)\right) \tag{2.51}$$

The electric fields created by this mechanism produce a torque on blob-like structures that spins them up, and mixes the electric field generated by the ideal interchange mechanism, which reduces this ideal radial transport.

Considering this boundary condition in more detail, we will allow both density (as in (2.73)) and temperature to take unique values at the sheath boundary. In particular we split ion and electron temperatures up into perpendicular and parallel values. Assuming $T_{e\|} = T_{i\|} = T_{e\perp}$ at the mid-plane, $T_{e\|} = T_{e\perp} \neq T_{i\|}$ at the sheath and $T_{i\perp} = 0$ everywhere. We will call $T_{i\|}$ at the sheath T_t, and all the other temperatures T (they are all equal). The ion temperature must become one dimensionally adiabatic at the sheath edge ($\gamma = 3$) if a fluid approach is consistent [Riemann, 1991], which leads to a modification of (2.48) to

$$\left\langle \partial_z J_\| \right\rangle_\| = \sqrt{\frac{T + 3T_t}{m_i}} \frac{en_t}{l_\|} \left\{ 1.0 - \exp\left(3.0 - \frac{e\phi}{T} \right) \right\}. \qquad (2.52)$$

The boundary condition in (2.52) will alter the torque applied by the mechanism that causes the filaments to spin compared to (2.48). In particular, the rotation generated in (2.48) stabilises the shear flow instabilities associated with the filament advection in the radial direction via mixing, but, introduces a new rotational instability [Myra et al., 2004]. The rotation generation and damping with respect to the sheath potential in (2.52) is increased toward the edges of the filament, and reduced in the centre which may alter the rotational stability properties and the magnitude of the mixing of interchange associated vorticity.

2.2.3 Limitations due to parallel averaging

There are 2 very notable limitations of the model 2.50. Firstly,for convenience we imply that $< v_\| >< n >=< nv_\| >$, since the gradient $< \partial_\|(nv_\|) >$ is taken as the difference between the mid-plane $nv_\|$ (=0) and the $nv_\|$ at the target. Secondly, the model implies density gradient in the parallel direction. This means that there may be an additional potential gradient in the parallel direction to support quasi-neutrality under such disparate pressure forces for electrons and ions, and would bear similarities to the treatment of drift waves thus far, resembling some $k_{0\|}$ of (1.89). These are neglected in this thesis, which limits itself to the study to the simplest effects of the boundary conditions on the mid-plane plasma. This simplicity leads to the necessity to make ad-hoc assumptions about temperatures, e.g, that electron and ion temperature may be different at the sheath boundary yet ions have no thermal perpendicular motions. Linearising the parallel direction to $\pm\vec{J}_{s\|}$ also neglects nonlinear motions in the parallel flows and consequently nonlinear interactions of nonlinear parallel flows and nonlinear perpendicular advection.

2.3 Theoretical Modelling of Plasma Filaments

Due to the vortical nature of the plasma velocity during drift wave and interchange motions, and, the tendency of the drift wave and interchange instabilities to strongly enhance the magnitude of these rotating density inhomogeneities, in edge and SOL plasma, coherent structures commonly form in the plane perpendicular to the magnetic field, known as blobs. These structures typically have an elongated character along the magnetic field line, due to the faster motions in this direction. This three-dimensional structure is known as a filament. Models of fast convective transport by plasma filaments have been developed [Krasheninnikov, 2001; Garcia et al., 2005] and some of their predictions have been supported by observations [Ayed et al., 2009; Rozhansky and Kirk, 2008]. A simple particle guiding centre picture of these qualitative models arises from the polarisation of a region of enhanced SOL density due to an inhomogeneous magnetic field. This produces an electric field which is in phase with the blob density, and causes an advection opposite to $\vec{\nabla} B$ as shown in figure 2.1. In the mid-plane of a tokamak, this is perpendicular to and directed at the first wall. This is the basic principle behind the electrostatic interchange. The current produced by particle gyrations in an inhomogeneous magnetic field are identically represented by the diamagnetic current in a velocity-averaged fluid description [Garcia, 2003], and indeed the diamagnetic term in equation (2.18) will be where the electrostatic interchange arises from. The qualitative models are derived using drift-ordering in the plane perpendicular to the confining magnetic field and

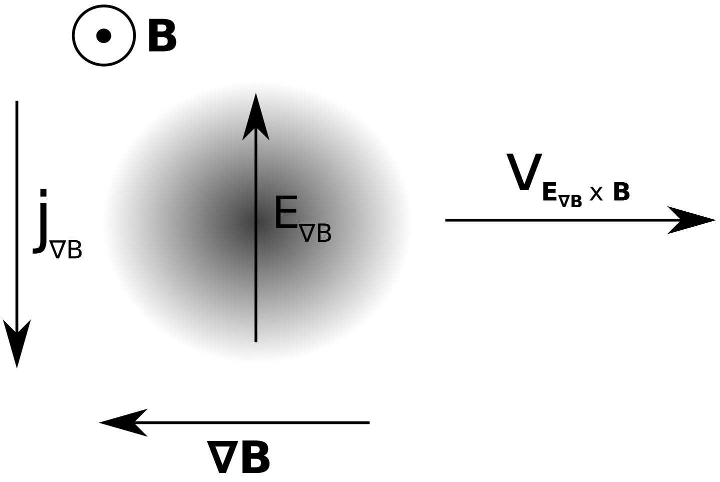

Figure 2.1: Schematic model of filament $E \times B$ advection, from a guiding centre drift perspective.

a closure for the parallel transport, which may be specific to a region of interest. Firstly, the polarisation term for the perpendicular electron motion is removed due to the small electron mass, the diamagnetic term for ions is removed within the cold ion approximation and the electric field is assumed to be electrostatic so that $\vec{E} = -\vec{\nabla}\phi$. This leads to continuity equations for ions and electrons,

$$\partial_t n_e + \nabla \cdot \left(n_e \frac{\vec{B} \times \vec{\nabla}\phi}{B^2} + \frac{T_e}{eB^2} \vec{\nabla} n_s \times \vec{B} \right) + \nabla_{\|} n_e \vec{v}_{e_{\|}} = 0, \tag{2.53}$$

$$\partial_t n_i + \nabla \cdot \left(n_i \frac{\vec{B} \times \vec{\nabla}\phi}{B^2} - \frac{m_i n_i}{eB^2} \frac{d\vec{\nabla}_{\perp}\phi}{dt} \right) + \nabla_{\|} n_i \vec{v}_{i_{\|}} = 0. \tag{2.54}$$

Three further assumptions are made: magnetic field is assumed as $\vec{B} = B(x)\hat{z}$ so that curvature is neglected, it is assumed that $\nabla n \gg \frac{\nabla B}{B}$ and finally the so called Boisonique approximation is used so that $\vec{\nabla} \cdot \frac{n}{B^2} \frac{d\vec{\nabla}_{\perp}\phi}{dt} \approx \frac{n}{B^2} \frac{d\vec{\nabla}_{\perp}^2 \phi}{dt}$. The equations then become,

$$\left(\partial_t + \vec{v}_E \cdot \nabla\right) n_e = \frac{1}{e} \vec{\nabla}_{\|} J_{e_{\|}} + \frac{T_e}{e} \frac{\partial B^{-1}}{\partial x} \frac{\partial n_e}{\partial y}, \tag{2.55}$$

$$\left(\partial_t + \vec{v}_E \cdot \nabla\right) n_i = -\frac{1}{e} \vec{\nabla}_{\|} J_{i_{\|}} + \frac{n_i m_i}{e} \left(\partial_t + \vec{v}_E \cdot \nabla\right) \frac{\vec{\nabla}_{\perp}^2 \phi}{B^2}, \tag{2.56}$$

where $\hat{y}$ represents the polodial direction and $\hat{x}$ represents the radial direction, and the parallel velocities have be written in terms of the volume currents. The quasi neutrality condition ($n_e = n_i = n$) then leads to an equation for plasma density n and vorticity $\Omega = \vec{\nabla}_{\perp}^2 \phi / B^2 \approx \vec{\nabla} \times \vec{v}_E$ [Krasheninnikov, 2001],

$$\left(\partial_t + \vec{v}_E \cdot \nabla\right) n = 0, \tag{2.57}$$

$$\left(\partial_t + \vec{v}_E \cdot \nabla\right) \Omega = \frac{1}{n m_i} \vec{\nabla}_{\|} \left(J_{e_{\|}} + J_{i_{\|}} \right) + \frac{T_e}{n m_i} \frac{\partial B^{-1}}{\partial x} \frac{\partial n}{\partial y}. \tag{2.58}$$

The diamagnetic drift and the polarisation drift are dropped in equation (2.57) due to the ordering in ω_c. Parallel currents are also dropped in equation (2.57) since the instantaneous response of a plasma density blob to the potential perturbation is of interest. At this point we discuss two limiting cases of equation (2.58), dominant and negligible parallel currents.

2.3.1 Dominant Parallel Currents

Parallel currents in the mid-plane may be governed by the Bohm criterion at the sheath boundary near the divertor plates [Riemann, 1991; Bohm, 1949]. The averaged parallel current can therefore be described, starting from equation (2.48), as

$$\langle \nabla_{\|} J_{\|} \rangle_{\|} = \frac{e n_t C_s}{l_{\|}} \left(1 - \exp \frac{\text{-}e\phi}{T} \right) \approx \frac{e n_t C_s}{l_{\|}} \left(\frac{e\phi}{T} \right), \tag{2.59}$$

with $e\phi < T$, where $n_t, l_{\|}, C_s$ are the target density, parallel length and sound speed respectively. By averaging equations (2.56),(2.58) in the parallel direction the sheath currents (2.59) can be included in the model,

$$\left(\partial_t + \vec{v}_E \cdot \nabla \right) n_b = 0, \tag{2.60}$$

$$\left(\partial_t + \vec{v}_E \cdot \nabla \right) \Omega_b = \frac{1}{n_b m_i} \frac{e n_t C_s}{l_{\|}} \left(\frac{e\phi_b}{T_e} \right) + \frac{T_e}{n_b m_i} \frac{\partial B^{-1}}{\partial x} \frac{\partial n_b}{\partial y}, \tag{2.61}$$

with n_b, ϕ_b, Ω_b representing the average blob density, potential and vorticity in the parallel direction. Since the scale of the divertor sheath is of the order of the Debye length, most of the average in the quantities n_b, ϕ_b, Ω_b comes from the presheath variation; this will be very close to the mid-plane values. We assume that perpendicular gradients do not vary in the parallel direction. Note that the $\vec{E} \times \vec{B}$ drift becomes $v_E = (b \times \nabla_{\perp} \phi_b)/B$. Terms unaffected by the averaging are the magnetic field B and electron temperature T_e. In this work the assumption $\partial_x \ln(B) = R_0^{-1}$ is used, where R_0 is the tokamak major radius.

Assuming constant vorticity in the filament (due to dominating parallel currents, and the lack of time variation in the parallel currents), (2.61) can be rearranged to find the electrostatic potential ϕ which can then be substituted into (2.57) to give

$$\partial_t n_b + \frac{T l_{\|} \rho_i}{e B R_0} \left\{ \left[\partial_x \left(\frac{1}{n_t} \partial_y n_b \right) \right] (\partial_y n_b) - \left[\partial_y \left(\frac{1}{n_t} \partial_y n_b \right) \right] (\partial_x n_b) \right\} = 0. \tag{2.62}$$

In [Krasheninnikov, 2001], a separable solution $n_b(x, y, t) = n_b(x, t) n_b(y)$ has been found assuming $n_b/n_t = \xi = const$ and $n_b(y) = \exp(-y^2/2l_{\perp}^2)$. The continuity equations then becomes

$$\partial_t n_b + \frac{T l_{\|} \rho_i}{e B R_0 l_{\perp}^2 \xi} \partial_x n_b = \partial_t n_b + 2 C_s \frac{\rho_i^2}{l_{\perp}^2} \frac{l_{\|}}{R_0} \frac{1}{\xi} \partial_x n_b = 0. \tag{2.63}$$

Equation (2.63) represents a radial advection of blob density n_b with velocity

$$\frac{\vec{v}_E}{C_s} = \frac{\rho_i^2}{l_{\perp}^2} \frac{l_{\|}}{R_0} \frac{1}{\xi} \hat{x}, \tag{2.64}$$

as given in [Krasheninnikov, 2001], where C_s is the sound speed. Note that in (2.65) and (2.64), δ is the plasma magnetisation which must be $\ll 1$ for this fluid model to be valid.

$$\rho_i/l_\perp \approx \delta \tag{2.65}$$

2.3.2 Negligible Parallel Currents

With $J_\| \approx 0$, the diamagnetic currents are closed by plasma vorticity (in the $\perp$ plane) from ion polarisation currents. In this case the scaling of filament radial velocity can be found by dimensional analysis of (2.58) under the flute approximation (since parallel transport is negligible) and a vorticity which is only constant in time,

$$\vec{v}_E \cdot \nabla\Omega = -\frac{T_e}{nm_i}\frac{1}{BR_0}\frac{\partial n}{\partial y}. \tag{2.66}$$

The approximation

$$\vec{\nabla} \times \vec{v}_E = \partial_x \left(\frac{\partial_x \phi \hat{z}}{B}\right) + \partial_y \left(\frac{\partial_y \phi \hat{z}}{B}\right) \approx \frac{\nabla_\perp^2 \phi}{B}\hat{z} = \Omega\hat{z} \tag{2.67}$$

is used to write (2.66) as

$$\vec{v}_E \cdot \vec{\nabla}\left|\vec{\nabla} \times \vec{v}_E\right| = -\frac{C_s^2}{n}\frac{1}{R_0}\frac{\partial n}{\partial y}. \tag{2.68}$$

Finally, the local non-linearity approximation

$$n = n_0 + \tilde{n}, \quad |n_0| \gg |\tilde{n}|, \quad n_0 = f(x) \tag{2.69}$$

with $n_0, \tilde{n}$ the background and fluctuating density respectively, is used to write (2.68) as

$$\vec{v}_E \cdot \vec{\nabla}\left|\vec{\nabla} \times \vec{v}_E\right| = -\frac{C_s^2}{n_0}\frac{1}{R_0}\frac{\partial \tilde{n}}{\partial y}, \tag{2.70}$$

which has the dimensional scaling (found by replacing all perpendicular derivatives with $1/l_\perp$) in v_E/C_s of

$$\frac{v_E}{C_s} \sim \left(\frac{l_\perp}{R_0}\frac{\tilde{n}}{n_0}\right)^{\frac{1}{2}}, \tag{2.71}$$

as given in [Garcia et al., 2005], valid only in the case of small density fluctuations.

When the local approximation (2.69) is not valid, the scaling (2.71) is incorrect and the dimensional analysis of the fully nonlinear equation (2.68) is

$$\frac{v_E}{C_s} \sim \left(\frac{l_\perp}{R_0}\right)^{\frac{1}{2}}. \tag{2.72}$$

2.3.3 Dominant Parallel Currents with Constant Target Density

Here, we would like to relax the assumption $n_b/n_t = \xi = const$ that leads to (2.64). This would allow the target density n_t to be independent from that of a filament and we will consider n_t to be constant. Physically, such a condition could be approximately realised if the target density was an average over some number of filaments that crossed a given radial location in some window of time. This assumption leads to a modified continuity equation,

$$\frac{\partial n_b}{\partial t} + \frac{Tl_{\|}\rho_i}{eBR_0 n_t}\left\{\left[\frac{\partial}{\partial x}\left(\frac{\partial}{\partial y}n_b\right)\right]\frac{\partial n_b}{\partial y} - \left[\frac{\partial}{\partial y}\left(\frac{\partial}{\partial y}n_b\right)\right]\frac{\partial n_b}{\partial x}\right\} = 0. \qquad (2.73)$$

This will advect regions of negative curvature, like the peaks associated with filaments. For a function of $n_b = \frac{-y^2}{2l_\perp}$ we find the solution.

$$\frac{\vec{v}_E}{C_s} = \frac{\rho_i^2}{l_\perp^2}\frac{l_{\|}}{R_0}\frac{n_b}{n_t}\hat{x}. \qquad (2.74)$$

The equation (2.73) describes the *radial ($\hat{x}$)* advection of structures with a density that has negative curvature in the *polodial ($\hat{y}$)* direction; the scaling (2.74) describes the advection of a region of such negative curvature. A density that has a variation of polodial curvature will have variations in the resulting radial velocity. Regions with negative polodial curvature (e.g. peaks) in density will move radially *outward*, and regions with positive polodial curvature (e.g. troughs) will move radially *inward.*

2.4 Numerical Modelling of SOL and edge turbulence

In this section we derive and discuss systems of equations that form the basis for numerical models employed in this thesis. They all take advantage of the drift ordering framework, which significantly reduces the computational effort with respect to the Braginskii equations (even before you take into account the loss of the stress, collision and conduction terms). Three models have been developed that use varying levels of assumptions about the perpendicular and parallel dynamics.

2.5 HW Model

Perhaps the simplest of these, is the Hasegawa Wakatani model [Hasegawa and Wakatani, 1983] which differs from the present discussion since it is usually applicable to the edge plasma. SOL models usually do not include resistivity in the parallel current term that gives rise to the drift instability that characterises the model, although this has been identified as a significant dissipation mechanism for SOL filaments [Angus et al., 2012]. The model is build upon (2.55) and (2.56),

$$\left(\partial_t + \vec{v}_E \cdot \nabla\right) n_e = \frac{1}{e}\vec{\nabla}_{\|} J_{e_{\|}} + \frac{T_e}{e}\frac{\partial B^{-1}}{\partial x}\frac{\partial n_e}{\partial y}, \tag{2.75}$$

$$\left(\partial_t + \vec{v}_E \cdot \nabla\right) n_i = -\frac{1}{e}\vec{\nabla}_{\|} J_{i_{\|}} + \frac{n_i m_i}{e}\left(\partial_t + \vec{v}_E \cdot \nabla\right)\frac{\vec{\nabla}_{\perp}^2 \phi}{B^2}, \tag{2.76}$$

In this case the electron equation is chosen for the continuity equation,

$$\left(\partial_t + \vec{v}_E \cdot \nabla\right) n = \frac{1}{e}\vec{\nabla}_{\|} J_{e_{\|}} + \frac{T}{e}\frac{\partial B^{-1}}{\partial x}\frac{\partial n}{\partial y}, \tag{2.77}$$

and quasi-neutrality requires that

$$\left(\partial_t + \vec{v}_E \cdot \nabla\right)\frac{\vec{\nabla}_{\perp}^2 \phi}{B^2} = \frac{1}{n m_i}\vec{\nabla}_{\|} J_{e_{\|}} + \frac{T}{n m_i}\frac{\partial B^{-1}}{\partial x}\frac{\partial n}{\partial y}. \tag{2.78}$$

Substituting in the parallel current divergence result 2.25, for which we must apply the local model

$$n = n_0 + \tilde{n}, \quad |n_0| \gg |\tilde{n}|, \quad n_0 = f(x), \tag{2.79}$$

the equations become,

$$\left(\partial_t + \vec{v}_E \cdot \nabla\right)\tilde{n} - \frac{1}{B}\frac{\partial \phi}{\partial y}\frac{\partial n_0}{\partial x} = -\frac{k^2 T}{\eta e^2}\left(\frac{\tilde{n}}{n_0} - \frac{e\phi}{T}\right) - \frac{T}{eB^2}\frac{\partial B}{\partial x}\frac{\partial \tilde{n}}{\partial y}, \tag{2.80}$$

$$\left(\partial_t + \vec{v}_E \cdot \nabla\right)\vec{\nabla}_{\perp}^2 \phi = -\frac{k^2 B^2 T}{\eta e n_0 m_i}\left(\frac{\tilde{n}}{n_0} - \frac{e\phi}{T}\right) - \frac{T}{n_0 m_i}\frac{\partial B}{\partial x}\frac{\partial \tilde{n}}{\partial y}. \tag{2.81}$$

Normalising $t \to t\omega_c$ for time, $x \to \frac{x}{\rho_i}$ for space, $\phi \to \frac{e\phi}{T}$ for potential and $n \to \frac{n}{n_0}$ for density we obtain dimensionless versions of (2.80) and (2.81) that read:

$$\left(\partial_t + \hat{z} \times \nabla\phi \cdot \nabla\right)\tilde{n} - \frac{1}{n_0}\frac{\partial \phi}{\partial y}\frac{\partial n_0}{\partial x} = -\frac{k^2 T}{\eta e^2 n_0 \omega_c}\left(\tilde{n} - \phi\right) - \frac{1}{B}\frac{\partial B}{\partial x}\frac{\partial \tilde{n}}{\partial y}, \tag{2.82}$$

$$\left(\partial_t + \hat{z} \times \nabla\phi \cdot \nabla\right)\vec{\nabla}_{\perp}^2 \phi = -\frac{T k^2}{e^2 \eta \omega_c n_0}\left(\tilde{n} - \phi\right) - \frac{1}{B}\frac{\partial B}{\partial x}\frac{\partial \tilde{n}}{\partial y}. \tag{2.83}$$

We define the constants $\kappa = -\frac{\partial \ln n_0}{\partial x}$, $C = -\frac{\partial \ln B}{\partial x}$ and $\alpha = \frac{k^2 T}{n_0 e^2 \eta \omega_c}$, rename $n = \tilde{n}$ and write the advective terms as $\hat{z} \times \nabla\phi \cdot \nabla f = [\phi, f]$,

$$\frac{\partial n}{\partial t} = [n, \phi] - \kappa \frac{\partial \phi}{\partial y} - \alpha (n - \phi) + C \frac{\partial n}{\partial y}, \tag{2.84}$$

$$\frac{\partial \vec{\nabla}_{\perp}^2 \phi}{\partial t} = \left[\vec{\nabla}_{\perp}^2 \phi, \phi\right] - \alpha (n - \phi) + C \frac{\partial n}{\partial y}. \tag{2.85}$$

these are the normalised model equations. $\vec{E} \times \vec{B}$ compression has been neglected. Attention should be drawn to the assumption of a single harmonic mode in the z direction via $\partial_z n = i k_z n$.

2.6 TOKER Model

We have created a numerical model based on the TOKAM 2D [Sarazin and Ghendrih, 1998] simulation to assess the accuracy of our data analysis methods and also to study the role of parallel currents, which we will call TOKER. The parallel boundary conditions are changed so that they can either take the usual flute model assumptions $\vec{\nabla}_{\|}(T, n) = 0$, or one where density is set to an independent value at the parallel target boundary. The model is built on the perpendicular drift ordered velocities,

$$\vec{v}_{\perp s} = \frac{\vec{E} \times \vec{B}}{B^2} - \frac{T_s}{q_s B^2} \frac{\vec{\nabla} n_s}{n_s} \times \vec{B} + \frac{m_s}{q_s B^2} \frac{d}{dt} \vec{E}_{\perp}, \tag{2.86}$$

and the continuity equation for particle density,

$$\frac{\partial n_s}{\partial t} + \vec{\nabla} \cdot (n_s \vec{v}_{s_\perp}) + \vec{\nabla} \cdot \left(n_s \vec{v}_{s_\|}\right) = 0 \tag{2.87}$$

Now we will determine the quantity $\nabla \cdot (v_s n_s)$. We assume the electric field is described by the potential ϕ such that $E = -\nabla \phi$, and that the magnetic field B is constant and in the $\hat{z}$ direction. Poisson brackets are used for convenience and these are defined as:

$$[A, B] = \partial_x A \partial_y B - \partial_y A \partial_x B, \tag{2.88}$$

$$[A, \cdot] = \partial_x A \partial_y - \partial_y A \partial_x, \tag{2.89}$$

$$\left[\vec{A}, \vec{B}\right] = \partial_x \vec{A} \cdot \partial_y \vec{B} - \partial_y \vec{A} \cdot \partial_x \vec{B}. \tag{2.90}$$

We will commonly make use of the following relations, often implicitly,

$$\hat{z} \times \vec{\nabla} f \cdot \vec{\nabla} g = [f, g], \tag{2.91}$$

$$\vec{\nabla} \cdot \hat{z} \times \vec{\nabla} f = 0. \tag{2.92}$$

The perpendicular velocities 2.86 can therefore be written as

$$\vec{v}_\perp = \frac{\hat{z}\times\vec{\nabla}_\perp\phi}{B} + \frac{T_s\hat{z}\times\vec{\nabla}_\perp n_s}{q_s n_s B} - \frac{m_s n}{q_s B^2}\left(\partial_t + \frac{1}{B}\left[\phi,\cdot\right] + \frac{T_s}{q_s n_s B}\left[n_s,\cdot\right]\right)\vec{\nabla}_\perp\phi, \quad (2.93)$$

from which a calculation of $\vec{\nabla}\cdot(\vec{v}_s n_s)$ yields

$$\begin{aligned}\nabla\cdot(v_s n_s) = \left[\phi,\tfrac{n}{B}\right] + \tfrac{T_s}{q_s}\left[n_s,\tfrac{1}{B}\right] - \tfrac{m_s n_s}{q_s B^2}\left(\partial_t\vec{\nabla}^2_\perp\phi + \tfrac{1}{B}\left[\phi,\vec{\nabla}^2_\perp\phi\right]\right)\\ -\tfrac{m_s T_s}{q_s^2 B^3}\left(\left[\vec{\nabla}_\perp n_s,\vec{\nabla}_\perp\phi\right] + \left[n_s,\vec{\nabla}^2_\perp\phi\right]\right)\\ -\tfrac{m_s}{q_s}\left(\partial_t\vec{\nabla}_\perp\phi\cdot\vec{\nabla}_\perp\tfrac{n}{B^2} + \left[\phi,\vec{\nabla}_\perp\phi\right]\cdot\vec{\nabla}_\perp\tfrac{n}{B^3} + \tfrac{T_s}{q_s}\left[n_s,\vec{\nabla}_\perp\phi\right]\cdot\vec{\nabla}_\perp\tfrac{1}{B^3}\right). \quad (2.94)\end{aligned}$$

We have neglected drifts due to the stress tensor π, which contains the gyro-viscous stress that must be included in a model with $T_i \neq 0$ since it results in significant "diamagnetic cancellation" Chang and Callen [1992]. We consider a simplified form by reducing (2.94) to

$$\begin{aligned}\nabla\cdot(v_s n_s) = \tfrac{1}{B}\left[\phi,n_s\right] + \tfrac{T_s}{q_s}\left[n_s,\tfrac{1}{B}\right]\\ -\tfrac{n_s m_s}{q_s B^2}\left(\partial_t\vec{\nabla}^2_\perp\phi + \tfrac{1}{B}\left[\phi,\vec{\nabla}^2_\perp\phi\right] + \tfrac{T_s}{q_s}\left(\left[\vec{\nabla}_\perp n_s,\vec{\nabla}_\perp\phi\right] + \left[n_s,\vec{\nabla}^2_\perp\phi\right]\right)\right). \quad (2.95)\end{aligned}$$

The terms

$$n_s\left[\phi,B^{-1}\right] + \frac{n_s m_s}{q_s}\left(\frac{3\partial_t\vec{\nabla}_\perp\phi}{B^3} + \frac{4\left[\phi,\vec{\nabla}_\perp\phi\right]}{B^4} + \frac{4T_s\left[n_s,\vec{\nabla}_\perp\phi\right]}{n_s q_s B^4}\right)\cdot\vec{\nabla}_\perp B \quad (2.96)$$

were neglected since they are curvature terms expected to be small compared to term 2 on the RHS of (2.95) within the constant temperature hypothesis. However, in a model with non-constant temperature, these terms are expected to be significant. The terms

$$-\frac{m_s}{q_s}\left(\frac{1}{B^2}\partial_t\vec{\nabla}_\perp\phi\cdot\vec{\nabla}_\perp n_s + \frac{1}{B^3}\left[\phi,\vec{\nabla}_\perp\phi\right]\cdot\vec{\nabla}_\perp n_s\right) \quad (2.97)$$

are neglected since they are of comparable nonlinear structure to terms kept in (2.95) and not expected to add much depth to the model, while increasing the complexity of a numerical investigation; these are the same assumptions as those used in [Sarazin and Ghendrih, 1998]. Assuming cold ions, isothermal electrons and inertia-less electrons the continuity equations are

$$\partial_t n_e = \frac{1}{B}\left[n_e,\phi\right] + \frac{1}{e}\vec{\nabla}_\parallel J_{e\parallel} - \frac{T_e}{e}\left[B^{-1},n_e\right], \quad (2.98)$$

$$\partial_t n_i = \frac{1}{B}\left[n_i,\phi\right] - \frac{1}{e}\vec{\nabla}_{\|} J_{i_{\|}} - \frac{m_i n_i}{eB^2}\partial_t \nabla_\perp^2\phi + \frac{m_i n_i}{eB^3}\left[\vec{\nabla}_\perp^2\phi,\phi\right]. \tag{2.99}$$

In order to find the vorticity equation we subtract equations (2.98),(2.99) and invoke quasi-neutrality by setting $n_e = n_i$,

$$\frac{m_i n}{eB^2}\partial_t \nabla_\perp^2\phi = \frac{1}{e}\vec{\nabla}_{\|}\left(J_{e_{\|}} + J_{i_{\|}}\right) + \frac{m_i n}{eB^3}\left[\vec{\nabla}_\perp^2\phi,\phi\right] - \frac{T_e}{e}\left[B^{-1},n\right]. \tag{2.100}$$

We choose to follow the ion continuity equation;

$$\partial_t n = \frac{1}{B}\left[n,\phi\right] + \frac{1}{e}\vec{\nabla}_{\|} J_{i_{\|}}, \tag{2.101}$$

The averaged divergence of the parallel current is given by (2.50), so that

$$\partial_t n = \frac{1}{B}\left[n,\phi\right] + \frac{n_t C_s}{l_{\|}}, \tag{2.102}$$

$$\frac{m_i n}{eB^2}\partial_t \nabla_\perp^2\phi = \frac{n_t C_s}{l_{\|}}\left(e^{-\frac{e\phi}{T}} - 1\right) + \frac{m_i n}{eB^3}\left[\vec{\nabla}_\perp^2\phi,\phi\right] - \frac{T_e}{e}\left[B^{-1},n\right], \tag{2.103}$$

with $e\phi \ll T$. Normalisations are $\omega_c = eB/m_i$ for time, $\rho_i = \sqrt{Tm_i}/eB$ for space, T/e for potential and n_t for density. Including ad-hoc diffusion (for numerical stability, and the validity of the strongly collisional Braginskii model), viscosity and density source terms, the normalised model equations are

$$\begin{aligned} \left(\frac{\partial}{\partial t} - D\nabla_\perp^2\right) n &= \left[n,\phi\right] - \sigma e^{-\phi} + S && (2.104)\\ \left(\frac{\partial}{\partial t} - \nu\nabla_\perp^2\right)\nabla_\perp^2\phi &= \left[\nabla_\perp^2\phi,\phi\right] + \frac{\sigma}{n}\left(1 - e^{-\phi}\right) - \frac{g}{n}\frac{\partial n}{\partial y}. && (2.105) \end{aligned}$$

with $g = \frac{\rho_i}{R_c}$, R_c the radius of curvature of the tokamak and $\sigma = \frac{\rho_i}{l_{\|}}$.

2.7 hTOKER Model

We have developed an electrostatic interchange model incorporating the effects of the parallel current density (2.52) and (2.48), based on the TOKER model. We begin again from equation (2.87),

$$\frac{\partial n_s}{\partial t} + \vec{\nabla}\cdot\left(n_s \vec{v}_{s_\perp}\right) + \vec{\nabla}\cdot\left(n_s \vec{v}_{s_{\|}}\right) = 0 \tag{2.106}$$

and the perpendicular velocity model (2.86), where temperature remains inside the derivative for the diamagnetic term,

$$v_\perp = \frac{E\times B}{B^2} - \frac{\nabla p_s \times B}{q_s n_s B^2} + \frac{m_s}{q_s B^2}\left(\partial_t + \frac{E\times B}{B^2}\cdot\nabla - \frac{\nabla p_s\times B}{q_s n_s B^2}\cdot\nabla\right)E_\perp . \qquad (2.107)$$

Again, it is assumed that $E = -\nabla\phi$, and that the magnetic field B is constant and in the $\hat{z}$ direction. The quantities $\nabla\cdot n_s v_{s\perp}$ and $\nabla\cdot v_{s\perp}$ must be known. We have,

$$\vec{v}_\perp = \frac{\hat{z}\times\vec{\nabla}_\perp\phi}{B} + \frac{\hat{z}\times\vec{\nabla}_\perp p_s}{q_s n_s B} - \frac{m_s}{q_s B^2}\left(\partial_t + \frac{1}{B}\left[\phi,\cdot\right] + \frac{1}{q_s n_s B}\left[p_s,\cdot\right]\right)\vec{\nabla}_\perp\phi \qquad (2.108)$$

which yields

$$\begin{aligned}\nabla\cdot(v_s n_s) = \left[\phi,\tfrac{n}{B}\right] + \tfrac{1}{q_s}\left[p_s,\tfrac{1}{B}\right] - \tfrac{m_s n_s}{q_s B^2}\left(\partial_t\vec{\nabla}_\perp^2\phi + \tfrac{1}{B}\left[\phi,\vec{\nabla}_\perp^2\phi\right]\right)\\ -\tfrac{m_s}{q_s^2 B^3}\left(\left[\vec{\nabla}_\perp p_s,\vec{\nabla}_\perp\phi\right] + \left[p_s,\vec{\nabla}_\perp^2\phi\right]\right)\\ -\tfrac{m_s}{q_s}\left(\partial_t\vec{\nabla}_\perp\phi\cdot\vec{\nabla}_\perp\tfrac{n}{B^2} + \left[\phi,\vec{\nabla}_\perp\phi\right]\cdot\vec{\nabla}_\perp\tfrac{n}{B^3} + \tfrac{1}{q_s}\left[p_s,\vec{\nabla}_\perp\phi\right]\cdot\vec{\nabla}_\perp\tfrac{1}{B^3}\right), \qquad (2.109)\end{aligned}$$

and similarly,

$$\begin{aligned}\nabla\cdot(v_s) = \left[\phi,\tfrac{1}{B}\right] + \tfrac{1}{q_s}\left[p_s,\tfrac{1}{n_s B}\right] - \tfrac{m_s}{q_s B^2}\left(\partial_t\vec{\nabla}_\perp^2\phi + \tfrac{1}{B}\left[\phi,\vec{\nabla}_\perp^2\phi\right]\right) \qquad (2.110)\\ -\tfrac{m_s}{n_s q_s^2 B^3}\left(\left[\vec{\nabla}_\perp p_s,\vec{\nabla}_\perp\phi\right] + \left[p_s,\vec{\nabla}_\perp^2\phi\right]\right)\\ -\tfrac{m_s}{q_s}\left(\partial_t\vec{\nabla}_\perp\phi\cdot\vec{\nabla}_\perp\tfrac{1}{B^2} + \left[\phi,\vec{\nabla}_\perp\phi\right]\cdot\vec{\nabla}_\perp\tfrac{1}{B^3} + \tfrac{1}{q_s}\left[p_s,\vec{\nabla}_\perp\phi\right]\cdot\vec{\nabla}_\perp\tfrac{1}{n_s B^3}\right). \qquad (2.111)\end{aligned}$$

We have neglected drifts due to the stress tensor π, which contains the gyro-viscous stress that must be included in a model with $T_i \neq 0$ since it results in significant "diamagnetic cancellation" Chang and Callen [1992].

The final three terms of equations (2.109) and (2.111) are neglected for the same reasons given in the previous section for the TOKER model. Although these terms become more important for the ballooning structure of interchange turbulence in the non-isothermal limit [Sarazin and Ghendrih, 1998], we neglect them to reduce the numerical effort. Terms 5 and 6 are neglected within the cold ion limit. Parallel currents of the form 2.52 are used. We follow the ion continuity equation,

$$\partial_t n = \left[\frac{n}{B},\phi\right] - \frac{n_t}{l_\|}\sqrt{\frac{T+3T_t}{m_i}} \qquad (2.112)$$

neglecting terms of order ω_c^p for $p > 0$. Using $C_t = \sqrt{\frac{T+3T_t}{m_i}}$, the continuity equations for each species are

$$\partial_t n_i = \left[\frac{n_i}{B}, \phi\right] + \frac{m_i n_i}{eB^2}\left(\partial_t \vec{\nabla}_\perp^2 \phi + \frac{1}{B}\left[\phi, \vec{\nabla}_\perp^2 \phi\right]\right) - \frac{n_t C_t}{l_\|} \tag{2.113}$$

and

$$\partial_t n_e = \left[\frac{n_e}{B}, \phi\right] - \frac{1}{B^2 e}\left[B, p_e\right] - \frac{n_t C_t}{l_\|}\exp\left(3.0 - \frac{e\phi}{T}\right). \tag{2.114}$$

Subtracting and invoking quasi-neutrality we find

$$\begin{aligned} 0 = \tfrac{m_i n_i}{eB^2}\left(\partial_t \vec{\nabla}_\perp^2 \phi + \tfrac{1}{B}\left[\phi, \vec{\nabla}_\perp^2 \phi\right]\right) \\ -\tfrac{n_t C_t}{l_\|} + \tfrac{1}{B^2 e}\left[B, p_e\right] + \tfrac{n_t C_t}{l_\|}\exp\left(3.0 - \tfrac{e\phi}{T}\right) \end{aligned} \tag{2.115}$$

which, rearranged in terms of vorticity gives

$$\partial_t \nabla_\perp^2 \phi = \frac{1}{n_i m_i}\left[p_e, B\right] + \frac{1}{B}\left[\nabla_\perp^2 \phi, \phi\right] + \frac{eB^2}{n_i m_i}\frac{n_t C_t}{l_\|}\left(1 - \exp\left(3.0 - \frac{e\phi}{T_e}\right)\right) \tag{2.116}$$

The heat equation is

$$\frac{3}{2} n_s \left(\partial_t + \frac{z \times \nabla \phi}{B} \cdot \nabla + \frac{z \times \nabla p_s}{q_s n_s B} \cdot \nabla\right) T_s = -p_s \nabla \cdot v_s. \tag{2.117}$$

Ion perpendicular temperature is zero. The electron heat equation is

$$\partial_t T = \frac{1}{B}\left[T, \phi\right] + \frac{2T}{3B^2}\left[\phi, B\right] - \frac{2T}{3l_\|}\sqrt{\frac{T + 3T_t}{m_i}}, \tag{2.118}$$

neglecting terms of order ω_c^{-1} or greater. Collisional transport needs to be represented, the pertinent collision times as given by [Braginskii, 1965; Helander and Sigmar, 2002] are

$$\tau_{ei} = \frac{12\pi^{\frac{3}{2}}}{\sqrt{2}} \frac{\sqrt{m_e} T_e^{\frac{3}{2}} \varepsilon_0^2}{ne^4 \ln(\Lambda)} \tag{2.119}$$

$$\tau_{ii} = \frac{12\pi^{\frac{3}{2}}}{\sqrt{2}} \frac{\sqrt{m_i} T_i^{\frac{3}{2}} \varepsilon_0^2}{ne^4 \ln(\Lambda)}. \tag{2.120}$$

The classical perpendicular diffusivities are

$$\begin{aligned} D_n &= (1+T_i/T_e)\,\rho_e^2\nu_{ei} && (2.121)\\ D_T &= 2\rho_i^2\nu_{ii} && (2.122)\\ D_\Omega &\approx \frac{3}{8}D_{T_i} = \frac{6}{8}\rho_i^2\nu_{ii} && (2.123) \end{aligned}$$

Neoclassical Pfirsch Schulter fluxes in the radial direction are approximated by the diffusivities

$$\begin{aligned} D_n^{PS} &= 1.3q_{95}^2 D_n && (2.124)\\ D_T^{PS} &= 1.6q_{95}^2 D_T && (2.125)\\ D_\Omega^{PS} &= 1.6q_{95}^2 D_\Omega && (2.126) \end{aligned}$$

from [Fundamenski et al., 2007]. For normalisation B_0, T_0 and n_0 are chosen as reference values, followed by the definitions

$$C_0 = \sqrt{\frac{T_0}{m_i}},\ \omega_0 = \frac{eB_0}{m_i},\ \rho_0 = \frac{C_0}{w_0}. \qquad (2.127)$$

Time is normalised to $1/\omega_0$, potential to T_0/e, space to ρ_0 and velocity to C_0. Vorticity is defined as $\Omega = \nabla_\perp^2\phi$. We write the normalised collision related terms as

$$D_n = C_n\varepsilon_e\frac{\rho_e^2 n}{T^{\frac{3}{2}}},\ D_T = C_T\varepsilon_i\frac{\rho_i^2 n}{T^{\frac{3}{2}}},\ D_\Omega = C_\Omega\varepsilon_i\frac{\rho_i^2 n}{T^{\frac{3}{2}}}, \qquad (2.128)$$

where we have defined the constants

$$C_n = 0.212,\ C_T = 0.699,\ C_\Omega = 0.159, \qquad (2.129)$$

$$\varepsilon_e = \frac{n_0 e^4}{\sqrt{m_e}T_0^{\frac{3}{2}}\omega_0\varepsilon_0^2},\ \varepsilon_i = \frac{n_0 e^4}{\sqrt{m_i}T_0^{\frac{3}{2}}\omega_0\varepsilon_0^2}. \qquad (2.130)$$

The diffusive terms are written

$$\begin{aligned} R_n &= \nabla_\perp\cdot\left(D_n\nabla_\perp + D_n^{ps}\partial_r\hat{r}\right)n && (2.131)\\ R_\Omega &= \nabla_\perp\cdot\left(D_\Omega\nabla_\perp + D_\Omega^{ps}\partial_r\hat{r}\right)\Omega && (2.132)\\ R_T &= \nabla_\perp\cdot\left(D_T\nabla_\perp + D_T^{ps}\partial_r\hat{r}\right)T && (2.133) \end{aligned}$$

Normalised model equations are

$$
\begin{aligned}
\partial_t n &= \frac{1}{B}\left[n,\phi\right] - \frac{n}{B^2}\left[B,\phi\right] - \frac{n_t}{l_{\|}}\sqrt{T+3T_t} + R_n + S_n, && (2.134)\\
\partial_t \nabla_\perp^2 \phi &= \frac{1}{n}\left[p,B\right] + \frac{1}{B}\left[\nabla_\perp^2\phi,\phi\right] + \frac{B^2}{n}\frac{n_t}{l_{\|}}\sqrt{T+3T_t}\left(1.0 - \exp\left(3.0 - \frac{e\phi}{T}\right)\right)\\
&+ R_\Omega + S_\Omega, && (2.135)\\
\partial_t T &= \frac{1}{B}\left[T,\phi\right] + \frac{2T}{3B^2}\left[\phi,B\right] - \frac{2T}{3l_{\|}}\sqrt{T+3T_t} + R_T + S_T. && (2.136)
\end{aligned}
$$

2.7.1 Warm Ions

The effects of warm ions may be rudimentarily included in the model. Returning to equation (2.109),

$$
\begin{aligned}
\nabla\cdot\left(v_s n_s\right) = \left[\phi,\tfrac{n}{B}\right] + \tfrac{1}{q_s}\left[p_s,\tfrac{1}{B}\right] - \tfrac{m_s n_s}{q_s B^2}\left(\partial_t\vec{\nabla}_\perp^2\phi + \tfrac{1}{B}\left[\phi,\vec{\nabla}_\perp^2\phi\right]\right)\\
-\tfrac{m_s}{q_s^2 B^3}\left(\left[\vec{\nabla}_\perp p_s,\vec{\nabla}_\perp\phi\right] + \left[p_s,\vec{\nabla}_\perp^2\phi\right]\right)\\
-\tfrac{m_s}{q_s}\left(\partial_t\vec{\nabla}_\perp\phi\cdot\vec{\nabla}_\perp\tfrac{n}{B^2} + \left[\phi,\vec{\nabla}_\perp\phi\right]\cdot\vec{\nabla}_\perp\tfrac{n}{B^3} + \tfrac{1}{q_s}\left[p_s,\vec{\nabla}_\perp\phi\right]\cdot\vec{\nabla}_\perp\tfrac{1}{B^3}\right), \quad (2.137)
\end{aligned}
$$

we may retain the term $-\tfrac{m_s}{q_s^2 B^3}\left(\left[\vec{\nabla}_\perp p_s,\vec{\nabla}_\perp\phi\right] + \left[p_s,\vec{\nabla}_\perp^2\phi\right]\right)$ relatively simply, under the assumption that ion and electron temperatures are equal, giving a change in the normalised vorticity equation that reads

$$
\begin{aligned}
\partial_t \nabla_\perp^2 \phi &= \frac{2}{n}\left[p,B\right] + \frac{1}{B}\left[\nabla_\perp^2\phi,\phi\right] + \frac{B^2}{n}\frac{n_t}{l_{\|}}\sqrt{T+3T_t}\left(1.0 - \exp\left(3.0 - \frac{e\phi}{T}\right)\right)\\
&+ \frac{1}{nB}\left(\left[\nabla_\perp^2\phi, nT\right] + \left[\vec{\nabla}_\perp\phi,\vec{\nabla}_\perp(nT)\right]\right) + R_\Omega + S_\Omega. && (2.138)
\end{aligned}
$$

Of course, these equations are only a valid combination where the scale of interest is larger than the ion Larmor radius, which, in the warm ion case is of course nonzero. When this scale assumption is violated, the electric fields associated with ϕ and the densities associated with n become defined differently for ions, and the entire fluid approach must be altered, for example [Madsen et al., 2011].

2.7.2 Inconsistencies in the hTOKER model

There are a number of inconsistencies in the model.

The parallel model is extremely simplified, neglecting many of the effects that removing the flute mode assumption ($\partial_z n, \partial_z T = 0$) would imply as discussed at 2.2.3.

We have also neglected the gyro-viscous stresses by not including the stress tensor in the drift model 2.1. This is of particular importance in the warm ion model, because it will lead to so called "gyro-viscous cancellation". The classic form of this cancellation is to completely cancel the total time derivative of the diamagnetic part of the plasma polarisation, however, other models restate the effect such that the advection of plasma vorticity with the diamagnetic velocity is cancelled Chang and Callen [1992]. Therefore the warm ion effects added in (2.138) are not consistent without the addition of the drifts due to the gyro-viscous forces. For example, the divergence of the (ion) gyro-viscous part of the Braginskii stress tensor,

$$\nabla \cdot \Pi = \left(\partial_x \Pi_{xx} + \partial_y \Pi_{xy}\right)\hat{x} + \left(\partial_x \Pi_{yx} + \partial_y \Pi_{yy}\right)\hat{y}, \tag{2.139}$$

with $\eta = \frac{p_i}{\omega_i}$,

$$\begin{aligned} &\left(-\partial_x \eta \left(\partial_x v_y + \partial_y v_x\right) + \partial_y \eta \left(\partial_x v_x - \partial_y v_y\right)\right)\hat{x} \\ &\left(\partial_x \eta \left(\partial_x v_x - \partial_y v_y\right) + \partial_y \eta \left(\partial_x v_y + \partial_y v_x\right)\right)\hat{y}, \end{aligned} \tag{2.140}$$

which may be written

$$\begin{aligned} \nabla \cdot \Pi &= \eta \left(\partial_x^2 + \partial_y^2\right)\left(v_x \hat{y} - v_y \hat{x}\right) \qquad (2.141) \\ &+ \left(\partial_x v_y \hat{x} + \partial_y v_x \hat{x} + \partial_x v_x \hat{y} - \partial_y v_y \hat{y}\right)\partial_x \eta \\ &+ \left(\partial_x v_y \hat{y} + \partial_y v_x \hat{y} + \partial_x v_x \hat{x} - \partial_y v_y \hat{x}\right)\partial_y \eta, \end{aligned}$$

which can be identified as the compact form

$$\nabla \cdot \Pi = \eta \left(\hat{z} \times \vec{\nabla}^2 \vec{v}\right) + \left(\hat{z} \times \vec{\nabla} v_x - \vec{\nabla} v_y\right)\partial_x \eta + \left(\hat{z} \times \vec{\nabla} v_y + \vec{\nabla} v_x\right)\partial_y \eta. \tag{2.142}$$

A drift velocity $\vec{v}_\Pi = \frac{1}{enB}\nabla \cdot \Pi$ may be identified from the gyro-viscous stress, which gives

$$\vec{v}_\Pi = \frac{1}{2}\rho \left\{ \left(\vec{\nabla} v_x + \hat{z} \times \vec{\nabla} v_y\right)\partial_x \Xi + \left(\vec{\nabla} v_y - \hat{z} \times \vec{\nabla} v_x\right)\partial_y \Xi - \vec{\nabla}_\perp^2 \vec{v} \right\} \tag{2.143}$$

with

$$\Xi = \ln B + \ln \rho^2 - \ln n, \tag{2.144}$$

and ρ the ion gyro-radius. The cancellation will occur in the quasi-neutrality condition $\vec{\nabla} \cdot \vec{J}$ for the currents caused by v_Π and the advection of the plasma vorticity with diamagnetic velocity,

$$\vec{\nabla} \cdot n \left(\vec{v}_{\Pi} + \vec{v}_{pd} \right), \tag{2.145}$$

where

$$\vec{v}_{pd} = \frac{m}{eB^2} \vec{v}_d \cdot \nabla \left(\hat{z} \times \vec{v} \right) = \rho^2 \left(\hat{z} \times \vec{\nabla} \ln(nT) \right) \cdot \vec{\nabla} \left(\hat{z} \times \vec{v} \right). \tag{2.146}$$

Such a calculation is very long indeed, however, the general result is that as with plasma density, vorticity may not be advected with the diamagnetic velocity in a plasma with uniform magnetic field. Corrections due to curvature are second order, yet hTOKER keeps some first order terms from $\vec{v}_{pd}$ which should be cancelled with terms originating from $\vec{v}_{\Pi}$. In addition, the neglection of the stress tensor means that there is no viscous heating present in the heat equation. The warm ion effects are therefore not presented in the correct form in the hTOKER model.

Also, the dissipation term for temperature is not realistic. Firstly, parallel electron thermal conduction may be large, yet has been neglected. Secondly, average electron velocity through the sheath should be modified by the Boltzmann factor, so that electron temperature would be more strongly dissipated in regions with lower potential (due to higher electron loss through the now lowered, non-equilibrium sheath potential drop). In the interest of including finite ion temperature effects in a simplistic way, these terms have been neglected so that the assumption $T_i = T_e$ may be made. The spirit of the model is therefore to test the effects of the constant divertor density/temperature model on the plasma vorticity equation. Note, however, that in most cases the spatial average of the plasma potential will be quite close to the equilibrium sheath potential drop, and therefore the dissipation model for temperature may be considered approximately correct over a large enough spatio-temporal scale.

As such, the model should not be considered exact or even accurate, but rather a qualitative tool in the study of SOL plasma turbulence.

2.8 Summary

In this chapter we have discussed the contemporary advective theory of blobs using drift ordering, and, demonstrated its application to the advective theory of plasma blobs. Present sheath limited and polarisation limited results for blob advective velocity are shown, and the sheath limited case is extended to include the case of independent plasma density and temperature at the sheath boundary (located at the wall-plasma intersection along the magnetic field line). This model predicts a blob velocity that is proportional to the blob density. The theoretical basis of the numerical models TOKER and hTOKER is presented, and a particular configuration of parallel and perpendicular temperatures is employed that simplifies the models in both the cold and warm ion cases. The warm ion model is very approximate, and should only be considered for qualitative studies in the best case.

Chapter 3

Scaling of filament velocity with density

Some of the results of this section have been published in [Higgins et al., 2012]. In chapter 2, we have reviewed solutions and scaling of radial velocity for interchange motions. These scalings can predict order of magnitude velocities that agree with experimental values of velocity, however for different values of the parameters. The model scalings are, with explicit factor of 2 to account for curvature effects,

$$\frac{\vec{v}_E}{C_s} = 2\frac{\rho_i^2}{l_\perp^2}\frac{l_\parallel}{R_0}\frac{1}{\xi}\hat{x}, \tag{3.1}$$

for sheath limited filament advection assuming an invariant parallel gradient of density,

$$\frac{v_E}{C_s} \sim 2\left(\frac{l_\perp}{R_0}\frac{\tilde{n}}{n_0}\right)^{\frac{1}{2}}, \tag{3.2}$$

for filament advection in the absence of limiting parallel currents assuming $\frac{\tilde{n}}{n_0} \ll 1$ and

$$\frac{v_E}{C_s} \sim 2\left(\frac{l_\perp}{R_0}\right)^{\frac{1}{2}} \tag{3.3}$$

in the case of $\frac{\tilde{n}}{n_0} \geq 1$. We also find a new solution for the sheath limited case assuming an invariant target density,

$$\frac{\vec{v}_E}{C_s} = 2\frac{\rho_i^2}{l_\perp^2}\frac{l_\parallel}{R_0}\frac{n_b}{n_t}\hat{x}, \tag{3.4}$$

exact assuming dominant parallel currents for regions of constant negative curvature. In each case, the advective velocity of a filament v_E in the radial direction is given in terms of the sound speed $C_s = \sqrt{\frac{T_e}{m_i}}$, the ion Larmor radius ρ_i, perpendicular blob size $l_\perp$, length along magnetic field between divertor plates $l_\|$, radius of curvature of the tokamak R_0, blob density n_b, target density n_t, ratio of target and blob density $\xi = n_t/n_b$ and a filament density perturbation $\tilde{n}$ on a density background n_0.

Filament sizes are of the order few to tens of ion Larmor radius, temperature is of order tens of electron volts and the advective velocity of order kilometres per second [D'Ippolito et al., 2011]. Given fairly similar combinations of these parameters, any of the advective models (3.1), (3.2), (3.3) or (3.4) can show a favourable agreement with the observations, for example, taking $T_e = 30eV$, $\frac{\vec{v}_E}{C_s} \sim \frac{1kms^{-1}}{50kms^{-1}} = 0.02$, $\rho_i = 2mm$, $l_\| = 15m$, $R_0 = 0.85m$, $1/\eta = n_b/n_t \sim 5$, $\tilde{n}/n_0 \sim 1$ we find

$$l_\perp = \sqrt{2\frac{4e-6}{0.02} * \frac{15}{0.85} * 5} = 18.3cm, \tag{3.5}$$

for the sheath limited case and,

$$l_\perp = 0.0004 * 0.85 = 0.17mm \tag{3.6}$$

without sheath limiting. For these estimates, the sheath limited case seems more applicable, however, taking different estimates of $T_e = 10eV$, $\frac{\vec{v}_E}{C_s} \sim \frac{5kms^{-1}}{30kms^{-1}} = 0.17$, $\rho_i = 1.2mm$, $l_\| = 15m$, $R_0 = 0.85m$, $1/\eta = n_b/n_t \sim 5$, $\tilde{n}/n_0 \sim 0.5$ we find

$$l_\perp = \sqrt{2\frac{1.4e-6}{0.17} * \frac{15}{0.85} * 5} = 1.0mm, \tag{3.7}$$

for the sheath limited case and,

$$l_\perp = \frac{0.028}{0.5} * 0.85/2 = 2.4cm \tag{3.8}$$

without sheath limiting. These estimates appear more favourable to the interpretation without sheath currents.

There are numerous complicating effects to this interpretation of blob dynamics that should be noted: only laminar blob dynamics are considered, background turbulence is ignored, blob birth properties are untreated, parallel blob structure in $J_\|$ neglected, interactions between blobs are not considered, temperature profiles are ignored and a Gaussian blob shape is likely an oversimplification.

This demonstrates that an accurate discrimination between models, based on predicted values of radial velocity alone, is at best problematic. Another way to discriminate between these models, besides estimating velocities, can come from examining the scaling of the velocity of experimentally measured filaments with parameters such as $l_\perp$ and ρ_i, scalings of these parameters vary strongly between models, however experimentally measuring temperature to an adequate resolution can be problematic, as can the measurement of filament size which for single point measurements, the most readily available source of data, depends heavily on the plasma flow structure which again is problematic to measure at adequate resolutions and accuracy. We focus therefore on the scaling of (3.1), (3.2), (3.3) and (3.4) with plasma density. These solutions can be combined in a single expression, $v_E \propto F(\rho_i, l_\parallel, l_\perp)n^\alpha$. Four scenarios can be identified; each with a particular value of α:

1. the sheath case with $n_t = \xi n_b$, where v_r is not dependent on the filaments density and is large for small filaments, $\alpha = 0$ (3.1)
2. the sheath case with $n_t = const$, for which small and dense filaments are also the fastest, $\alpha = 1$ (2.74)
3. no sheath, small fluctuations model predicts large v_r for large filaments with density deviating strongly from the background, $\alpha = 0.5$ (3.2)
4. no sheath fully nonlinear model gives radial velocity proportional to the size, but independent of the filament density, $\alpha = 0$ (3.3).

The scaling exponent α will be determined directly from the experimental data.

3.1 Candidate Data Sets

To perform this study of the scaling of filament advection velocities, data are taken historically from experiments performed on the MAST tokamak. MAST is a spherical tokamak, in which a low aspect ratio equilibrium magnetic field is achieved by constructing the primary field coils inside the vacuum vessel, attached to a central column which acts as the main transformer. Such designs are highly compact, and have an inherently high variance of magnetic field strength with radius compared to conventional designs. The MAST vacuum vessel is $4.4m$ tall and $4m$ in diameter, with a plasma boundary, where closed fields lines transition to open ones, at a typically radius of $\sim 1.4m$. The principal diagnostic utilised is the Gundestrup probe, comprising a number of biased and unbiased Langmuir probes, which is mounted on the reciprocating probe system. This system is fixed to the mid-plane, that is, the plain which the magnetic axis resides upon. Fixed to an unimportant (for our purposes) angle about the central column of the tokamak, the reciprocating system is capable of measurement across most of the SOL ($r >\sim 1.4m$) and may reach a few cm inside the plasma boundary, limited by the maximum acceptable heat and particle fluxes to the probe head itself, which of course increase further inside the plasma boundary in an operating scenario.

Data from the Gundestrup reciprocating probe system on the MAST tokamak, schematically shown in figure 3.1, is used to evaluate the polodial electric field and density of filaments in discharge numbers 21712, 21856 and 21860. These discharges were chosen with the intention of investigating the scaling of the velocities predicted in section 2.3 with density while keeping the remaining plasma parameters the same. In summary these are: plasma current $I_p = 400kA$, torodial magnetic field at $1m$ $B_T = 0.4T$ and core electron temperature $T_{e_{core}} = 700eV$.

Figure 3.2 shows the profiles of electron density and temperature for the discharges, figure 3.3 shows the line integrated density and target densities. The magnetisation for MAST approaches a maximal value of 0.3, so that the models in section 2.3 are not violated in (2.65). Electric field is calculated from floating potential measurements V_f, and density is inferred via ion saturation current

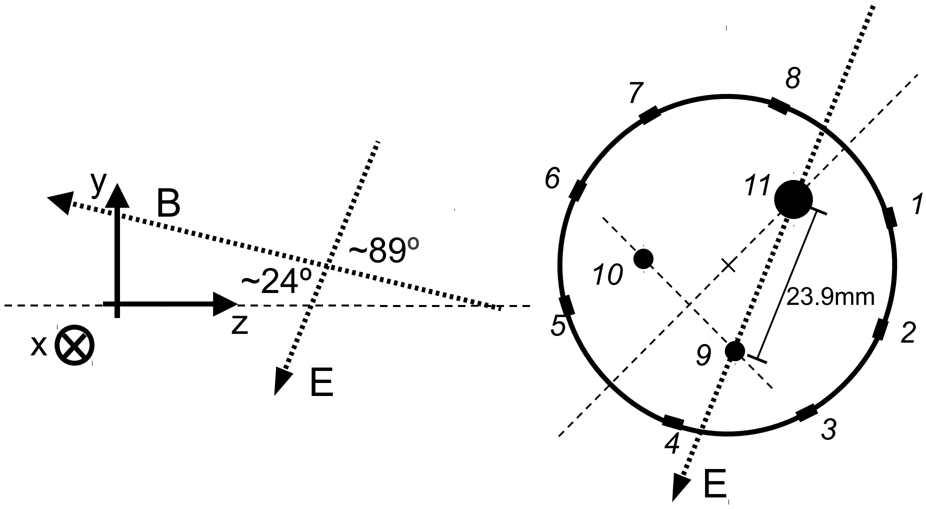

Figure 3.1: This is a diagram of the layout and pinouts of the Gundestrup probe system used on MAST [MacLatchy et al., 1992]. Pins 1 to 8 measure I_{sat} while pins 9 to 11 measure V_f.

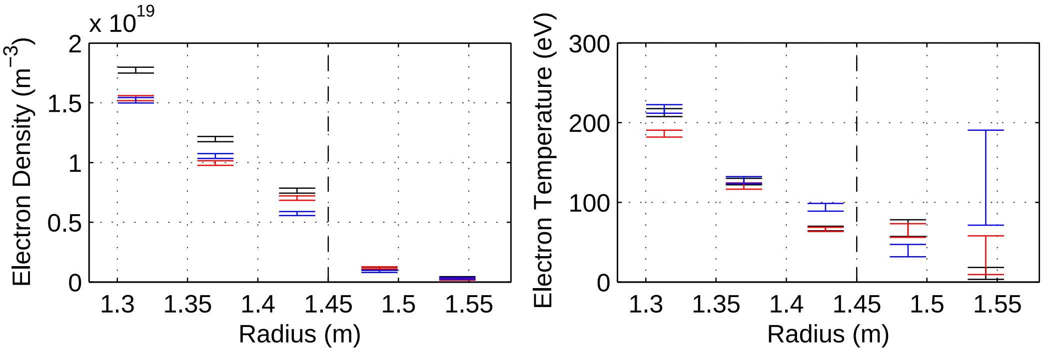

Figure 3.2: Electron density and temperature profiles from the Ruby Thompson Scattering system [Walsh et al., 2003]. 21712(black), 21856(red), 21860(blue). Dashed line gives LCFS position approximately.

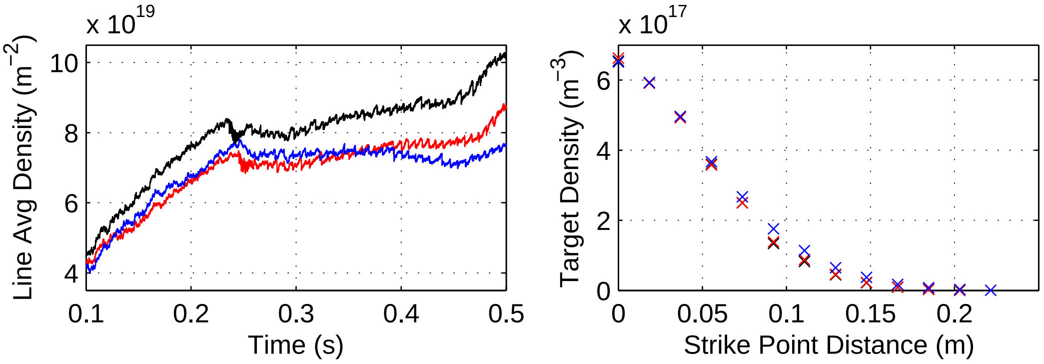

Figure 3.3: Line integrated electron density from the CO2 interferometer system, Target electron density around $0.29s, 0.31s$ (lower target, outer strike point). 21712(black), 21856(red), 21860(blue).

measurements I_{sat} [Tamain et al., 2010],

$$V_f = V_p + \frac{T_e}{2e} \ln \left[2\pi \frac{m_e}{m_i} \left(1 + \frac{T_i}{T_e} \right) \right] \tag{3.9}$$

$$I_{sat} = en_e \sqrt{k_b \frac{(T_e + Z\gamma_i T_i)}{m_i}}, \tag{3.10}$$

where γ_i is a constant which depends on the ion equation of state. In figure 3.4, the raw V_f signals are shown.

3.1.1 Pre-processing of Experimental Data

The reciprocating probe system allows measurement of the probe data across a radial range, signals are pre-processed as follows:

1. Smoothing LCFS distance data – Probe distance to LCFS vs time is given from EFIT [Uesugi et al., 1985] and RP systems. This data is multivalued on small scales; in order use the data to interpolate between radial position and distance from the LCFS, the data is smoothed over $0.04s$.
2. V_f mean trend removal – There is a mean trend in floating potential data due to (at least) the radial electric field and radial temperature profiles. This is removed using a piecewise linear detrend with a time window of $1.\dot{6} \times 10^{-4}s$ (larger than the timescale associated with blobs).
3. V_f response correction – The floating potential signal from pin 11 has a different response in amplitude. This is due to the difference in surface areas. To correct this, the signal is multiplied by a constant such that the standard deviation over a scale of 0.02s for both signals are equal.

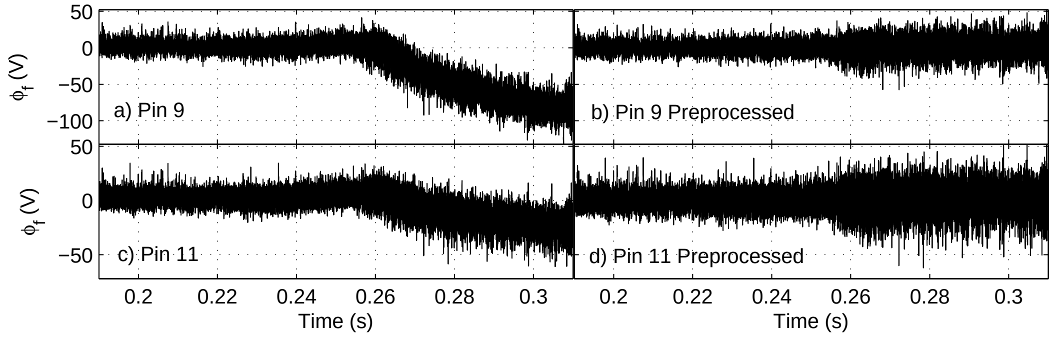

Figure 3.4: Traces of floating potential before (left) and after (right) pre-processing.

The polodial electric field E_θ (corresponding to the $\vec{E} \times \vec{B}$ drift) is calculated between pins 11 and 9 (see figure 3.1). Figure (3.5) shows traces of the I_{sat} derived electron density, and electric field data after pre-processing. The intermittent bursts in the two signals are interpreted as signatures of filamentary transport.

The electric fields are not obviously correlated with the density; this is no surprise given the phase distribution in figure 4.6 for the SOL using this probe. This may purely be due to strong electron temperature gradients, as discussed in chapter 3. The magnitudes of the electric fields give radial velocities on the order of

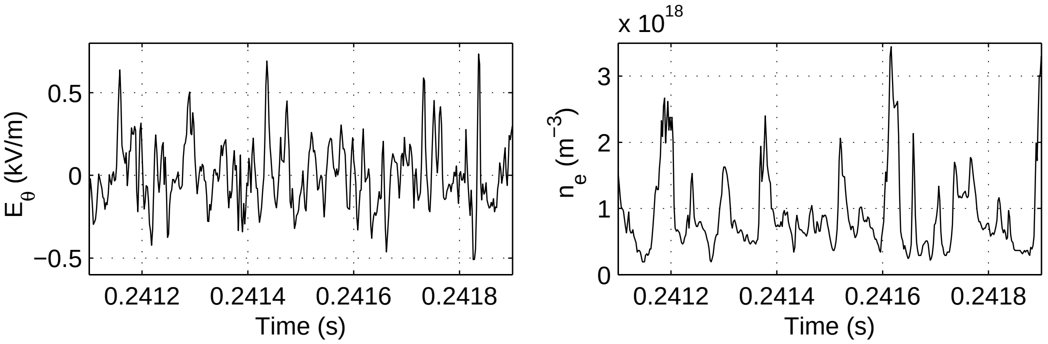

Figure 3.5: Peaks in electric field (left) and ion saturation current (right) are interpreted as signatures of filaments. Temperature of $20eV$ assumed to find n_e from the I_{sat}.

kms^{-1}, which is approximately the expected value for MAST L-Mode [Ayed et al., 2009]. It is clear that an indirect method will be needed if we are to examine any scaling with filament density, since it would be problematic to match filaments on a one to one basis from each signal. Also, a direct method would be likely to fail since it is difficult to determine if a variation in I_{sat} is a variation in n_e or $\sqrt{T}$, and to determine by how much each electric field is altered by electron temperature gradients. The indirect approach we choose will make use of two datasets, in which the plasma density is marginally altered. In this case, we will be able to use average methods to determine on average the effect of the change in density, under the assumption that any changes in velocity are purely due to this change in density.

3.1.2 The Strength of Fluctuations in MAST

At this point, we would like to address the validity the local approximation

$$n = n_0 + \tilde{n}, \quad |n_0| \gg |\tilde{n}|, \quad n_0 = f(x) \tag{3.11}$$

with respect to the strength of the nonlinearity $\tilde{n}/n_0$, since it will determine which solution (3.2) or (3.3) is most valid. Often its application is split into two parts that can be generalised as

$$\partial_y n = \partial_y (n_0 + \tilde{n}) = \partial_y \tilde{n}, \tag{3.12}$$

$$n = (n_0 + \tilde{n}) = n_0. \tag{3.13}$$

Actually, (3.12) is simply a change of reference value. One can subtract any constant value n_0 from any function to represent it about another mean value, without changing the gradients in any way. (3.13) however, should only be applied if $n_0 \gg \tilde{n}$ is satisfied to a few orders of magnitude; even for $\tilde{n}/n_0 \sim 0.1$ this would misrepresent the data by 10%. We address the approximation applied to the equation (3.2),

$$\vec{v}_E \cdot \vec{\nabla} \left| \vec{\nabla} \times \vec{v}_E \right| = -2 \frac{C_s^2}{n} \frac{1}{R_0} \frac{\partial n}{\partial y}. \tag{3.14}$$

Now decomposing the density into two parts and writing gradients as length scales,

$$\frac{v_E}{C_s} = 2 \sqrt{\frac{l_\perp}{R_0} \frac{\tilde{n}}{\tilde{n} + n_0}}. \tag{3.15}$$

We are interested in the proportionality to density, so we simply write

$$v \propto \sqrt{\frac{\tilde{n}}{\tilde{n} + n_0}}, \tag{3.16}$$

and evaluate

$$\alpha = \frac{\partial v}{\partial \tilde{n}} \frac{\tilde{n}}{v} \tag{3.17}$$

for $n_0 = 1, \tilde{n} = 0.01..10$ to find the scaling exponent as a function of the density fluctuation strength $F_n = \tilde{n}/n_0$; figure 3.6.

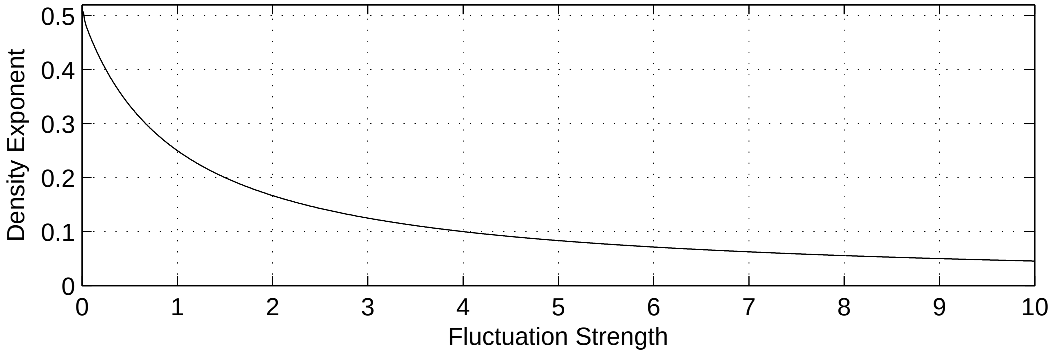

Figure 3.6: Change in velocity w.r.t. density for (3.16), giving the density exponent (α).

We see that for small F_n, a scaling with density of 0.5 is found as in (3.2). This decreases rapidly towards the index predicted by (3.3) as F_n increases. The question arises as to how to quantify F_n: For a single filament fluctuation above a density background, one might quantify F_n as the ratio of peak height to background level, $max(n)/min(n) - 1$. Or, an average F_n may be used such as the ratio of standard deviation to average value. An understanding of the functional dependence of the density scaling with these types of measurements of F_n is required, as the methods take extremely different values as shown in figures (3.7) and (3.8).

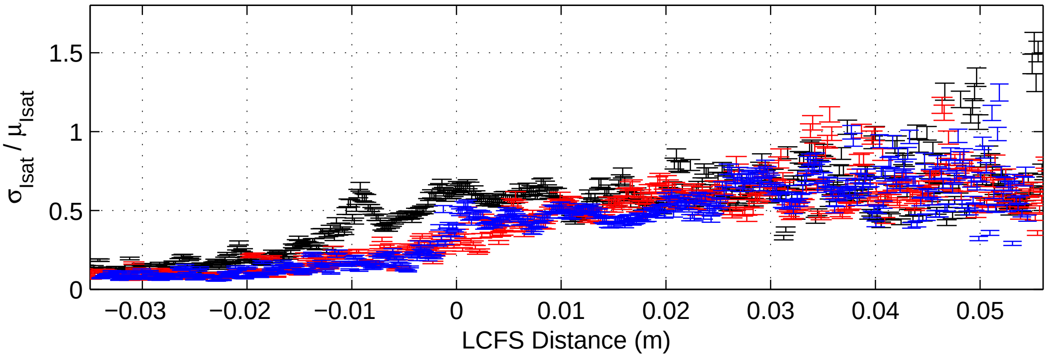

Figure 3.7: Strength of $\tilde{n}$ w.r.t. n_0, measured by the ratio of standard deviation to mean value. Calculated from #21712 data, subintervals of $4e-4s$.

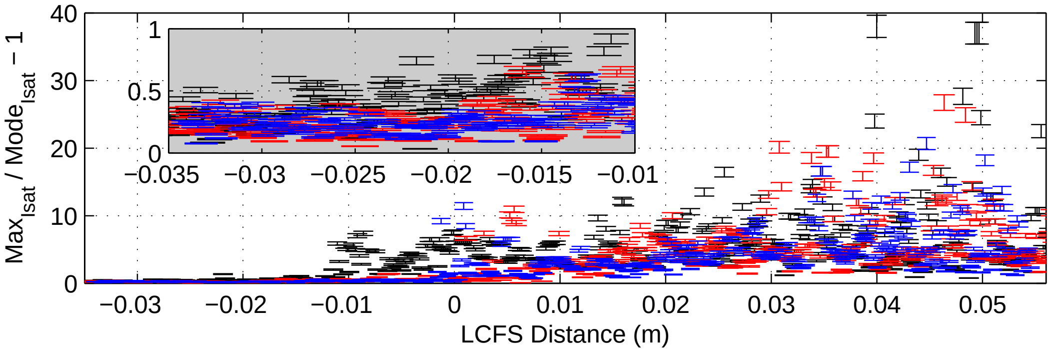

Figure 3.8: Strength of $\tilde{n}$ w.r.t. n_0, measured by the ratio of maximum value to modal average value. Calculated from #21712 data, subintervals of $4e-4s$.

In order to determine the mapping of these methods to the plot in (3.6), a method must be used that determines velocity from a density profile, that these methods may be applied to. Equation (3.14) is a two dimensional nonlinear boundary value problem and as such would be particularly expensive to solve numerically, to the point that the explicit evolution of the initial value problem specified by (2.57) and (2.58) (with $\nabla_\parallel J_\parallel = 0$) becomes a more attractive approach to solve the problem. Since only the scaling of v_E with particular density profiles in n are of interest, we approximate (3.14) as

$$v_x \frac{\partial^2 v_x}{\partial y^2} \propto \frac{1}{n} \frac{\partial n}{\partial y}, \tag{3.18}$$

and, given given particular profiles of $f(y)$, solve for the velocity profile $v_x(y)$ using an over-relaxed finite difference (Gauss-Seidel) iteration scheme [Press, 1992] with the i^{th} discretised point in the y direction written as i and grid spacing Δ,

$$v_x(i) = (\omega - 1.0)\, v_x(i) + \frac{1}{2}\sqrt{v_x(i)\left[v_x(i+1) + v_x(i-1)\right] - \frac{1}{2}\Delta \ln\left(\frac{n(i+1)}{n(i-1)}\right)}, \tag{3.19}$$

which is found to converge to the principal root for $n_y = n_0 + \tilde{n}\exp\left(-y^2\right)$ with $\omega = 1.9$. Solutions are dipolar in velocity, max value is selected as advection velocity. No structure except boundary values is enforced on solution in y. We scan values of F_n by finding the peak value of the converged velocity profiles v_c for $n_0 = 1.0$ and a range of $\tilde{n}$ of 0.1 to 20, as shown in figure 3.9.

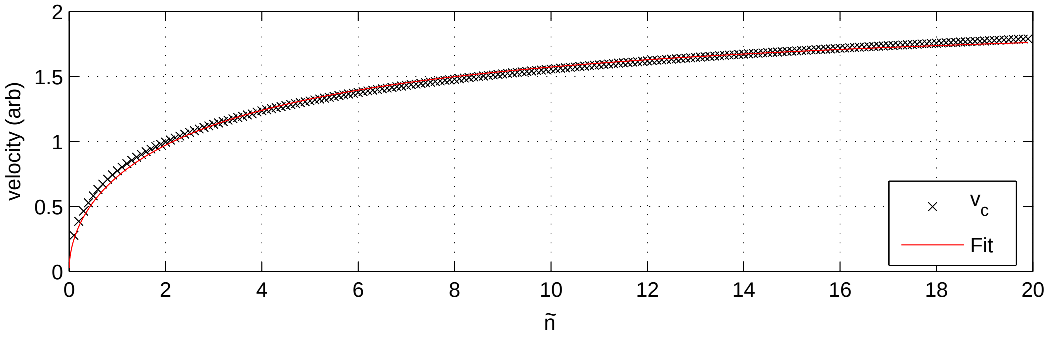

Figure 3.9: Converged velocity values v_c plotted as a function of $\tilde{n}$ ($n_0 = 1$ fixed). Fitted to $k\sqrt{\frac{\tilde{n}}{\tilde{n}+c}}$ for $k = 2.041, c = 6.854$.

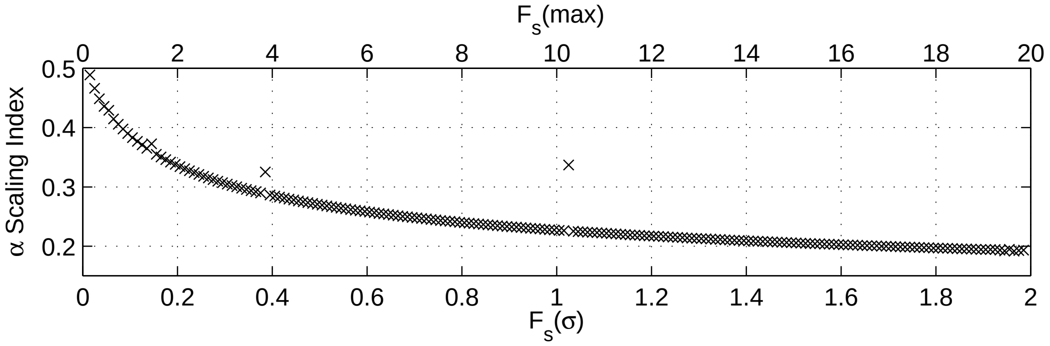

Figure 3.10: α scaling index calculated from (3.17) for v_c, against $F_n(\sigma)$ and $F_n(max)$.

There are small jumps in the velocity profile at some thresholds in $\tilde{n}$, evident when calculating (3.17); figure 3.10 shows the result of calculating the scaling index

(3.17), which we will denote α, in which there are a few points that do not fall onto the curve due to the small jumps in the velocity profile, these are likely due to changing accuracy conditions in the method that are difficult to constrain; a large fixed number of iterations, 1×10^8 was used to converge on the velocity solution, this however, does not fix the accuracy although the error is very small after this number of iterations. The curves are plotted with the σ/μ measure denoted $F_n(\sigma)$ and the $max/min - 1$ measure denoted $F_n(max)$, and we find that the two methods do indeed quantify the expected scaling very differently, with an expected α for MAST in the region of 0.25 as shown in figure 3.10, taking into consideration figures (3.7) and (3.8).

3.2 Methodology use to find the Velocity/Density Scaling

In order to study the advection mechanisms we investigate the scaling of radial $\vec{E} \times \vec{B}$ velocity with filament density. We have chosen a statistical method in which the signals are windowed (split into sections) and the average properties of these windows are used as average properties of the filaments inside the window. Such a method does not rely on both signals (I_{sat}, E_θ) containing the same set of filaments, and is valid as long as the separation of the V_f pins used to calculate E_θ is smaller than the polodial size of the filaments measured. The validity of this assumption is supported by fast camera measurements in [Ayed et al., 2009], where the most likely filament width was found to be $\approx 10cm$, compared to the pin separation of $\approx 2.4cm$ in the polodial direction. The auto correlation time of the I_{sat} signal is around $50 - 100\mu s$, which assuming a conservative filament velocity magnitude of $1kms^{-1}$ gives a filament size of $\approx 5 - 10cm$, in agreement with the fast camera measurements.

A generalised model is given in (3.20), where F is a function that depends on the advective model. The subscripts high and low refer to the pair of discharges being compared, where the "high" discharge has a larger density profile in the SOL than the "low" discharge.

$$\frac{\langle v_{E,high} \rangle}{\langle v_{E,low} \rangle} = \frac{\left\langle F_{high}\left(\rho_i, l_{\parallel}, l_{\perp}\right) n_{high}^{\alpha} \right\rangle}{\left\langle F_{low}\left(\rho_i, l_{\parallel}, l_{\perp}\right) n_{low}^{\alpha} \right\rangle}, \tag{3.20}$$

where $\langle \cdot \rangle$ indicates averages over all times in a window. We will assume that all the arguments of F are independent (including ρ_i and n) so that for example,

$$\left\langle \frac{\rho_i l_{\|}}{l_{\perp} R_0} \right\rangle = \frac{\langle \rho_i \rangle \left\langle l_{\|} \right\rangle}{\langle l_{\perp} \rangle \langle R_0 \rangle}. \tag{3.21}$$

Examining the co-dependence of B, T, n in plasma filaments would be a good subject for future work. Thus we write equation (3.20) as

$$\frac{\langle v_{E,high} \rangle}{\langle v_{E,low} \rangle} = \frac{F_{high}\left(\langle \rho_i \rangle, \left\langle l_{\|} \right\rangle, \langle l_{\perp} \rangle\right)}{F_{low}\left(\langle \rho_i \rangle, \left\langle l_{\|} \right\rangle, \langle l_{\perp} \rangle\right)} \frac{\left\langle n_{high}^{\alpha} \right\rangle}{\left\langle n_{low}^{\alpha} \right\rangle}. \tag{3.22}$$

We assume that phase of density and temperature fluctuations in (3.10) satisfies $I_{sat} \propto n$. The parameters specified by F in (3.22) for all analysed plasmas are: $\rho_i = 1.5mm$, $C_s = 43.8kms^{-1}$, $R_0 = 0.85m$, $l_{\perp} = 5 - 10cm$ and $l_{\|} = 15m$. Hence equation (3.22) simplifies to read

$$\frac{\langle v_{r,high} \rangle}{\langle v_{r,low} \rangle} - \frac{\left\langle n_{high}^{\alpha} \right\rangle}{\left\langle n_{low}^{\alpha} \right\rangle} = 0. \tag{3.23}$$

The average value for the signal dominated by large events (filaments) is not representative of the data. We use a peak detection algorithm to identify the peak value of filaments and then use only these values in each window. Peak values for each window are obtained by taking the maximum value for each section of the signal that rises above the mean value in the window. Since the high density and low density discharges have differing density profiles in the SOL, the radial profiles $< n_{high} >$ and $< n_{low} >$ will differ in a similar manner. Averages $\langle \cdot \rangle$, now taken as the average over all peaks in a window, do not take into account any correlation between density and velocity; it is not assumed that such correlation can be found, making the method very simple and having an error that depends on the number of peaks averaged over.

In order to find α we calculate the LHS of (3.23) in each window as a function of α using only the peak values as described. α is then given as the value that most closely satisfies (3.23). The equality is tested between $\alpha = 3.0$ and $\alpha = -3.0$ with a step of 0.01. Errors for the average peak values in each window are estimated by $\sigma_{peaks}/\sqrt{N_{peaks}}$ from central limit theorem, and the error in α is then interpolated using these errors in the previously calculated function of α.

We stress, that this method does not eliminate a possibility of erroneous E_θ calculations or the presence of unknown scaling of $\vec{v_E}$ with unmeasured quantities, which would also effect a single filament method. The filaments with a polodial size less than the pin separation measuring V_f will give erroneous field measurements unrelated to a blob advection velocity. This problem may be expected to worsen toward the far SOL, since filamentary structures are known to fragment into smaller filaments as they propagate (especially in the case of a vortically dominated advection) [Garcia et al., 2005]. In the sheath case, the smaller filaments propagate faster, so that one may expect to find a large population of small filaments in the far SOL.

3.3 Determined Scaling

Results for the radial velocity and I_{sat} window-averaged peak detections are shown in figure 3.11, and magnitudes of the measured radial velocities are in qualitative agreement with using fast camera measurements [Ayed et al., 2009]. The variation in peak I_{sat} between the candidate data sets is clear, and the averaged radial velocity peaks do also show a variation so that a finite profile for the α scaling parameter is to be expected after comparison of the datasets using (3.23). To be clear, the process does not amount to the division and comparison of the profiles displayed in figure 3.11, since raising the peak density values to α must be done before the averaging operation. We do not assume that the power and average operators commute, as discussed in the previous section.

Figure 3.12 shows α computed from (3.23) as a function of distance from the last closed flux surface for the entire range of spatial locations experienced by the reciprocating probe. However, it is clear that this method fails when the probe plunges into the bulk plasma. In this case, the estimated α index decreases rapidly and assumes negative values. Figure 3.11 shows that the falling trend of α inside the LCFS is due to a crossing of the average electric field peak values at $\approx -0.01m$. In [Sánchez et al., 2000] the same trends for v_E inside the LCFS are found on different machines, and were attributed to shear flows; the methodology discussed here is not applicable to such situations. The interaction of blobs and shear flows is discussed for example in [Xu et al., 2009].

Temporal window sizes are chosen to have equal spatial widths using probe time-position data from EFIT. We have tested the method against various window sizes as shown in figure 3.12, where width of $0.005m$ was chosen as a compromise between resolving changes in the α parameter in the SOL and having windows large enough to contain enough data for satisfactory statistical averaging.

Figure 3.13 contains the main results of our analysis. It shows the scaling exponent α, derived from window averages of V_f and I_{sat}^{α}, as a function of radial distance from the LCFS. The result does not imply a single mechanism to be responsible for the transport in the SOL of MAST, but suggests that the filaments

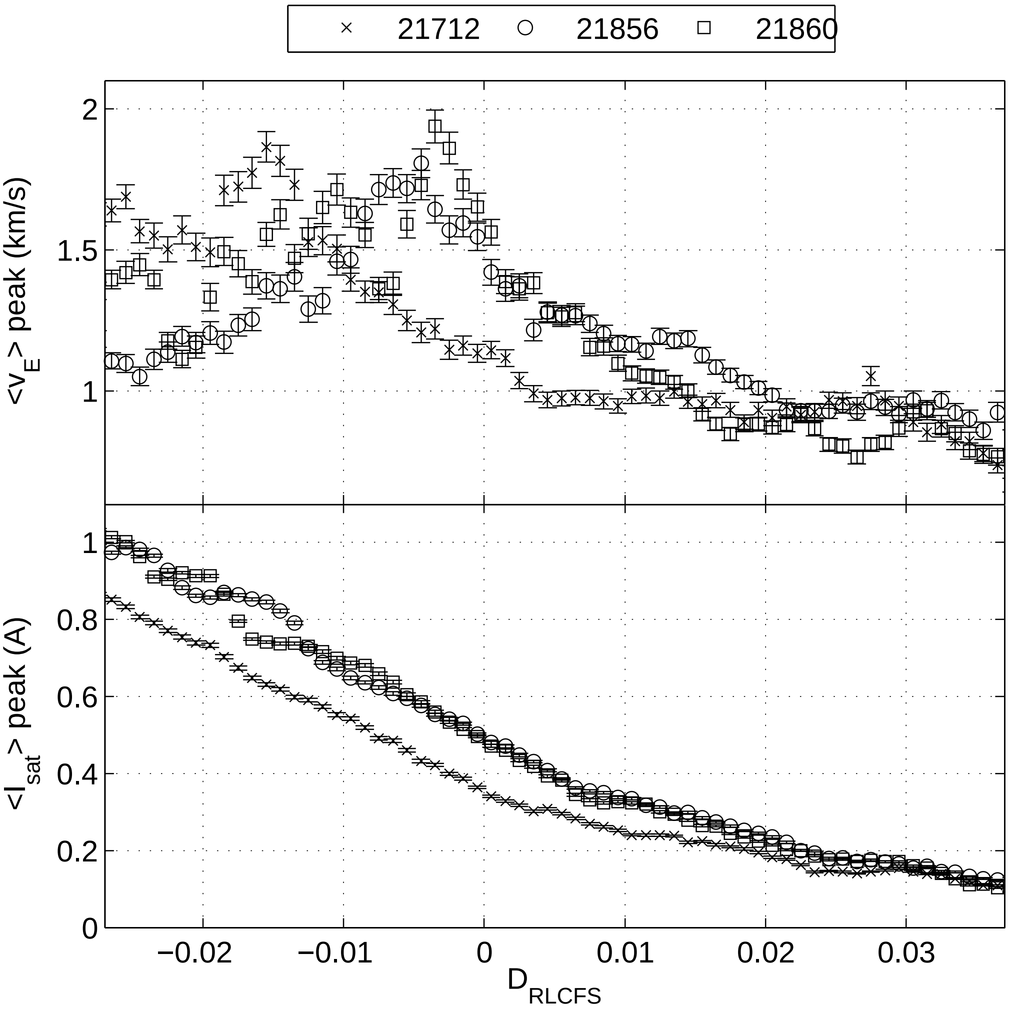

Figure 3.11: I_{sat} and radial v_E peak averages. Inside the LCFS, the electric field trends do not match (and in-fact cross) causing negative results for the scaling exponent α, plotted in figure 3.12. Given for window width of 0.005m.

experience different mechanisms in different SOL regions.

We find the general trend of $\alpha \approx 0.5$ at $0.0m$ to $\alpha \approx 1.0$ at $0.007m$ followed by a trend of $\alpha \approx 0.5$ to $\alpha \approx 0.0$ from $0.01m$ to $0.025m$. Beyond $0.025m$ α assumes negative values; mildly for 21712/21856 and strongly for 21712/21856. Scaling trends show disparity for the two comparisons beyond $0.01m$. Further out at $\approx 0.03m$ scalings become difficult to interpret due to the proximity of the I_{sat} window peak averages to each other.

From figure 3.10 we suggest that solutions of type (2.71) and (2.72) are

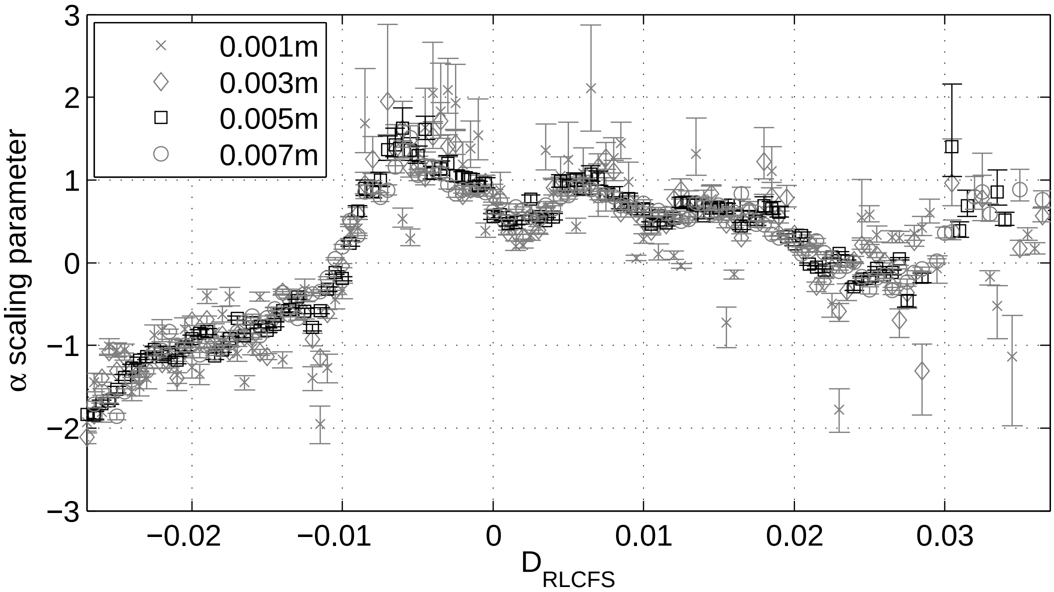

Figure 3.12: α parameter for various window sizes demonstrating the convergence of the method, given for shot 21712 compared to 21856. A window size must be chosen that allows for spatial variation of the parameter in the SOL, and that contains enough data to provide a good statistical average.

both extremes, and the expected α will, for F_n typical of MAST, take a value of approximately 0.25. Each window may contain filaments that are propagating under different mechanisms, therefore intermediate values of α should be interpreted to reflect this fact.

It may not be clear how filaments can be controlled by sheath currents near to the LCFS, since the time to set up a connection to the sheath at the target plates might go as $l_{\|}/C_s = t_{\|i} \approx 3.1 \times 10^{-4} s$ which is large compared to the perpendicular transport time $l_{\perp}/v_r = t_{\perp} \approx 5 \times 10^{-5}$. However if we consider the parallel transport time with the electron sound speed we find $t_{\|e} \approx 7.3 \times 10^{-6}$, small enough to be a possible cause of sheath connected perpendicular transport. Indeed, we find a maxima of α at $0.007m$ which is comparable to $v_{\perp} t_{\|e} \approx 10^3 \times 7.3 \times 10^{-6} = 0.0073m$. A discussion of kinetic parallel electron transport in the SOL can be found in [Tskhakaya et al., 2008].

3.4 Summary

We have tested four possible mechanisms leading to fast radial filament transport using MAST probe data. The mechanisms are parametrised by a single scaling

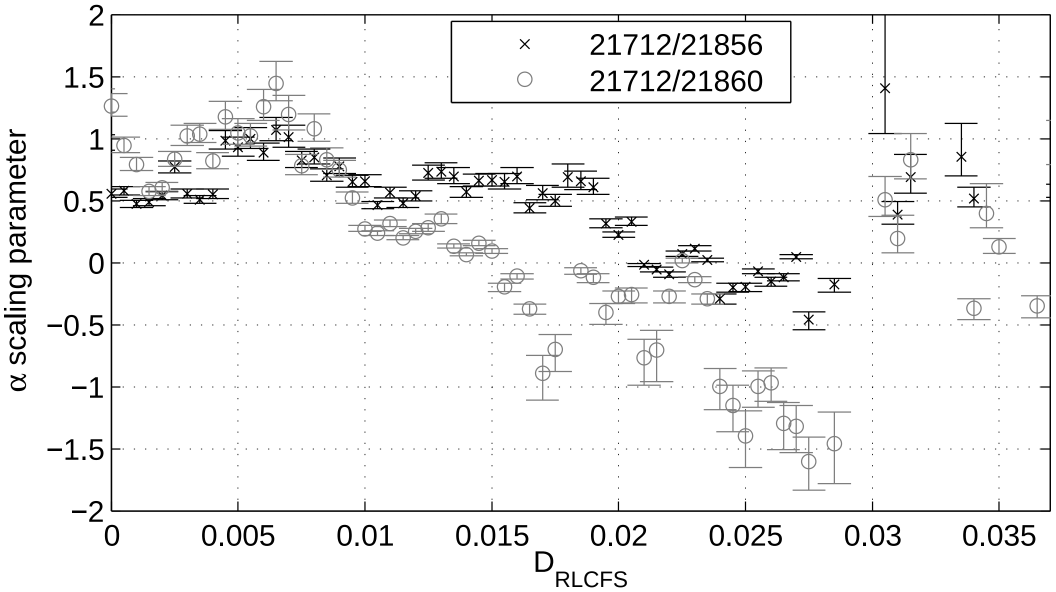

Figure 3.13: The α scaling parameter as a function of radial distance from the LCFS. A peak value of $\alpha \sim 1$ is reached at $\sim 0.007m$, indicative of sheath limited blob advection under constant target boundary conditions (3.4). In general, a range of the blob advection mechanisms discussed in chapter 2 appear to govern the blob advection, depending at least on the radial distance from the plasma LCFS.

exponent α which in ideal cases can assume values of 0, 0.5 or 1. The statistical approach developed here is particularly useful for the analysis of the large Langmuir probe datasets which are readily available on many fusion devices. This study complements that presented in [Ayed et al., 2009] where visible light camera datasets were used to perform a similar scaling analysis. Our main result is an estimate of the scaling exponent α for MAST datasets as a function of distance from the LCFS. Strong variability of α across the entire range of measured distances indicates that no single model can be invoked when describing radial blob advection. Instead, we interpret our result as a competition between one sheath dominated model (α = 1) and either a model given by fully nonlinear dynamics with neglected parallel dynamics or a second sheath dominated model (α = 0). Detailed analysis of the models that balance the advection of plasma vorticity with the plasma interchange term, leading in extreme cases to an α of 0 or 0.5, reveals that for the fluctuation strength associated with blobs on MAST, an intermediate value of $\alpha = 0.25$ may be the most appropriate. In the region where sheath dynamics appear to dominate (about $0.75cm$ from the bulk plasma), our observations imply that the plasma density on the target is approximately constant; not related directly to the plasma density inside the filament. We conclude that the parallel plasma behaviour must be much more dynamic than previously thought, if such a connection between plasma density at the divertor sheath and mid-plane in filaments can be so strongly nullified. We also conclude that the nature of the sheath connection of the filament via parallel currents may be kinetic, since the communication of potential appears to happen on the electron thermal timescale.

The statistical method used here is limited to examining a pair of datasets with variance in only one parameter (density). In reality, such a variance is hard to come by without altering other parameters, severely limiting the methods applicability. The models examined are also very basic models for blob advection that assume equilibrium laminar flow to the first order, and competing effects such as blob acceleration , interactions, parallel structure, to name a few may also damage the methods applicability.

Chapter 4

Blob Phase Analysis

Steep density and temperature gradients are key features of magnetically confined plasma (MCF) in a tokamak configuration. In the presence of a strong confining magnetic field, these gradients lead to a nonlinear transport of plasma across the magnetic field, towards the edge of the confinement region. There is a substantial body of evidence, from a variety of numerical simulations, analytical models and experimental observations, that this transport is dominated by nonlinear advection of filamentary structures; for a recent review of the field see [Krasheninnikov et al., 2008]. This applies to parts of edge pedestal as well as to a vacuum region just outside the last closed flux surface (LCFS) known as the Scrape-Off Layer in a tokamak. Drift instability is believed to be the main generation mechanism for large density and potential fluctuations in the edge pedestal and the drift-like dynamics is often taken as the main ingredient of cross-field transport in this region. In the SOL region it is the interchange transport, driven by the gradient in the magnetic field strength, that appears to be a dominant feature. In principle, however, both mechanisms would contribute to radial convection of filamentary structures in both regions of plasma and here we use Mega Amp Spherical Tokamak (MAST) [Lloyd et al., 2003] probe measurements to investigate the relative importance of these two mechanisms, and some additional transport scenarios, considering the relative generalised phase difference, θ_{nv}, between density and radial velocity fluctuations. The phase difference is a standard quantity used in linear analysis, however, when strong nonlinearities produce filaments, the velocity and density fluctuations are often functionally different, leading to a failure of the linear predictions. In this chapter, we develop techniques that robustly measure the phase difference in the nonlinear regime. We note that the phase difference between density and radial velocity fluctuations is not only a useful characteristic of transport mechanisms, but is also key to estimates of particle flux (and assuming a high coherence of plasma density and temperature, heat flux), since θ_{nv} is used to estimate the statistical correlations [Carreras et al., 1996]. However, our primary goal is to determine which mechanism, drift or interchange, is responsible for the transport of the blobs.

4.1 Introduction

The prototypical description of strongly magnetised plasma transport is usually given in terms of vorticity equation [Garcia et al., 2006a, 2005, 2006b; Kube and Garcia, 2011; Krasheninnikov, 2001; Yu et al., 2006; Furno et al., 2011; Sugita et al., 2012; Higgins et al., 2012; Angus et al., 2012], which reads:

$$\frac{\partial \nabla_\perp^2 \phi}{\partial t} + \left(\frac{\hat{z} \times \vec{\nabla}_\perp \phi}{B} \cdot \vec{\nabla}_\perp \right) \nabla_\perp^2 \phi = -2 \frac{B^2}{n m_i} \frac{\partial B^{-1}}{\partial x} \frac{\partial (nT)}{\partial y} + \frac{e B^2}{n m_i} \nabla_\parallel J_\parallel . \tag{4.1}$$

Here, vorticity defined as $\vec{\Omega} = \vec{\nabla} \times \vec{v}$ is expressed in terms of electrostatic plasma potential as $\nabla_\perp^2 \phi \hat{z}$, x and y axis corresponds to radial and polodial directions in cylindrical geometry, respectively. Two terms on the right hand side of (4.5) reflect two distinct physical process which govern any relation between density and potential fluctuations. The first term, representing a drift due to magnetic field curvature is often referred to as ballooning or interchange term. The second term, related to parallel current, is known as a drift term for edge plasma with flux surfaces (closed magnetic field lines), or sheath term when magnetic field lines connect to material surfaces, although a sheath term does not necessarily dominate the parallel current and may compete with a drift term in this region [Angus et al., 2012]. Thus parallel dynamics requires a closure that must be based on physics applicable in various plasma regions. We will now examine the theoretical phase difference θ_{nv} for the drift and interchange mechanisms in the presence of both linear and nonlinear fluctuations.

4.1.1 Linear fluctuations

In the case of the linear interchange fluctuations, parallel currents are generally neglected or approximated in the SOL by

$$\nabla_\parallel J_\parallel = e n \frac{C_s}{l_\parallel} \left(1 - \exp \frac{e\phi}{T_e} \right) \tag{4.2}$$

where the parallel velocity is bounded at the ion sound speed at the material surfaces intersected by the magnetic field, and the electrons are treated adiabatically.

There are two relevant limits of the interchange dynamics, as given by (4.1) which minimally describe the relation between density and electrostatic potential. In the absence of parallel currents, there is an approximate relation of

$$\text{CASE I:} \qquad \partial_y^2 \phi \propto -\frac{1}{n}\frac{\partial n}{\partial y}, \tag{4.3}$$

assuming no variance in the x-direction, since growth rate will remain proportional to value in this case. When sheath currents dominate, a scenario which may be applicable to SOL transport, and assuming $\frac{e\phi}{T} \ll 1$, we have

$$\text{CASE II:} \qquad \phi \propto \frac{1}{n}\frac{\partial n}{\partial y}. \tag{4.4}$$

We will refer to these limits, that is equations (4.3) and (4.4) as Case I and Case II respectively. Equation (4.3) is obtained by balancing terms 2 and 3 of equation 4.1 in a limit where terms $\propto \partial_x \phi$ may be neglected, whereas equation (4.4) is obtained by balancing terms 3 and 4 of equation 4.1, where $\vec{J}_\parallel$ is described by the sheath boundary conditions 4.2 in the limit of $e\phi \ll T_e$.

Linear theory predicts no phase difference between $\vec{v}_r \propto -\partial_y \phi \hat{r}$ and n for the interchange, given sinusoidal profile of density. This is evident on substituting $n = n_0 + \tilde{n} sin(y)$ into (4.3) or (4.4), taking n_0 which has no polodial dependence and assuming small fluctuations so that $\tilde{n}/n_0 \ll 1$, known as the local approximation of turbulence.

In the edge pedestal a resistive current, arising from ion-electron collisions, is used in the form

$$\nabla_\parallel J_\parallel = \nabla_\parallel \frac{T}{\eta_\parallel e}\left(\frac{\nabla_\parallel n}{n} - \frac{e\nabla_\parallel \phi}{T}\right). \tag{4.5}$$

For the pure drift system, the interchange term of (4.1) is neglected, and, for a pure drift wave with adiabatic electron response, that is when $n \approx \phi$, the phase θ_{nv} is 90 degrees. The relative phase between n and ϕ is, however, modified by the inclusion of parallel resistivity, which leads to equation (4.5) and in such case this this phase difference fall in the region of $30 - 45$ degrees [Horton, 1999], corresponding to a range of $60 - 45$ degrees for θ_{nv}. In both cases, density fluctuations lead potential perturbations and the direction of propagation coincides with the electron diamagnetic drift. This is important for correct interpretation of experimental results: polodial flow direction must be known to place the relative phase shift of n and ϕ at positive or negative range of angles.

4.1.2 Full Nonlinearity

Since drift waves and linear interchange fluctuations exhibit phase differences that occupy a different range of values, θ_{nv} offers a robust way to discriminate between these mechanisms. The local approximation however, is not a typical scenario for a tokamak SOL plasma. For MAST, $\langle \tilde{n}/n_0 \rangle \sim 1$ [Higgins et al., 2012] and a density filament may be described by $n = n_0 + \tilde{n} \exp\left(-x^2/2l_\perp^2\right)$. High $\tilde{n}/n_0$ modifies resulting potential profiles in such way that the concept of a linear phase difference is no longer applicable. Particular solutions for the simplistic cases I and II for radial velocity as a function of the y direction, $v_r(y)$, are given in figure 4.1. It must be noted that the solution in case I appears to be a unique case; in many studies e.g. [Garcia et al., 2006a] the velocity profiles $v_r(y)$ in the absence of sheath currents are, in fact, found to more closely resemble the profile given by case II in figure 4.1. Any such signature should be taken to be characteristic of the electrostatic interchange, and not unique to a sheath driven case or otherwise. The reason for this unique solution without local minima for case I shown in figure 4.1 is due to a complication arising from the assumptions of the equation (4.3); the vorticity, parametrised by the density gradient, is zero far from the blob. This yields a solution for potential that has a constant gradient far from the blob, thus a constant velocity in the negative $\hat{r}$ direction (n.b. the profile in figure 4.1 is valid up to a constant). In reality, velocity will be viciously damped far from the blob, however this effect is not included in our simple model, and, such an effect will yield a similar minima-maxima-minima structure of velocity about the density blob, for one example.

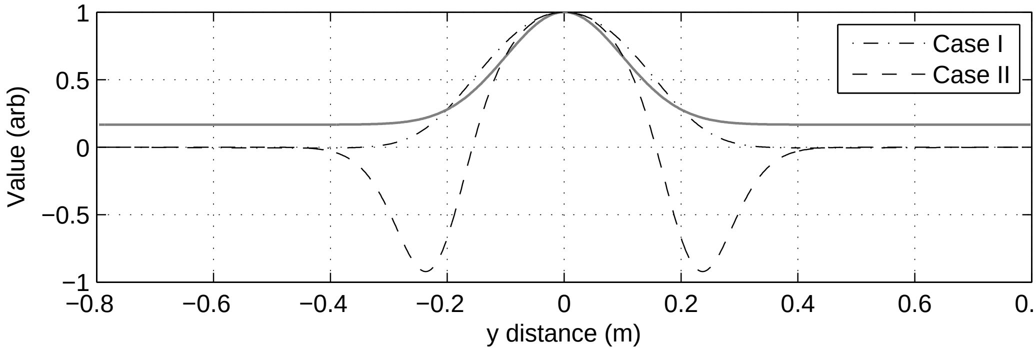

Figure 4.1: Density and velocity profiles for $\tilde{n}/n_0 = 5.00$ and $n = n_0 + \tilde{n} \exp\left(-x^2/2l_\perp^2\right)$ given for cases I and II.

It is apparent from figure 4.1, that the correlation between the density and potential of filaments will remain most coherent near the peak, and their proximity may be taken as a proxy of the linear phase. We will examine the validity of this statement in further detail in the following sections.

Simple approximate relations in the fully nonlinear scenario between potential and density, such as (4.3) and (4.4) are not as readily available for the drift wave case. However, we note that qualitatively the sign of θ_{nv} will still be fixed relative to the direction of propagation of the drift wave, and, for the drift wave instability to be a significant potential producing mechanism, the magnitude of the phase must be greater than zero, since the potential is always "produced" by the mechanism at a phase of 90 degrees.

4.1.3 Floating Potential

We finish with a short comment regarding an additional complication in establishing the relative phase between density and radial velocity, which applies equally to modelling and experimental observations. Standard tokamak Langmuir probes provide ion saturation current (I_{sat}), and floating potential (ϕ_f) measurements. The I_{sat} is proportional to density and will preserve its profile, providing temperature profiles are not radically different from those of density. Floating potential measurements, however, are given by $\phi_f \sim \phi - 2.5T_e/e$ [Wesson, 1987], with the last term modifying the velocity profiles by a factor of $2.5\partial_y T_e$. This effect will shift the phase angle away from predicted values, as we will show later.

4.2 Method

A typical method of estimating the phase difference between two signals uses the first order coherence:

$$\varphi = \cos^{-1}\left(\frac{\langle nv\rangle}{\langle n^2\rangle^{\frac{1}{2}}\langle v^2\rangle^{\frac{1}{2}}}\right), \tag{4.6}$$

Applying this estimator numerically for the Gaussian density function shown and a range of $\tilde{n}/n_0$ from 0.01 to 10, we find that case II gives an RMS phase far from zero, and case I gives an RMS phase that grows from zero as $\tilde{n}/n_0$ increases.

Using the same method for a conditional selection of the data where $v_r > 0$, which we will refer to this as thresholded RMS or tRMS, in both cases the phase begins at zero for small $\tilde{n}/n_0$ and increases smoothly to 10 degrees for a $\tilde{n}/n_0$ of 5, and onto 20 degrees for a $\tilde{n}/n_0$ of 10.

We would prefer to identify the interchange type behaviour with a zero phase, as we do with the linearised counterpart in order to distinguish it from other mechanisms therefore this is an improvement upon (4.6). The reason for this improvement is that the positive part of the velocity profile behaves closer to the linear regime than the negative parts - a trend that continues as the threshold is set to higher values, however resulting in increasing data loss. We note that for sinusoidal profiles, thresholding has no effect on the phase measurement, at all thresholds.

A more accurate measure of this central coherence is a relative position of density peak pk_n with respect to velocity peak, pk_v, that is $\delta y = pk_n - pk_v$, expressed as a fraction of the width of the density peak pk_w. Peaks are identified by using a threshold-based method. We set the threshold value to the mean of the signal and compute a local maximum for each section that exceeds the threshold value. These maxima provide the location of each density and velocity peak. The signed relative position between density and the nearest velocity peak is then calculated. A good estimate for pk_w is

$$pk_w = \sqrt{-\frac{\partial^2 n}{\partial y^2}|_{pk_n}^{-1} \times (n|_{pk_n})}, \tag{4.7}$$

which is exact assuming Gaussian density profiles, and allows error estimation by comparing second and fourth order approximations to the curvature and in the method, the phase is then approximated by

$$\theta = \frac{\delta y}{pk_w}, \tag{4.8}$$

measured in radians. This holds simply because the phase shift in a harmonic setting

$$\sin(k_y(y + \delta y)) = \sin(k_y y + \theta_{nv}), \tag{4.9}$$

gives the phase difference trivially as $\theta_{nv} = k_y \delta y$, with the width estimate pk_w simply related to the wave vector k_y by

$$pk_w = \sqrt{-{\frac{\partial^2 \sin(k_y(y + \delta y))}{\partial y^2}}^{-1} (\sin(k_y(y + \delta y)))} = \sqrt((k_y^2)^{-1}) = \frac{1}{k_y}. \tag{4.10}$$

Figure (4.2) shows the shift of the $-\partial_y \phi_f / B$ peak away from the density peak, due to temperature gradients, for nominal radial blob velocity of $1km/s$ mapped out against the blob size and peak blob temperature for cases I and II. We see that the phase shift including temperature profiles is likely to be in the region of 5 to 40 degrees, given moderate blob sizes and temperatures. For drift wave generated potentials, the phase shift due to temperature profiles will be zero in the case of an adiabatic response, and conservatively, a shift in the same direction by a similar amount for finite parallel conductivity; a diagram of these phase shifts is shown in figure 4.3.

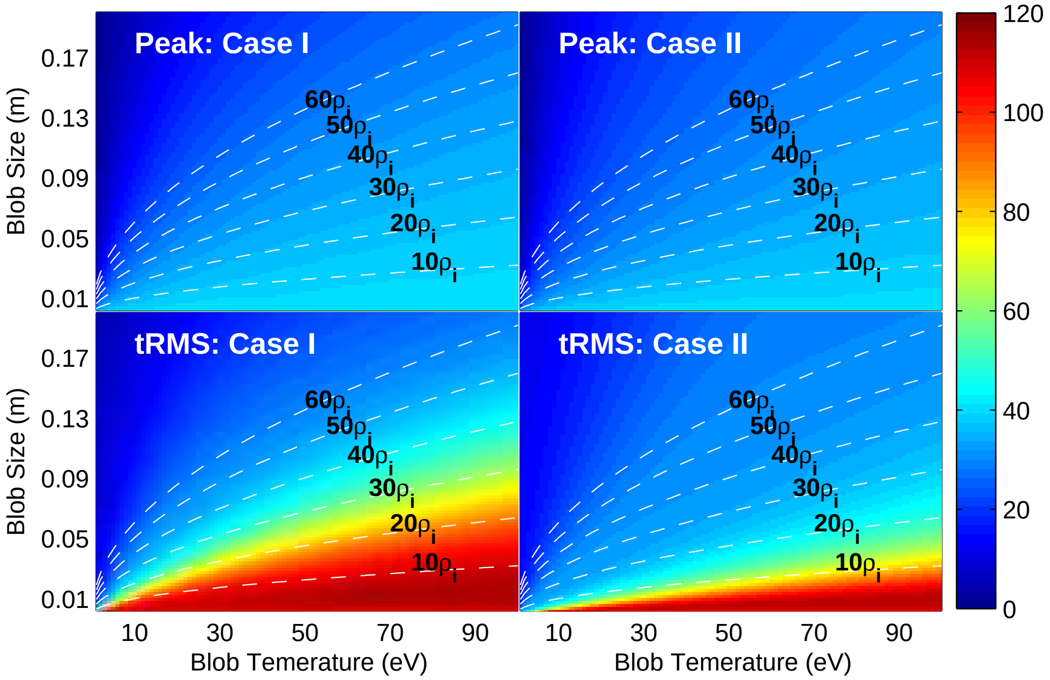

Figure 4.2: Phase shift found with the detection methods for test blobs parametrised by pressure width and peak temperature, given a blob radial velocity of $1km/s$. Peak refers to the peak detection phase method, and tRMS refers to the thresholded RMS method with an inclusive threshold of $v_r > 0$. For MAST, the phase shift θ_{nv} is estimated to, in general, contain a population in the range 5-40 degrees due to the effect of temperature gradients influencing the measurements. Results are displayed for: the peak method applied to data generated from CASE I **(top-left)** and CASE II **(top-right)**; the tRMS method applied to data generated from CASE I **(bottom-left)** and CASE II **(bottom-right)**. Broken white lines indicate the blob size as a factor of the ion Larmor radius ρ_i. Each phase value for parameter pair blob size and temperature is generated by a Gaussian profile, solved for ϕ for cases I and II, then the floating potential ϕ_f is computed from which $\vec{E} \times \vec{B}$ velocity is computed and the Peak or tRMS method used on this density (amplitude irrelevant) and velocity profile to find the displayed phase differences.

Before applying the peak detection phase technique to MAST data sets, there are likely sources of error that must be understood. Firstly, there will be quantisation error in the peak separation of order $1/f_s$ where f_s is the sampling frequency. Errors in the peak width are estimated by comparing the difference between second and fourth order finite difference computations of equation (4.7). Finally, there is an error associated with the angle of attack that the filament makes in the radial-polodial plane on the probe. Assuming peak locations in the y direction separated by some positive value and peak locations in the x direction are coincident, and defining the angle of attack as $\xi = \sin^{-1}(v_p/v_r)$ so that no polodial detection can be made at all for $\xi = 0$, the fractional error in the peak separation will be

$$\epsilon_{atk} = \frac{\sqrt{1 + v_p^2/v_r^2}}{v_p/v_r} - 1, \tag{4.11}$$

where v_p is the polodial velocity, and v_r is the radial velocity

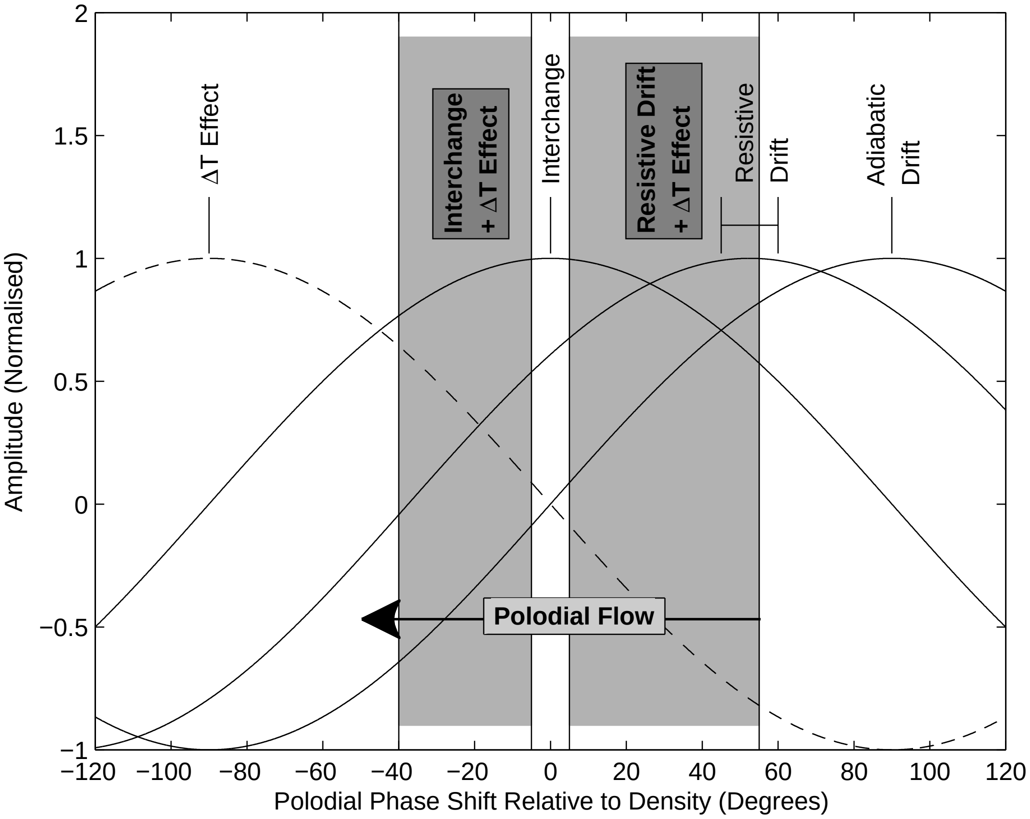

Figure 4.3: Diagram of the direction of the phase shifts of drift and interchange velocity peaks due to temperature gradient effects, and the direction of the polodial flow, so that interchange peaks would be detected earlier than the density peaks, and drift peaks later than the density peaks. ”Drift” and ”interchange” peak means the location of the velocity peak relative to the density for each mechanism. The reason for this ordering is that the plasma rotates in the ion diamagnetic direction [Ayed et al., 2009], typically with greater velocity than the blob advection.

4.3 Results and Discussion

Data is taken from the Gundestrup [MacLatchy et al., 1992] and mach probe heads (discharges 21712 and 23768) that have been installed on MAST, from which downstream (first contact with the plasma flow) measurements are selected by choosing appropriately located probe outputs on the probe head; this minimises the the flow disruptions due to the presence of the probe.

Beginning with the thresholded RMS method, we take data sets for density and apparent velocity and window into sections of length comparable to the estimated upper bound for filament temporal width ($4 \times 10^{-4}s$), then for each section calculate the RMS phase for velocity a number of velocity thresholds. Figure (4.4) shows us that with increasing velocity threshold, the apparent phase angle descends toward zero. This may be theoretically expected in the interchange case since the radial velocity profiles shown in figure 4.1 become increasingly coherent as data below an increasing velocity threshold is excluded. At a threshold of zero, we find qualitative agreement with the predicted phase shift due to the interchange in figure 4.2 which was estimated also at a threshold of zero.

The results of the peak detection method are shown in figure 4.6 and (4.7), in the form of the distribution of the detected phase differences. For SOL measurements in the 21712 we find a shift of the phase pdf toward values of -20 to -40 degrees, in agreement with predictions. The sign negative of the angle shift, which means that velocity peaks are being detected before density peaks is in agreement with interchange velocity peaking shown in figure 4.3. However the SOL measurements in the dataset 23768 give a a strongly peaked value at zero degrees, appearing to be indicative of a measurement of interchange activity not corrupted by temperature gradients when using the floating potential. We expect the range to find a phase shift due to drift wave transport to be approximately 5 to 55 degrees; taking into account first the shift from the adiabatic case to the resistive case due to finite parallel resistivity, and then the shift due to the temperature gradient effects. However for both SOL data-sets, we do not find significant probability of phase in this range compared to the range ~ 0 to -40; the phase distributions in the SOL agree with predictions made by electrostatic interchange models, and disagree with predictions characteristic of drift-wave models.

A numerical study of the action of drift waves on SOL filaments [Angus et al., 2012] reports that there is a timescale, dependent on the filament size, after which a filament propagating under the interchange will be destroyed by drift-wave instabilities that grow in the strong gradient region in the filament edge; this timescale may be also overestimated since the filaments begin with no parallel gradients. Typically, this timescale is $2.5 \times 10^{-5}s$ for the simulated plasmas, and a filament size of $\delta = 0.1m$, although it should also be noted that the parameters result in filaments with a higher drift-instability growth rate as noted by the reporters; the rate in normalised units is $\gamma_{dw} = \sqrt{\frac{R_c}{\delta}}$ where R_c is the radius of curvature, taking a value of $150cm$ as opposed to the $85cm$ found on MAST, and δ is the filament perpendicular size. For a typical MAST filament velocity of $1kms^{-1}$, the time to propagate through our region of measurement, $\sim 0.06m$ in length, from the LCFS is then $6 \times 10^{-5}s$, approximately twice as long as the reported destabilisation time – however γ_{dw} is approximately ten times slower in going from the simulated $R_c = 150cm$ to the $R_c = 85cm$ appropriate for MAST.

We additionally compare displacements of negative velocity peaks, since an interesting behaviour is found in the 23768 data; there is a drop in the probability near zero phase, and local maxima further from zero in both directions shown in figure 4.8, reminiscent of the negative peaks seen in the limiting cases displayed in figure (4.1) for case II, however these trends are either not resolved well or not found in the 21712 data. This is further evidence for interchange driven blob propagation in these datasets.

In the 21712 data-set the reciprocation range puts the probe inside the plasma at $\sim 2cm$ for $\sim 0.05s$, repeating the measurement in this range we find the distribution function peaked very close to zero at $\sim 1.2°$, with little breading compared to the SOL measurements – this is expected due to the smaller temperature gradients associated with filaments found inside the LCFS. Interpreting this phase distribution to be mostly unaltered by temperature gradient effects, we find that the electrostatic interchange is dominating the transport of filaments inside the LCFS, given the absence of any strong distribution of phase in the $5 - 55°$ region. Using the linear prediction of phase difference between density and potential in the drift-interchange system of [Dewhurst et al., 2009],

$$\theta = tan^{-1}\left(-\frac{1}{B}\frac{dB}{dR}\frac{2\pi}{\lambda_y}\frac{1}{\alpha}\right), \tag{4.12}$$

where the radial coordinate R, λ_y is the transverse wavelength in the spectral analysis, B is the magnetic field and α the adiabatically parameter that includes the effects of parallel resistivity. Length scales are normalised to the hybrid Larmor radius, and taking typical MAST parameters of $\frac{1}{B}\frac{dB}{dR} \sim 1m^{-1}$ and the measured phase difference of $\sim 90°$ we find

$$\alpha \sim \frac{0.007}{\lambda_y}. \tag{4.13}$$

This may be interpreted in one of two ways: Firstly, given reasonable λ_y of > 1, we find the adiabaticity parameter is very low, much smaller than the value in the literature [Horton, 1999], so that here interchange is producing the low θ_{nv} measurement because the drift wave dynamics are very slow in comparison, which may be due to small parallel gradients, strong parallel resistivity or any other deduction that can be made from the quantities in this parameter, or secondly, that this prediction is simply failing in a strongly nonlinear regime in which the interchange becomes the dominant potential producing process. It is possible for the drift interchange system to be unstable to drift waves on some small scales, which couple via inverse cascade to large enough scales for the interchange to destabilise [Angus et al., 2012]; the system may exhibit characteristics typical to the interchange on observed scales while ultimately relying on the drift wave instability to drive the cascade at smaller scales and it would be incorrect to draw the conclusion that drift waves do not play a role in this case.

4.4 Summary

We have shown that for tailored measurements of phase, signatures of electrostatic interchange dynamics, modified by the application of floating potential measurements can be found that are rarely discussed in the literature. These are, the zero phase of plasma density and velocity when using peak separations as an approximate for phase, and the negative velocity lobes either side of the density peak; it estimated from recent numerical work that the SOL drift wave instability may be acting too slowly to be detected in the radial coverage region of the probe. Measuring $2cm$ inside the plasma, the phase measurements are still characteristic of an electrostatic interchange, and as expected effects due to temperature gradients are much less visible; this suggests that the electrostatic interchange continues to be responsible for the propagation of positive density fluctuations away from the plasma in this region.

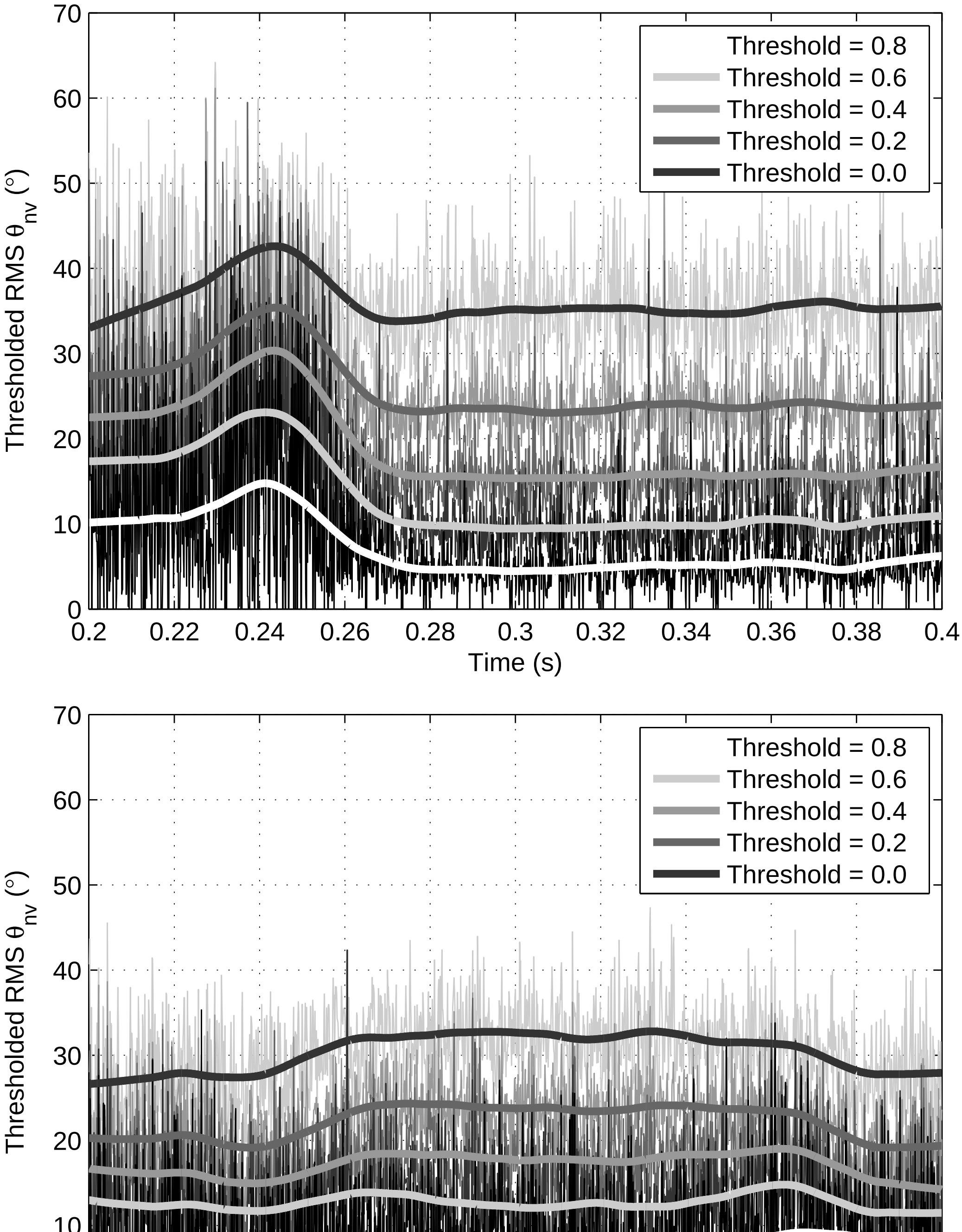

Figure 4.4: Traces of windowed tRMS evaluations of θ_{nv} for both datasets (top:#21721, bottom:#23768), with incremental changes to the chosen threshold where -1 represents a threshold at the minimum velocity of the dataset, 0 a threshold of zero velocity and 1 a threshold at the maximum of the dataset (i.e, a threshold of 1 excludes all data, and a threshold of 1 includes all data). For a reference of probe location with respect to time, see figure 4.5.

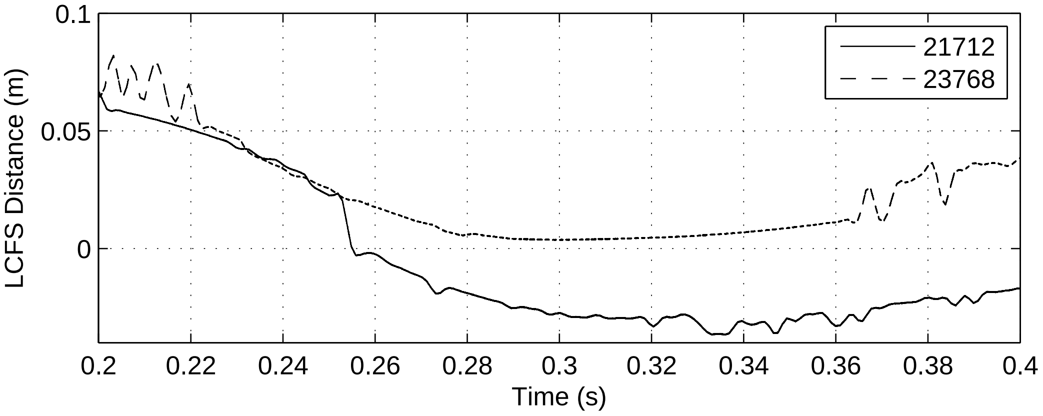

Figure 4.5: The location of the reciprocating probe with respect to time for discharges #21712 and #23768.

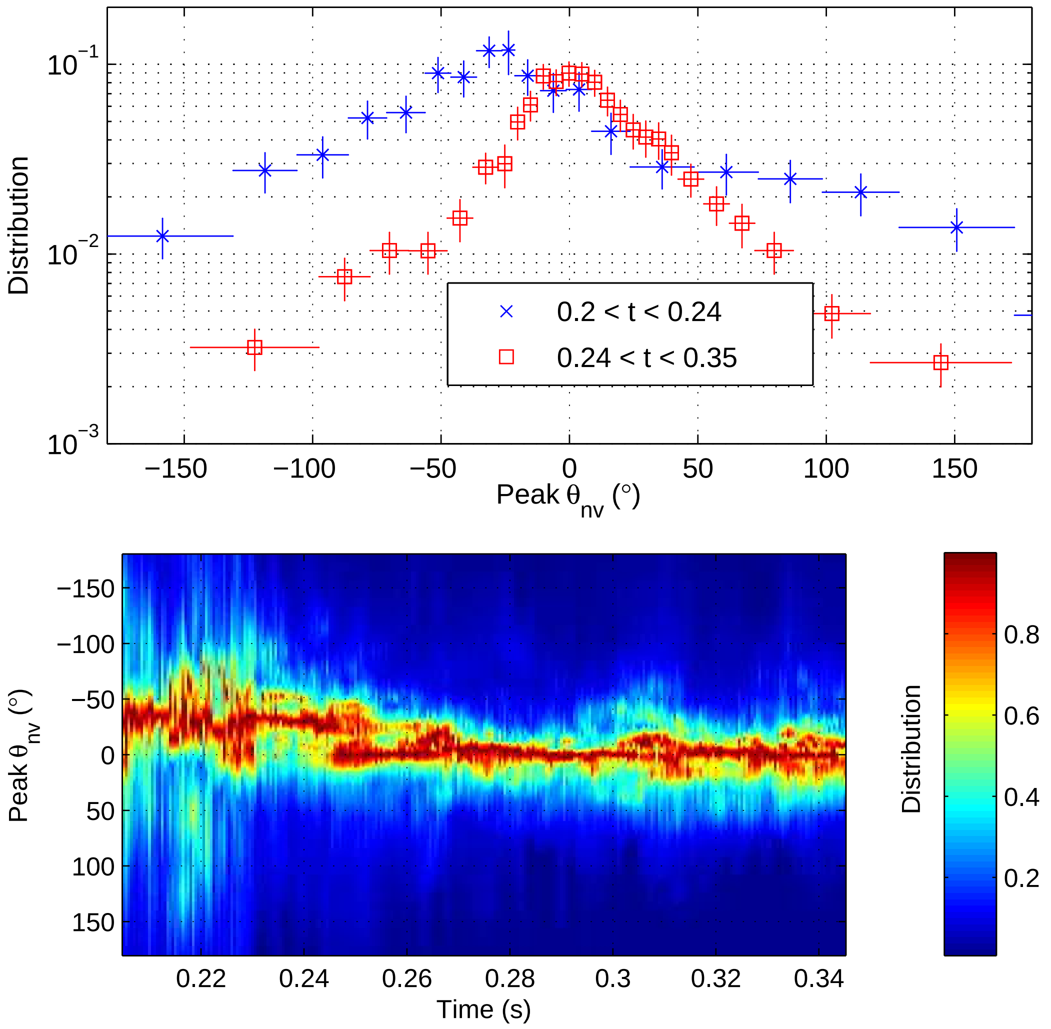

Figure 4.6: **(top)** Distribution of detected phase differences evaluated by the peak method, for a temporal range specified in the legend; discharge #21712. Each point describes the average probability for the range (of θ_{nv}) covered. Bin widths are chosen such that each bin contains 50 data points; fractional error in distribution is estimated as $\frac{1}{\sqrt{N}}$ where N is the bin count, hence fractional errors are uniform. Error in the source data (discussed in section 2) is interpreted by uniformly redistributing each value across the number of bins corresponding to the error. **(bottom)** The same phase difference distribution is unfolded in time, and normalised such that the maximum probability at each temporal location is unity in order to display a relative probability density plot. Distributions are interpolated to regular values of θ_{nv}. At times earlier than $\sim 0.24s$, the probe is outside the LCFS (blue crosses) and at later times the probe is inside the LCFS (red squares). SOL measurements peak at approximately $-25°$ (n lagging v), which may be attributed to blobs with interchange phase difference and a shifted phase due to electron temperature gradients. For times later than $0.24s$, the phase difference peaks approximately between $\pm 10°$, a value that is difficult to attribute to drift wave activity, it is however more readily explained by interchange activity. In the unfolded distribution (bottom), there is a clear transition of the peak phase difference from $\sim -25°$ to $\sim 0°$ in the region $0.24s$ to $0.26s$. For a reference of probe location with respect to time, see figure 4.5.

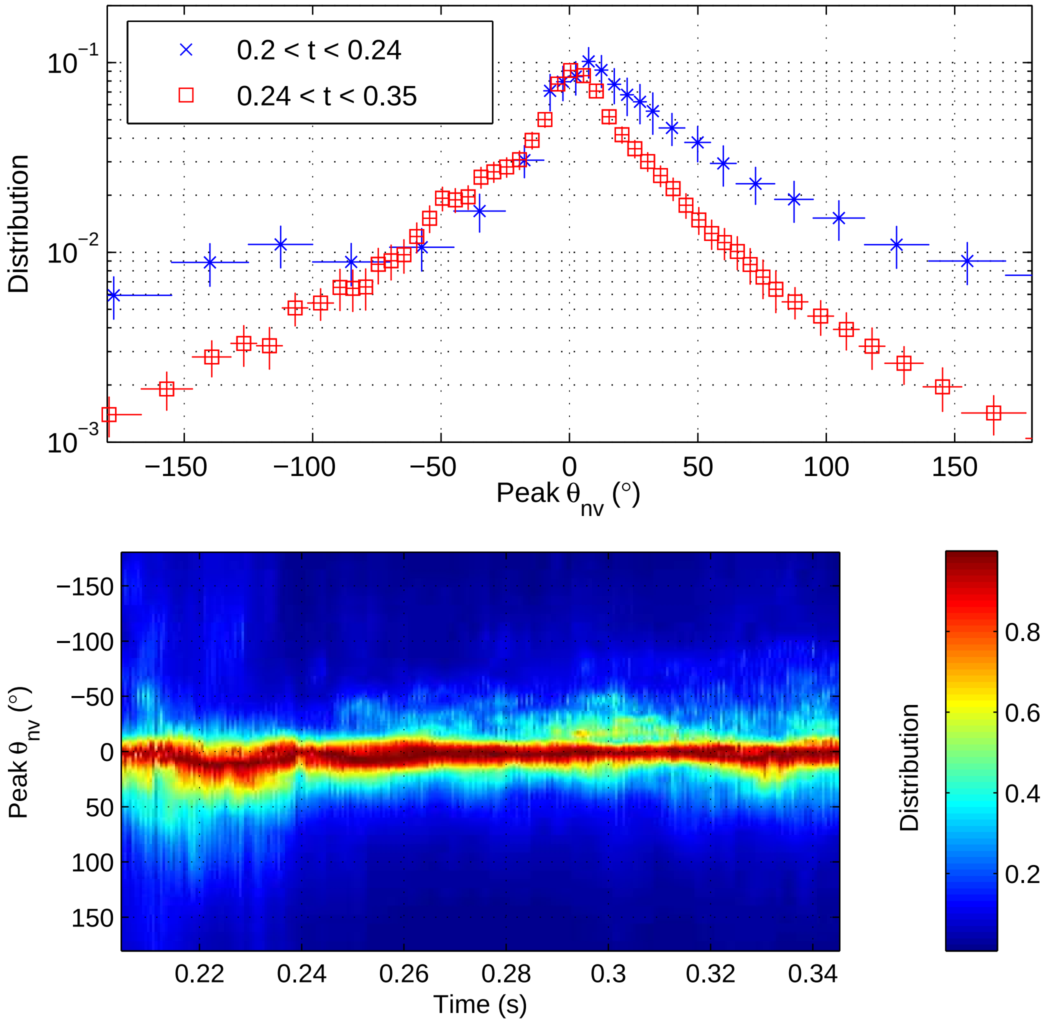

Figure 4.7: **(top)** Distribution of detected phase differences evaluated by the peak method, for a temporal range specified in the legend; discharge #23768. Each point describes the average probability for the range (of θ_{nv}) covered. Bin widths are chosen such that each bin contains 50 data points; fractional error in distribution is estimated as $\frac{1}{\sqrt{N}}$ where N is the bin count, hence fractional errors are uniform. Error in the source data (discussed in section 2) is interpreted by uniformly redistributing each value across the number of bins corresponding to the error. **(bottom)** The same phase difference distribution is unfolded in time, and normalised such that the maximum probability at each temporal location is unity in order to display a relative probability density plot. Distributions are interpolated to regular values of θ_{nv}. In the phase distribution plots (top), the data is split into two sections we will call the near and far SOL, where the probe is in the far SOL at early times, and the near SOL at later times. For both regions, this dataset clearly shows a phase difference that peaks at 0°, which is strongly indicative of interchange activity where the measurements are relatively unaffected by electron temperature gradient effects. There is very little variance with radial position of the probe. For a reference of probe location with respect to time, see figure 4.5.

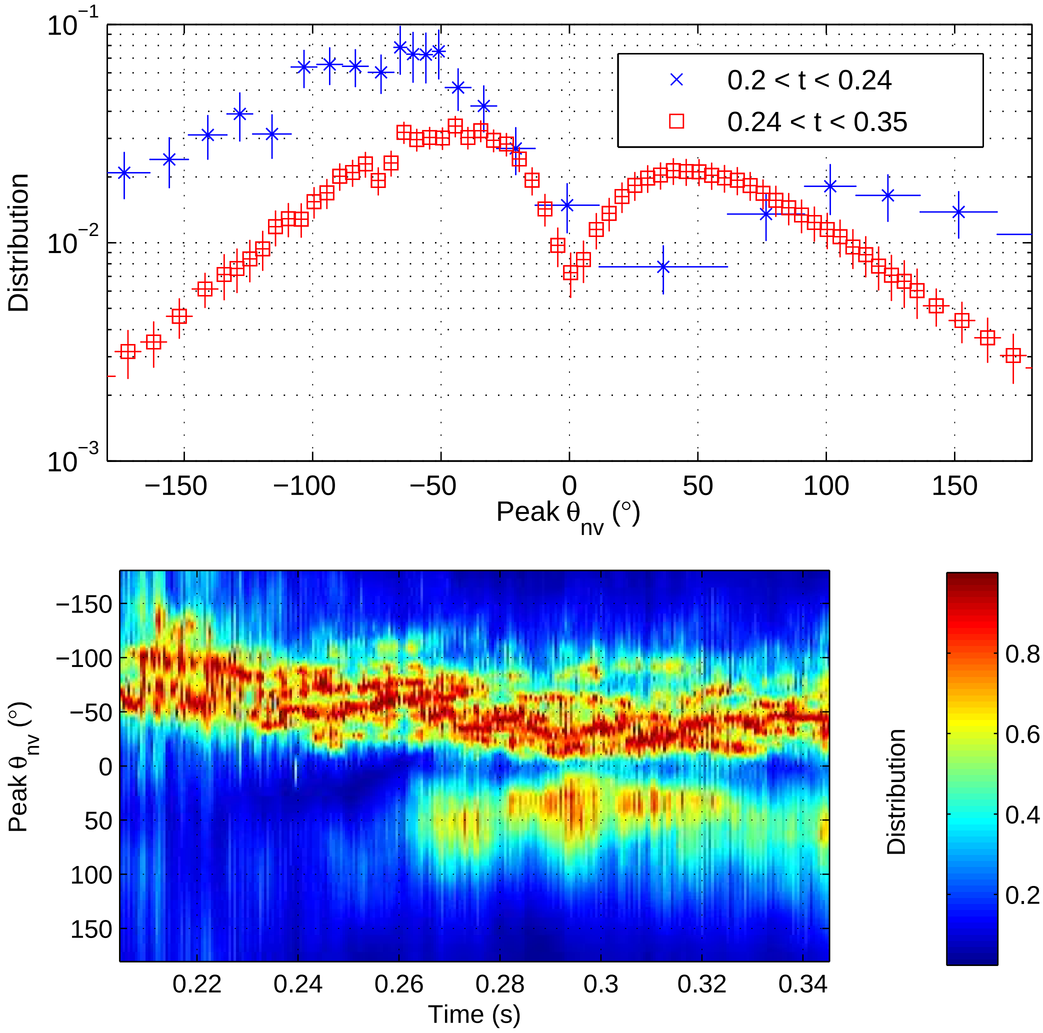

Figure 4.8: **(top)** Distribution of detected phase differences evaluated by the peak method, *for negative (or inwardly moving) velocity peaks*, for a temporal range specified in the legend; discharge #23768. Each point describes the average probability for the range (of θ_{nv}) covered. Bin widths are chosen such that each bin contains 50 data points; fractional error in distribution is estimated as $\frac{1}{\sqrt{N}}$ where N is the bin count, hence fractional errors are uniform. Error in the source data (discussed in section 2) is interpreted by uniformly redistributing each value across the number of bins corresponding to the error. **(bottom)** The same phase difference distribution is unfolded in time, and normalised such that the maximum probability at each temporal location is unity in order to display a relative probability density plot. Distributions are interpolated to regular values of θ_{nv}. Regions are defined in the same was as figure 4.7. We find for the near SOL a double peak structure with maxima at $\sim \pm 50°$; such a structure is very typical of the velocity structure produced by the sheath limited vorticity equation (CASE II), easily visible in the displacement of negative velocity peaks relative to the density peak in figure 4.1. This is further evidence of interchange driven blob dynamics in these datasets. For a reference of probe location with respect to time, see figure 4.5.

Chapter 5

Numerical modelling of scaling behaviour

Some of the results of this section have been published at [Higgins et al., 2012]. In this chapter the feasibility of finding filaments travelling under the mechanism (2.74) in a fully turbulent plasma is tested by numerical evolution of the governing dynamical equations,

$$\begin{aligned} \left(\frac{\partial}{\partial t} - D\nabla_{\perp}^{2}\right) n &= [n, \phi] - \sigma e^{-\phi} + S && (5.1) \\ \left(\frac{\partial}{\partial t} - \nu\nabla_{\perp}^{2}\right) \nabla_{\perp}^{2}\phi &= \left[\nabla_{\perp}^{2}\phi, \phi\right] + \frac{\sigma}{n}\left(1 - e^{-\phi}\right) - \frac{g}{n}\frac{\partial n}{\partial y}, && (5.2) \end{aligned}$$

which are the equations leading to the result (2.74) including dissipation and a source of particle density, where the aim is to test the velocity scaling without the assumption of a constant vorticity and zero dissipation.

Equation (5.1) describes the evolution of the plasma density n. The second term on the LHS of (5.1) describes the change in density due to collisional diffusion and provides a dissipation scale for turbulent density structures. The first term on the RHS of (5.1) gives the advection of plasma density with the $\vec{E} \times \vec{B}$ drift, while the third term is a density sink due to parallel plasma transport and the fourth a density source due to transport across the LCFS into the simulation domain.

Equation (5.2) describes the evolution of plasma ($\vec{E} \times \vec{B}$) vorticity $\nabla_{\perp}^{2}\phi$. The second term on the LHS of (5.2) describes the change in vorticity due to collisional viscosity and provides a dissipation scale for turbulent vorticity structures. The first term on the RHS of (5.2) gives the nonlinear advection of plasma vorticity with the $\vec{E} \times \vec{B}$ drift, the second term on the RHS of (5.2) is the change in plasma vorticity due to the parallel electron and ion sheath currents and the final term is the current arising from the electron diamagnetic drift, containing gradients of the magnetic field which provides the interchange drive due to curvature and gradient B currents, destabilising regions with $\partial_y n$.

The diffusion and viscosity coefficients D, ν, and the source term S must be estimated. The parallel sheath resistivity is $\sigma = \rho_i / L_\parallel$, and the magnetic field curvature by $g = \rho_i / R_0$ where R_0 is the tokamak major radius.

Spatial dimensions are normalised to the ion Larmor radius ρ_i, temporal dimensions to the ion cyclotron frequency ω_{ci}, potential is normalised to the thermodynamic potential T_e/e and density to the target density n_t.

In this model we have allowed the density of the filament to vary with respect to the target density n_t, however the parallel model [Riemann, 1991] used insists at the very least that there is an exponentially decreasing density profile in the parallel direction toward the sheath. We therefore restrict the simulated values of normalised density n to be greater or equal to unity, ensuring the parallel model remains approximately consistent. This is achieved by altering the form of the sheath dissipation in the continuity equation for $1 < n < 2$ by multiplication with $(n - 1)$, allowing a smooth transition to $n = 1$ in this region. While this is an arbitrary choice, we note that it has no effect on the large fluctuations associated with filaments.

5.1 Numerical Implementation

Equations (5.1) and (5.2) are evaluated by second order centred finite differencing on a grid with $NX \times NY$ points using the classical 4th order Runge-Kutta scheme to integrate the initial values of n and ϕ in time [Press, 1992]. The Laplace boundary problem of finding ϕ at the new timestep from $\nabla_\perp^2 \phi$ given by equation ((5.2)) is integrated spectrally using the eigenvalues of the Laplace operator and FFTW [Frigo and Johnson, 2005]. Boundary conditions for all simulated quantities are periodic, with a damping region at a given radial distance and range from the source of the interchange flux. Initial conditions are

$$\phi = 0; \quad n = \sum_i^{NY} S_0 + \frac{S_0}{100} \sin\left(k_i y + \varphi\right) \tag{5.3}$$

in order to destabilise the plasma as quickly and with as little spectral bias as possible, with the random phase $0 < \varphi < 2\pi$ (uni-formally distributed).

Convergence for performed simulations is reached at a timestep of $0.2/\omega_c i$

and a resolution of 1024×1024 grid points. Total simulation time is typically 5×10^4 timesteps. The code is parallelised in the polodial direction using MPI [MPI Forum] (Message Passing Interface) also using the parallel FFTW3.3 alpha MPI [Frigo and Johnson, 2005] implementation and run typically on 16 or 32 processes (with a speedup from 1 process of 13 and 21 respectively).

5.2 Parameter Estimation

The source term is modelled as

$$S = S_0 \exp\left(\frac{-(x - 0.5l_x)^2}{2S_w^2}\right), \tag{5.4}$$

where S_0 is the amplitude of the source, S_w is the width of the source and l_x, l_y are the radial and polodial extents of the simulation domain, respectively.

The radii explored by the probe in figure 3.13 corresponds to a radius of $1.48m$ to $1.445m$. Mean values of quantities for this region are given in table (5.1).

Parameter	Value	Parameter	Value
$\lvert T_e \rvert$	$20eV$	$\lvert n_{sol} \rvert$	$1 \times 10^{19} m^{-3}$
$\lvert n_t \rvert$	$1 \times 10^{17} m^{-3}$	$\lvert B \rvert$	$0.3T$
$\lvert l_{\parallel} \rvert$	$15.0m$	$\lvert q \rvert$	4
R_0	$0.85m$	S_w	$3\rho_i$
l_x	$120\rho_i$	l_y	$120\rho_i$
H	$4.4m$	$\lvert \theta_p \rvert$	27°

Table 5.1: Averages of particular values and other parameters used in the TOKER simulation. q is the safety factor, $|n_{sol}|$ is the average SOL density, H is the height of the MAST vacuum vessel, and $|\theta_p|$ is the average magnetic field pitch angle.

In order to estimate the source strength S_0 we estimate the rate of particles crossing an area of simulated LCFS at the classical Bohm rate [Helander and Sigmar, 2002] which we then set equal to equation (5.4) integrated over the simulation domain. This gives a normalised source strength of

$$\bar{S}_0 = \left(\frac{(\partial_x n_{ped})\, T_{ped}}{16eB_{ped}\sqrt{2\pi}S_w}\right)\left(\frac{1}{\omega_{ci} n_t}\right), \tag{5.5}$$

where the subscripts $_{ped}$ denote pedestal vales, which for the discharges analysed in section 3.2 are $\partial_x n_{ped} \approx 10^{20}$, $T_{ped} \approx 100eV$ and $B_{ped} \approx 0.35T$. From equation (5.5) we find a value of $S_0 = 5.5 \times 10^{-3}$ to $S_0 = 1.1 \times 10^{-2}$ gives rough agreement between TOKER and estimated MAST particle flux across the LCFS, given a range of $1 \times 10^{18} m^{-3} > n_t > 5 \times 10^{17} m^{-3}$.

Diffusion and viscosity coefficients are estimated from collision rates and the Pfirsch-Schlter neoclassical collisional transport regime as described in [Helander and Sigmar, 2002; Fundamenski et al., 2007], where we use the electron temperature as an effective ion temperature in determining the viscosity coefficient. This results in $D \approx 1.7 \times 10^{-3}, \nu \approx 2.4 \times 10^{-3}$.

5.3 Numerical Results

We have performed 7 simulations to span the possible values suggested for n_t. These simulations designated $TOKER01$ to $TOKER07$ have source strengths of $(15, 9, 10, 6, 5, 3, 18) \times 10^{-3}$ respectively.

We use the same technique described in section 3.2 of chapter 3 to evaluate the α scaling parameter with these exceptions:

1. Signal pre-processing of the simulation data is not required since the model does not produce a radial trend in potential, has direct measurement of plasma potential and radial positions are known precisely.

2. Time series of quantities are taken once the simulation has reached a quasi-stationary state after initial destabilisation of the plasma between times $0.5ms$ to $1.7ms$ for a selection of radial and polodial locations. Peak averages are taken from this entire range at each of these selected locations, and the average at a given radial position includes all peak detections for each polodial location of that radial position.

3. Electric field is measured on two scales given by the scale that the Gundestrup probe on MAST measures the polodial electric field, and the smallest scale electric field corresponding to $23.9mm$ and $3.0mm$ respectively. This is to assess the impact that measuring E_θ on a particular scale has. Results for the α scaling parameter are given using these two scale lengths.

Figure (5.1) shows a snapshot of simulation TOKER01 at a time $t = 0.7ms$. Notably there is a high degree of mixing in density while the plasma potential retains mainly large scale features; plasma filaments appear to have a complex internal transport with strongly varying densities, with an overarching radial transport of this structure. In figure 5.2 we see the elongated radial velocity bursts set up by the plasma vorticity model, characteristic of this type of SOL model.

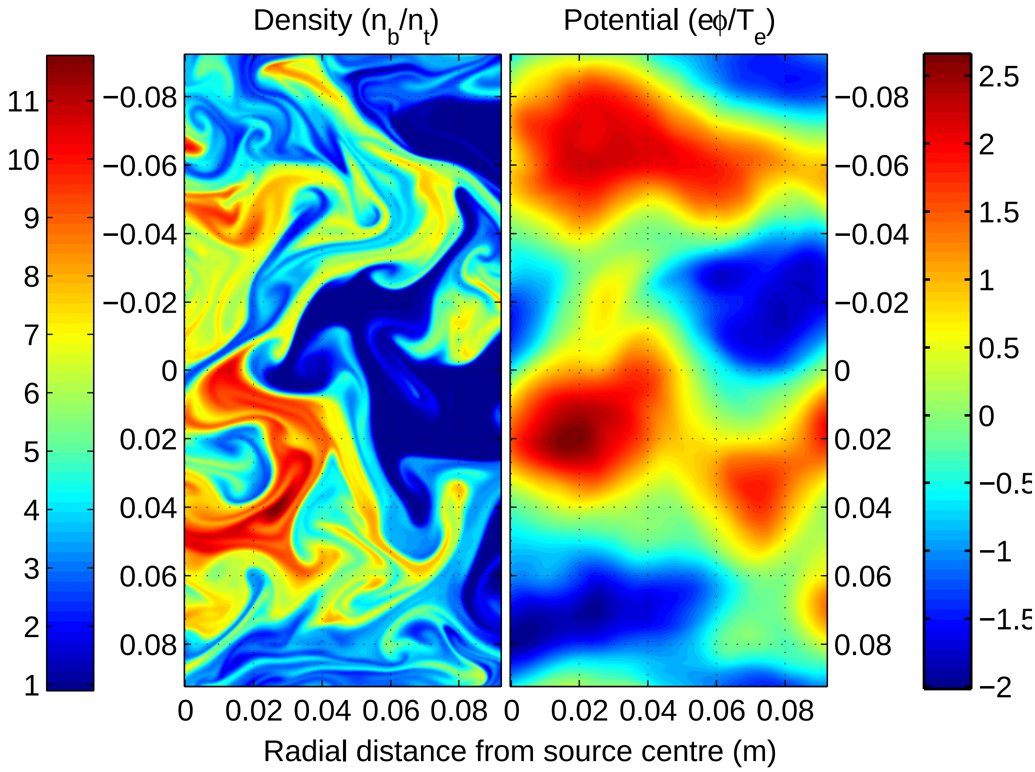

Figure 5.1: (left) Density and (right) potential snapshots of simulation TOKER01 at time $t = 0.7ms$. The scale of the potential fluctuations is much greater than that of the density fluctuations - these “filaments” have a large degree of internal structure, with an overarching general drift.

The strength of density fluctuations is given for the simulated plasmas in figure 5.3, and it appears that for the lower source strength simulations the scaling (2.71) could play a role. It should be noted however that this measure of fluctuation strength gives an average picture, and also is a conservative estimate. An alternative measure of average fluctuation strength might be to take n_t as the background n_0, in which case simulated plasmas would have a fluctuation strength always ≥ 1. Complications and correct interpretation of this measurement are given in figure 3.10.

The simulation domain is relatively small compared to the entire MAST SOL, we only simulate a domain large enough to be comparable to the probe reciprocation distance in section 3.2. Due to the sheath dissipation (second term in equation (5.1)) not being proportional to plasma density in this model, it cannot contribute to an exponential SOL density profile and we may expect that SOL widths are

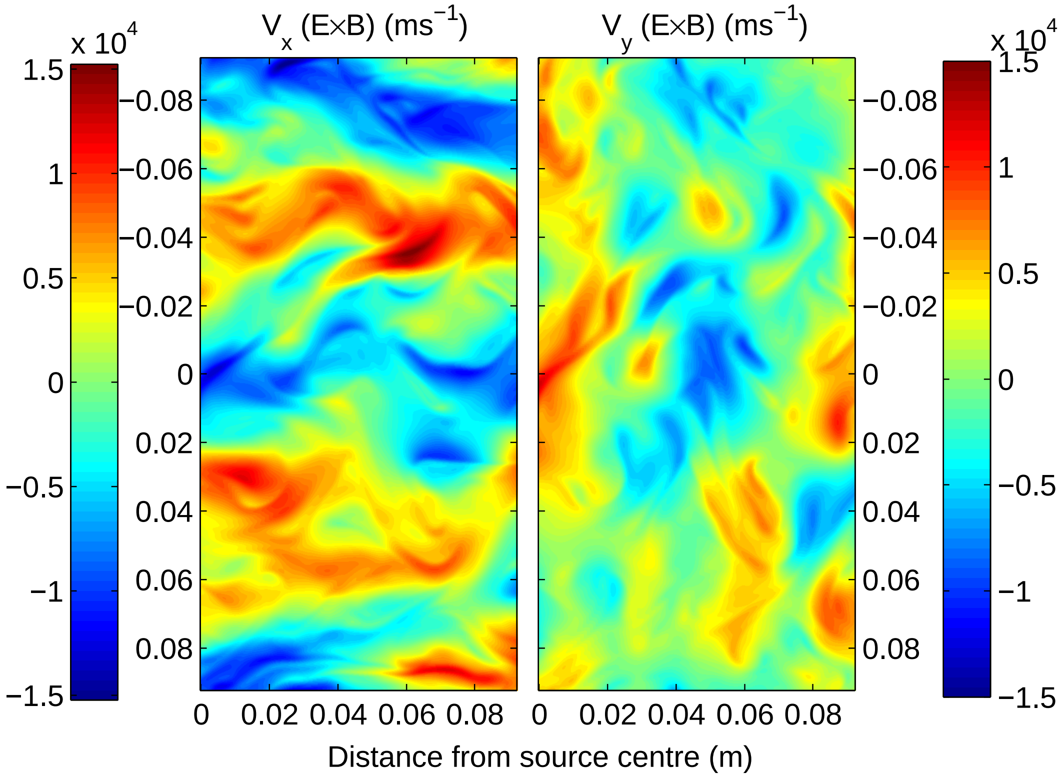

Figure 5.2: (left) Radial and (right) Vertical $\vec{E} \times \vec{B}$ drift velocities for simulation TOKER01.

not reproduced self consistently in this model. In figure 5.4 the averaged density profile does exhibit an exponential profile, while the density peak averages in figure 5.5 have a linear profile. The profile in (5.4) may be due to the nature of sheath dissipation near to $n_b/n_t \approx 1$ which as discussed is modified toward $(n_b - 1)\,\sigma e^{-\phi}$ near this limit. In addition, the $n_t \approx const$ model becomes questionable in this region (since n_t should be allowed to vary as this limit is approached), so that we limit our discussion to filaments with high n_b/n_t where the $n_t = const$ assumption is most valid.

Figures (5.6) and (5.7) give the averaged peak detections of radial $\vec{E} \times \vec{B}$ velocity for simulated plasmas, at smallest and probe scales respectively. The small scale velocities are consistently larger than the probe scale velocities by $200ms^{-1}$ to $400ms^{-1}$, indicating that the “internal structure” of the filament is mildly moving ahead of the “surrounding filament” (it becomes difficult to define the plasma filament with this degree of mixing). The dominant structures appear to be streamer like with $k_x = 0$. It is important to remember that the error bars correspond to

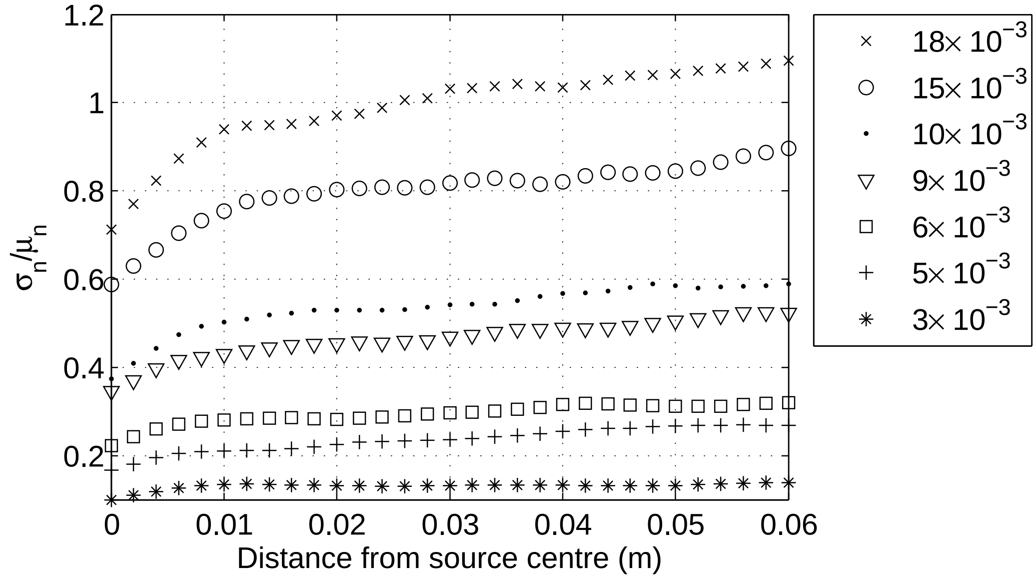

Figure 5.3: The strength of density fluctuations relative to ambient density for TOKER data (each with different source strength S_0, indicated in the legend), where σ_n and μ_n are the standard deviation and mean of n respectively.

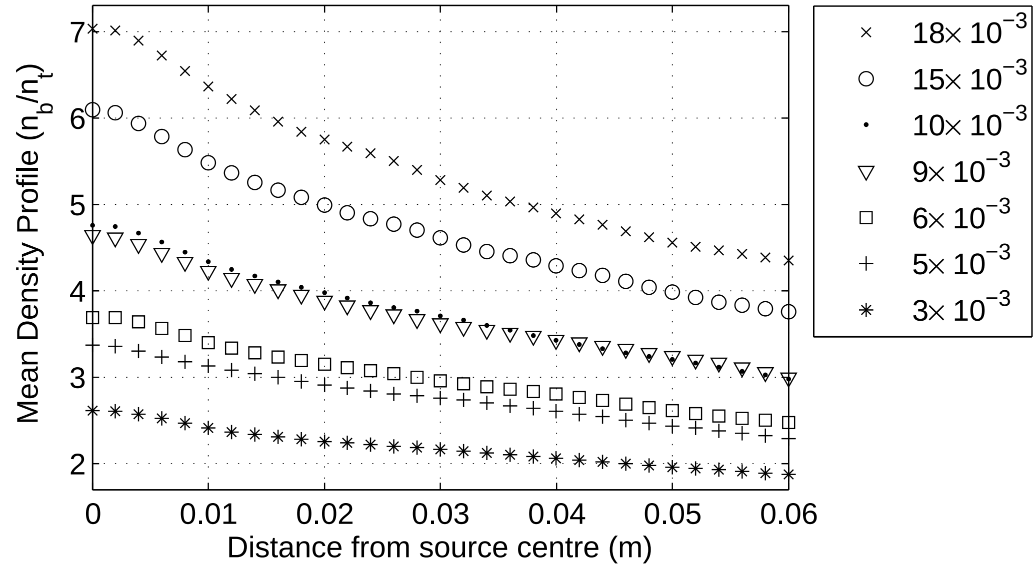

Figure 5.4: Averaged radial density profiles for simulated plasmas (each with different source strength S_0, indicated in the legend).

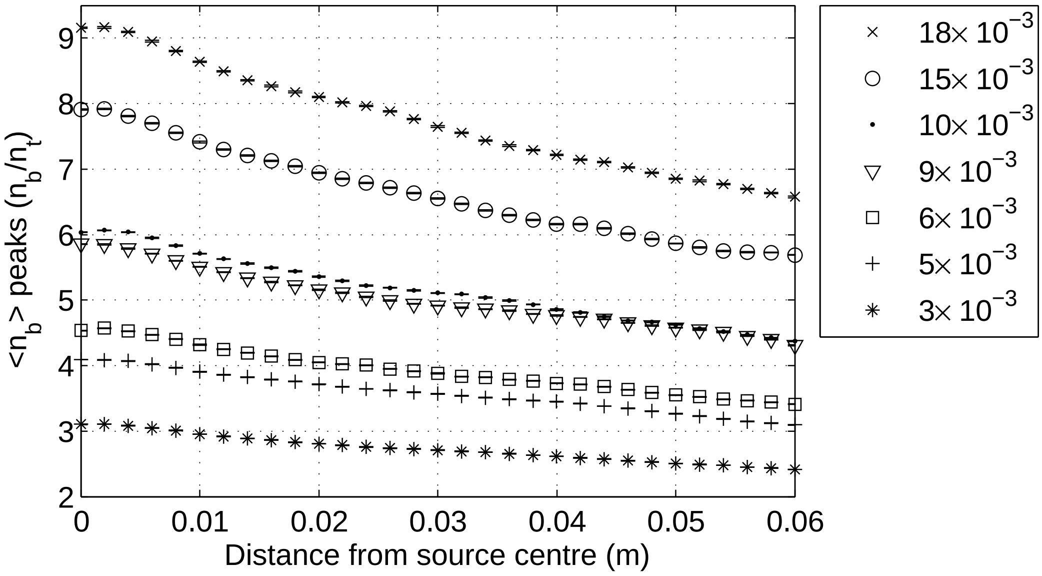

Figure 5.5: Average peak density radial profile for simulated plasmas (each with different source strength S_0, indicated in the legend).

the confidence on the mean, not simply the variance of the measurement which is of course much larger. Early (small radii) $< v_E >$ peak profiles appear to correspond to an acceleration phase where the plasma potential grows to the limits governed by plasma vorticity and parallel currents, and since the parallel currents are inversely proportional to n_b in our model this saturation limit occurs at larger radii for discharges with higher S_0.

Figure (5.8) gives the α scaling parameter for selected comparisons of the simulated plasmas. In terms of the two selected E_θ scales, α does not vary significantly in general (this makes sense, since we would expect the same scaling in n_b for a given scale). It should also be noted that an inverse scaling of v_E with $l_\perp$ is consistent with sheath models.

Considering that saturation of v_E is reached at greater radii for higher S_0 simulations, we see in figure 5.8(e) a sheath scaling at $r \approx 0.3m$, in (5.8)(d) (higher S_0) at $r \approx 0.41$ and in (5.8)(c) (higher S_0 again) at $r \approx 0.52$. For these comparisons the balance of perpendicular currents is clearly resulting in an eventual sheath scaling. In figures (5.8)(a,b), we can see that the sheath currents are becoming more limited by the high density filaments (see equation (5.2)), pulling scalings down from unity toward zero. Finally figure 5.8(f) (which perhaps has a small fluctuation strength) shows the biggest difference in α between E_θ measurement scales of

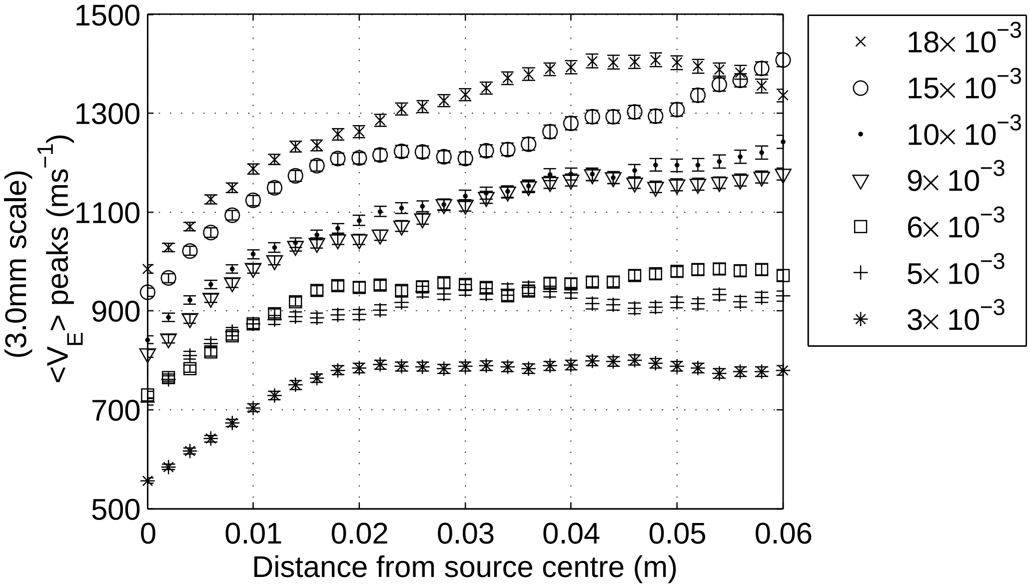

Figure 5.6: Average peak radial v_E radial profile for simulated plasmas ($3.0mm$ scale) (each with different source strength S_0, indicated in the legend).

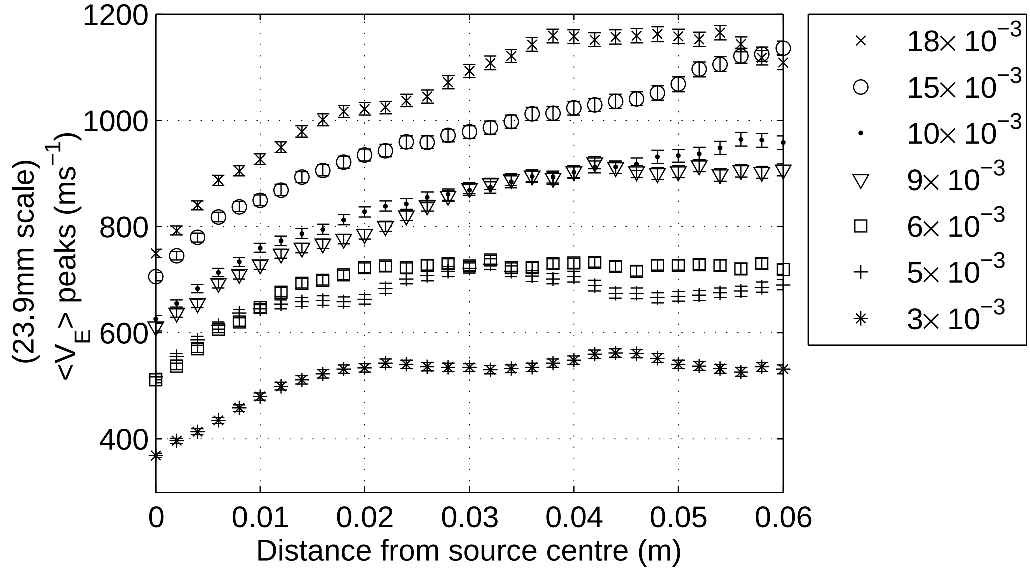

Figure 5.7: Average peak radial v_E radial profile for simulated plasmas ($24.9mm$ scale) (each with different source strength S_0, indicated in the legend).

around 0.4 and is the most difficult to interpret. The small scale α result in figure 5.8f may indicate the presence of the scaling in equation (2.71) when combined with figure 5.3, however since these fluctuation strength measurements are conservative it is the authors opinion that this is another mode of competition between the scalings in equations (2.72) and (2.74).

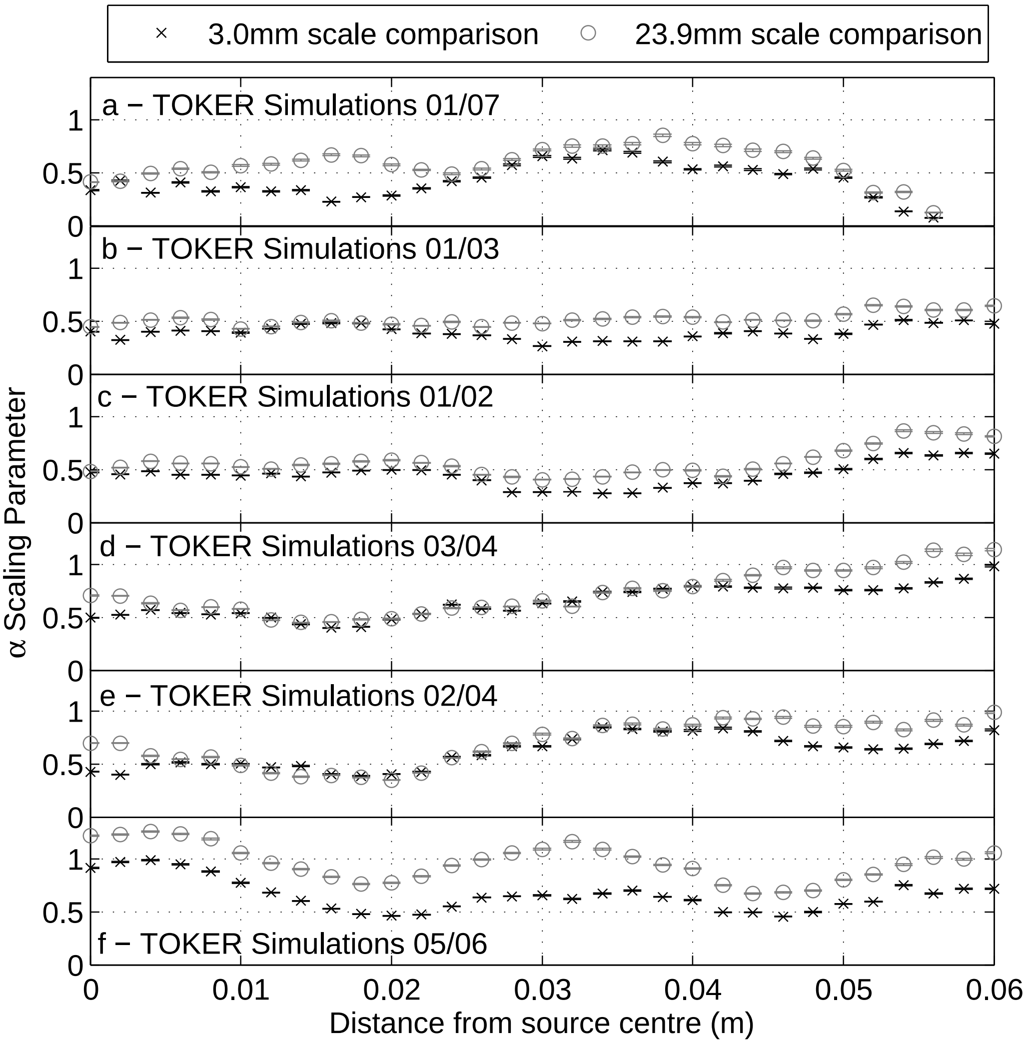

Figure 5.8: The α scaling parameters for selected comparisons of TOKER simulations at different source strengths. Results indicate a competition between (2.74) at $\alpha = 1$, interchange balanced by sheath current at constant target density, and (2.72) at $\alpha = 0$, interchange balanced by advection of vorticity. The TOKER model cannot scale with (2.64). A scaling of (2.71) is also unlikely due to the high strength of density fluctuations (see figure 5.3). Given the strength of nonlinearity, we may expect an α in the range of ~ 0.35 to ~ 0.22, referring to figure 3.10 and 5.3 for a blob advection with interchange balanced by advection of vorticity, as opposed to the extreme given by 2.72 of $\alpha = 0$.

We suggest that the reason we do not find $\alpha \approx 1$ until larger radii in figure 5.8 is due to an unrealistic LCFS source treatment; in reality it is a source of flux not just density. This means that in the simulation we have to wait until these filaments pick up their saturated velocities (if a stationary saturation is indeed ever reached), a more complete treatment may be to include an edge plasma and boundary region as in ESEL [Garcia, 2009].

5.4 Summary

These investigations demonstrate that in general, it is possible to find filaments with a high scaling index as found experimentally in figure 3.13, however, in the transition from the laminar model of (2.74) to the investigation of the dynamics in the turbulent scenario, with driving and damping terms, the alpha index is far from stationary, and in all cases the scaling 2.74 is in competition with the nonlinear advection of vorticity which drives a scaling as discussed in figure 3.10.

Chapter 6

Numerical modelling of warm SOL effects

In this chapter we adopt the governing equations of 6.1 to study the plasma in the presence of warm electrons and ions with an effective parallel temperature at the sheath boundary. The shapes of the density, velocity, flux and phase PDFs are analysed in each case, and, the difference in the velocity,flux and phase pdfs is given when probes measure floating potential as opposed to the real plasma potential. Consequences of the boundary conditions for blob evolution are evaluated. We begin, first, with the numerical implementation of the model equations which were derived in chapter 2,

$$\begin{aligned}
\partial_t n &= \frac{1}{B}\left[n,\phi\right] - \frac{n}{B^2}\left[B,\phi\right] - \frac{n_t}{l_\parallel}\sqrt{T+3T_t} + R_n + S_n, && (6.1)\\
\partial_t \nabla_\perp^2\phi &= \frac{1}{n}\left[p,B\right] + \frac{1}{B}\left[\nabla_\perp^2\phi,\phi\right] + \frac{B^2}{n}\frac{n_t}{l_\parallel}\sqrt{T+3T_t}\left(1.0-\exp\left(F_\Lambda-\frac{e\phi}{T}\right)\right) \\
&+ \frac{1}{nB}\left(\left[\nabla_\perp^2\phi, nT\right] + \left[\vec{\nabla}_\perp\phi, \vec{\nabla}_\perp(nT)\right]\right) + R_\Omega + S_\Omega, && (6.2)\\
\partial_t T &= \frac{1}{B}\left[T,\phi\right] + \frac{2T}{3B^2}\left[\phi,B\right] - \frac{2T}{3l_\parallel}\sqrt{T+3T_t} + R_T + S_T. && (6.3)
\end{aligned}$$

As usual, the t subscript refers to the target quantity at the sheath entrance to the divertor plates. F_Λ typically takes values in the range $\sim 2.5-3$, depending on the details of the sheath transition modeling. Compared to the TOKER model discussed in chapter 5, the hTOKER model evolves a plasma temperature which typically has gradients of similar magnitude to the plasma density. The term driving the interchange retains the temperature inside the derivative, leading to a stronger force driving the structures and generating vorticity; the SOL modelled by hTOKER typically features even more violent dynamics than the TOKER model. As discussed in chapter 2, ion continuity is followed such that the ion forms for the sheath dissipation of temperature and density are kept, so that when operating with finite ion temperature the system can be evolved with one temperature for both electrons and ions. With finite ion temperature, there are the additional terms 5 and 6 on the RHS of the vorticity equation that provide additional effects on SOL structures.

There are two notable limitations of the parallel model used in hTOKER (2.50). These are, the assumption of $< nv_{\parallel} >=< n >< v_{\parallel} >$, and the neglection of zero parallel wavenumber drift-wave structures which are implied to exist by the scenario which as $\partial_{\parallel} n \neq 0$, as discussed at 2.2.3. Parallel particle flows, heat fluxes and in particular the treatment of warm ion effects without any treatment of the gyro-viscous stresses lead to a severely idealised model as discussed in chapter 2. It is not consistent to treat warm ions without the gyro-viscous stress.

6.1 Numerical Implementation

A summary of the techniques used to evolve the system (6.1) follows,

- Fixed quantities, $L_{\parallel}, n_t, T_t, B$, do not vary with time or the polodial direction, and are set up during the initialisation phase and do not change. These are the parallel length, target density, target temperature and magnetic field, respectively.

- Time evolution is performed with an explicit predictor corrector method using the Adams-Moulton-Bashforth scheme [Press, 1992]. The timestep is a fixed constant value, boundary conditions are periodic.

- The scheme is parallelised in MPI [MPI Forum] for execution on the distributed memory parallel computers, with the domain distributed in the x (radial) direction.

- The boundary value problem of finding $\phi = \nabla^{-2}\Omega$, is solved spectrally with the MPI enabled FFTW 3.3.1 library Frigo and Johnson [2005], and the eigenvalues of the centred second order finite difference method. The undefined constant value of integration, due to the boundary conditions, is selected by assuming that the plasma furthest from the LCFS source is in equilibrium with the Bohm sheath potential.

- Ambient values for N, T are defined, and after each step of evolution, these values are enforced as the smallest values allowed. For the simulations performed in this chapter these ambient limits take the values of $N_{bg} = 10^{17}m^{-3}$ and $T_{bg} = 1eV$.
- Poisson brackets are solved using the method [Arakawa, 1966], which ensures a high order of conservation.

Normalising quantities used in the simulations of this chapter are $B_0 = 1Tesla$, $T_0 = 1eV$ and $N_0 = 10^{19}m^{-3}$.

6.1.1 Blob Source

Plasma LCFS source is modelled by injection of filaments with Gaussian spatial profiles and properties drawn from predefined distribution functions for density, temperature, velocity, size and waiting time per metre. The blobs enter the domain at the LCFS with the Gaussian envelope, $Env(t) = \exp\left(\frac{(t-t_0)^2}{2\tau^2}\right)$, applied to density, temperature and radial velocity. The envelope, $Env(t)$, has a temporal width defined by the time scale $\tau = \ell/v$, where ℓ is the blob size and v is the radial velocity of the blob. The amplitude of the temporal envelope is defined by $\int_t^{t+\Delta t} Env(t)$ at each timestep to ensure that $\sum_{\Delta t} Env(t) = 1$ over the temporal discretisation of the simulation. These blobs are added to a linked list (and to the simulation) when the waiting time expires, and removed from the list when the time passes 9σ from the peak of the temporal envelope. Each timestep, the source terms S_n, S_T, S_Ω are calculated based on the items in the blob list.

The distributions used in the simulation come from MAST probe measurements, using the same techniques as chapters 3 and 4; peak values are used to calculate the distribution functions shown in figure 6.1. Density and temperature are inferred by finding the distribution function of I_{sat}, normalising it so that it has a mean value of unity, then multiplying by the mean values of density or temperature as measured by the Nd:YAG [Walsh et al., 2003] system around the LCFS to get the blob temperature or density distribution. Waiting times are estimated by the distance between peaks in I_{sat}, and, the polodial extent of the probe is used to estimate the waiting time per metre. Preliminary simulations show that the floating potential measurements of particle-energy flux $\Gamma_E = -\frac{nT\partial_y\phi}{B}$ overestimate the real flux by a factor of 2, therefore, a factor of 0.5 is introduced for the blob velocity distribution.

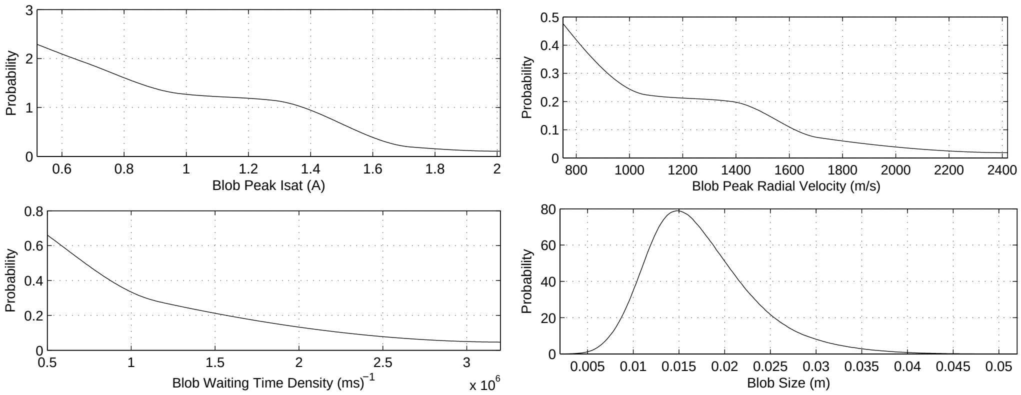

Figure 6.1: Blob distribution functions used in the hTOKER simulations. A factor of 0.5 is applied to the velocity source in light of preliminary simulations showing that the floating potential measurements overestimate the particle-energy flux $\Gamma_E = -\frac{nT\partial_y\phi}{B}$.

Simulations of SOL turbulence including parallel currents associated with sheath boundary conditions are prone to an artificial steady state solution when implemented with steady-state particle density and temperature sources that favours the production of radially elongated streamers. The reason for this may be sought in a steady-state solution solution to linearised interchange equations of motion.

$$\vec{\nabla}\cdot\vec{J} = e\vec{\nabla}\cdot n\left(\vec{v}_p + \vec{v}_{gi} - \vec{v}_{ge} - \vec{v}_{\|e} + \vec{v}_{\|i}\right) = 0 \tag{6.4}$$

gives the quasineutrality condition for the system, with v_p the ion polarisation velocity and $v_{gi,ge}$ the ion and electron drifts due to gravity. Following a linearisation $n = n_0 + \tilde{n}$, we have

$$n_0\vec{\nabla}\cdot\vec{v}_p + n_0\vec{\nabla}\cdot\left(\vec{v}_{\|i} - \vec{v}_{\|e}\right) + \left(\vec{v}_{gi} - \vec{v}_{ge}\right)\partial_y\tilde{n}, \tag{6.5}$$

since n_0 only has a gradient in the $\hat{x}$ direction but $n_0 \gg \tilde{n}$. The electron continuity equation, neglecting the motions due to drifts associated with the gravity is

$$\frac{\partial\tilde{n}}{\partial t} + \vec{v}_E\cdot\vec{\nabla}n_0 + n_0\sigma\frac{e\phi}{T_e} = 0, \tag{6.6}$$

with σ the sheath dissipation rate. After a Fourier transform this becomes

$$\frac{\tilde{n}}{n_0} = \frac{1}{\omega}\left(k_y\frac{\kappa T_e}{eB_0} - \sigma\right)\frac{e\phi}{T_e}, \tag{6.7}$$

in which we can identify the electron drift frequency $\omega_d = k_y v_d = k_y \frac{\kappa T_e}{e B_0}$, with $\kappa = -\frac{1}{n_0}\frac{\partial n_0}{\partial x}$, giving

$$\frac{\tilde{n}}{n_0} = \frac{e\phi}{T_e}\left(\frac{\omega_d - \sigma}{\omega}\right). \tag{6.8}$$

Equation (6.8) may be substituted into the Fourier transform of (6.5) to find

$$k_\perp \vec{v}_p + k_\| \left(\vec{v}_{\|i} - \vec{v}_{\|e}\right) + k_y \left(\vec{v}_{gi} - \vec{v}_{ge}\right) \frac{e\phi}{T_e}\left(\frac{\omega_d - \sigma}{\omega}\right), \tag{6.9}$$

which in the steady-state limit $\omega = 0$ becomes the greatly simplified balance between sheath and diamagnetic rates

$$\omega_d = \sigma. \tag{6.10}$$

This describes the balance between gravity and sheath currents leading to a well defined size of perturbation

$$k_y = \frac{e\sigma B_0}{\kappa T_e} = \left(\rho_i \kappa l_\|\right)^{-1}. \tag{6.11}$$

The problem with a model that has such a well defined unstable mode number, and source terms supplying density and temperature at a constant rate is that a standing wave approximately this wavenumber will form in potential, and the density and temperature will be channelled along these streamlines in the x-direction further reinforcing the standing wave. In the real world, a LCFS will have turbulent fluxes crossing it and in particular, there will certainly be non steady-state sources of plasma potential emanating from processes inside the LCFS. The blob source terms used in hTOKER, which naturally vary in space and in time and provide a source of vorticity, are an attempt not only to realistically model the fluxes across the LCFS but to mitigate this unrealistic steady-state streamer class of behaviour.

6.1.2 Subgrid Model

The natural dissipative scale of the hTOKER system can be very small, smaller than the ion gyro-radius typically is. In the interests of preserving some of the validity of the drift-fluid model, and keeping down the numerical effort, a subgrid dissipation model is employed, based on the model used in [Smith and Hammett, 1997] which pertains to spectral gyro-fluid simulations of drift wave turbulence. Defining the

RMS shear parameter

$$S = \sqrt{\left\langle \left(\frac{\partial v_x}{\partial x}\right)^2 + \left(\frac{\partial v_y}{\partial y}\right)^2 + \frac{1}{2}\left(\frac{\partial v_x}{\partial y} + \frac{\partial v_y}{\partial x}\right)^2 \right\rangle}, \tag{6.12}$$

and the average large-scale wavenumber

$$k_{av} = S \left\langle v_x^2 + v_y^2 \right\rangle^{\frac{-1}{2}} , \tag{6.13}$$

along with a cutoff wavenumber, which we set to the Nyquist limit $k_c = 2/\delta$, the dissipation has spectral eigenvalues of

$$\gamma_h = -M \left[\left(\frac{k_x}{k_c}\right)^p + \left(\frac{k_y}{k_c}\right)^p \right], \tag{6.14}$$

which in real space (for comparison) is closely related to the operator

$$\frac{\partial f}{\partial t} = \frac{-i^p}{|-i^p|} \frac{M}{k_c^p} \nabla^p, \tag{6.15}$$

which are the well known diffusive operators for even powers. The eigenvalue 6.14 is a generalisation of the diffusive operator to arbitrary power, known as hyperviscosity, which allows control over the spectral index of the dissipation scale via the parameter p in addition to the parameter M. Since the real dissipation scale is not in the simulation domain, a spectral index characteristic of the true dissipation physics scaled up to the grid scale of the domain would be incorrect. The correct index would instead be a part of the turbulent cascade. Values for M and p are tested to find the ones that best reproduce the spectral index at the grid scale.

The investigation [Smith and Hammett, 1997] finds that values of $p \sim 1.7\frac{k_c}{k_a v} + 2.4$ and $M \sim 0.1S\frac{k_c}{k_a v}$ reproduce the correct spectral amplitudes across a range of grid resolutions, compared with a fully resolved simulation. We find that these values are insufficient to dissipate the turbulence in our simulations at the grid scale. In order to introduce a dissipation range near the ion Larmor radius, we simulate at a resolution of $4mm$ and modify the magnitude to $M \sim 20S\frac{k_c}{k_a v}$. Instead of the average values S and k_{av}, we use maximum values, since the SOL features a wide range of shear and transient events. The selected value of M is much larger than the values in [Smith and Hammett, 1997], although they did find this parameter more difficult to assess a scaling for, compared to the index p. We have selected this value in a best effort to retain viable physics at the dissipation scale, and kept the same specification for the index p under the assumption that this parameter is of principle importance in the dissipation model, as it showed such robust scaling in [Smith and Hammett, 1997]. A possible reason for needing such high values of M in this work compared to [Smith and Hammett, 1997], may be that M should depend on the power input from the turbulent cascade toward the grid scale, which for our case is certainly greater.

A treatment that resolves all scales down to the collisional scale of this type of plasma would require an entirely different approach, such as the gyro-fluid model [Madsen et al., 2011].

6.2 Model Equation Reference

We provide a list of simulated models for reference. Each model is a set of conditions on either the cold ion (6.16) or warm ion (6.17) models.

$$
\begin{aligned}
\partial_t n &= \frac{1}{B}\left[n,\phi\right] - \frac{n}{B^2}\left[B,\phi\right] - \frac{n_t}{l_{\|}}\sqrt{T+3T_t} + R_n + S_n, \\
\partial_t \nabla_\perp^2 \phi &= \frac{1}{n}\left[nT,B\right] + \frac{1}{B}\left[\nabla_\perp^2\phi,\phi\right] + \frac{B^2}{n}\frac{n_t}{l_{\|}}\sqrt{T+3T_t}\left(1.0 - \exp\left(F_\Lambda - \frac{e\phi}{T}\right)\right) \\
&+ R_\Omega + S_\Omega, \\
\partial_t T &= \frac{1}{B}\left[T,\phi\right] + \frac{2T}{3B^2}\left[\phi,B\right] - \frac{2T}{3l_{\|}}\sqrt{T+3T_t} + R_T + S_T.
\end{aligned}
\tag{6.16}
$$

$$
\begin{aligned}
\partial_t n &= \frac{1}{B}\left[n,\phi\right] - \frac{n}{B^2}\left[B,\phi\right] - \frac{n_t}{l_{\|}}\sqrt{T+3T_t} + R_n + S_n, \\
\partial_t \nabla_\perp^2 \phi &= \frac{1}{n}\left[2nT,B\right] + \frac{1}{B}\left[\nabla_\perp^2\phi,\phi\right] + \frac{B^2}{n}\frac{n_t}{l_{\|}}\sqrt{T+3T_t}\left(1.0 - \exp\left(F_\Lambda - \frac{e\phi}{T}\right)\right) \\
&+ \frac{1}{nB}\left(\left[\nabla_\perp^2\phi, nT\right] + \left[\vec{\nabla}_\perp\phi, \vec{\nabla}_\perp(nT)\right]\right) + R_\Omega + S_\Omega, \\
\partial_t T &= \frac{1}{B}\left[T,\phi\right] + \frac{2T}{3B^2}\left[\phi,B\right] - \frac{2T}{3l_{\|}}\sqrt{T+3T_t} + R_T + S_T.
\end{aligned}
\tag{6.17}
$$

In the following, R_C are the collision terms with no neoclassical corrections while R_{PS} represents the terms that include them. We define the reference target values, that were used in constant target simulations e.g. (6.19) as n_{t0}, T_{t0}.

6.2.1 Single Blob Simulation Conditions

The first model examined, called standard interchange (SI) for reference, is defined by the cold ion model 6.16 and the additional conditions,

$$n_t = n, \quad T_t = T, \quad F_\Lambda = 0, \quad R = R_C. \tag{6.18}$$

Const-taget interchange (CTI) is 6.16 under the conditions

$$n_t = n_t, \quad T_t = T_t, \quad F_\Lambda = 0, \quad R = R_C. \tag{6.19}$$

Const-target interchange with neo-classical collissions (CTI-PS) is 6.16 under the conditions

$$n_t = n_t, \quad T_t = T_t, \quad F_\Lambda = 0, \quad R = R_{PS} \tag{6.20}$$

Standard interchange with sheath potential drop (SI-FP3) is 6.16 under the conditions

$$n_t = n, \quad T_t = T, \quad F_\Lambda = 3.0, \quad R = R_C \tag{6.21}$$

Const-target interchange with sheath potential drop (CTI-FP3) is 6.16 under the conditions

$$n_t = n_t, \quad T_t = T_t, \quad F_\Lambda = 3.0, \quad R = R_C \tag{6.22}$$

Standard interchange with neo-classical collisions and sheath potential drop is (SI-PS-FP3) is 6.16 under the conditions

$$n_t = n, \quad T_t = T, \quad F_\Lambda = 3.0, \quad R = R_{PS} \tag{6.23}$$

Standard interchange with warm ion effects is 6.17 under the conditions

$$n_t = n, \quad T_t = T, \quad F_\Lambda = 0, \quad R = R_C \tag{6.24}$$

Standard interchange with warm ion effects and sheath potential drop is 6.17 under the conditions

$$n_t = n, \quad T_t = T, \quad F_\Lambda = 3.0, \quad R = R_C \tag{6.25}$$

Const-target interchange with warm ion effects and sheath potential drop is 6.17 under the conditions

$$n_t = n_t, \quad T_t = T_t, \quad F_\Lambda = 3.0, \quad R = R_C \tag{6.26}$$

Const-target interchange with averaged divertor values is 6.16 under the conditions

$$n_t = \langle n(x,y) \rangle_{(x,y)}, \quad T_t = \langle T(x,y) \rangle_{(x,y)}, \quad F_\Lambda = 0, \quad R = R_C \tag{6.27}$$

Const-target interchange with averaged divertor values and sheath potential drop is 6.16 under the conditions

$$n_t = \langle n(x,y) \rangle_{(x,y)}, \quad T_t = \langle T(x,y) \rangle_{(x,y)}, \quad F_\Lambda = 3.0, \quad R = R_C \tag{6.28}$$

Const-target interchange with averaged divertor values, warm ion effects and sheath potential drop is 6.17 under the conditions

$$n_t = \langle n(x,y) \rangle_{(x,y)}, \quad T_t = \langle T(x,y) \rangle_{(x,y)}, \quad F_\Lambda = 3.0, \quad R = R_C \tag{6.29}$$

Standard interchange with divertor values kept as a fixed fraction of the simulated values is 6.16 under the conditions

$$n_t = n\frac{\langle n_{t0}(x,y) \rangle_{(x,y)}}{\langle n(x,y) \rangle_{(x,y)}}, \quad T_t = T\frac{\langle T_{t0}(x,y) \rangle_{(x,y)}}{\langle T(x,y) \rangle_{(x,y)}}, \quad F_\Lambda = 0, \quad R = R_C \tag{6.30}$$

Standard interchange with divertor values kept as a fixed fraction of the simulated values with sheath potential drop is 6.16 under the conditions

$$n_t = n\frac{\langle n_{t0}(x,y) \rangle_{(x,y)}}{\langle n(x,y) \rangle_{(x,y)}}, \quad T_t = T\frac{\langle T_{t0}(x,y) \rangle_{(x,y)}}{\langle T(x,y) \rangle_{(x,y)}}, \quad F_\Lambda = 3.0, \quad R = R_C \tag{6.31}$$

Standard interchange with divertor values kept as a fixed fraction of the simulated values, warm ion effects and sheath potential drop is 6.17 under the conditions

$$n_t = n\frac{\langle n_{t0}(x,y) \rangle_{(x,y)}}{\langle n(x,y) \rangle_{(x,y)}}, \quad T_t = T\frac{\langle T_{t0}(x,y) \rangle_{(x,y)}}{\langle T(x,y) \rangle_{(x,y)}}, \quad F_\Lambda = 3.0, \quad R = R_C \tag{6.32}$$

6.2.2 SOL Simulation Conditions

The first SOL model examined, called standard interchange (SOL-SI-PS) is defined by the cold ion model 6.16 and the additional conditions,

$$n_t = n, \quad T_t = T, \quad F_\Lambda = 0, \quad R = R_{PS}. \tag{6.33}$$

Standard interchange (SOL-SI-PS-FTI) is 6.17 under the conditions

$$n_t = n, \quad T_t = T, \quad F_\Lambda = 0, \quad R = R_{PS}. \tag{6.34}$$

Const-target interchange with neo-PS collissions (SOL-CTI-PS-FTI) is 6.17 under the conditions

$$n_t = n_t, \quad T_t = T_t, \quad F_\Lambda = 0, \quad R = R_{PS} \tag{6.35}$$

Standard interchange with sheath potential drop (SOL-SI-PS-FP3-FTI) is 6.17 under the conditions

$$n_t = n, \quad T_t = T, \quad F_\Lambda = 3.0, \quad R = R_{PS} \tag{6.36}$$

Const-target interchange with sheath potential drop (SOL-CTI-PS-FP3-FTI) is 6.17 under the conditions

$$n_t = n_t, \quad T_t = T_t, \quad F_\Lambda = 3.0, \quad R = R_{PS} \tag{6.37}$$

6.3 Single blob behaviour

In order to examine the behaviour of filaments in the regimes hTOKER can simulate, we perform a number of simulations with combinations of effects turned on or off. The const-target boundary conditions were set to MAST values, which are about an order of magnitude less than the mid-plane values. This means that in addition to providing homogeneity to the parallel terms, the magnitude is also greatly reduced. These simulations were run for $2 \times 10^3 \omega_0^{-1}$, with a timestep $0.1\omega_0^{-1}$. Source terms S_n, S_Ω, S_T were set to zero.

6.3.1 Const-Target and PS Effects on Standard Interchange

We begin by investigating the effect of the constant target boundary conditions upon the standard sheath driven interchange, with no sheath potential drop at the target plates, for comparison with these effects switched on. We examine the standard sheath interchange, the effect of the const target conditions, and the effects of including the neoclassical Pfirsch Schulter diffusion.

Standard Sheath-Interchange

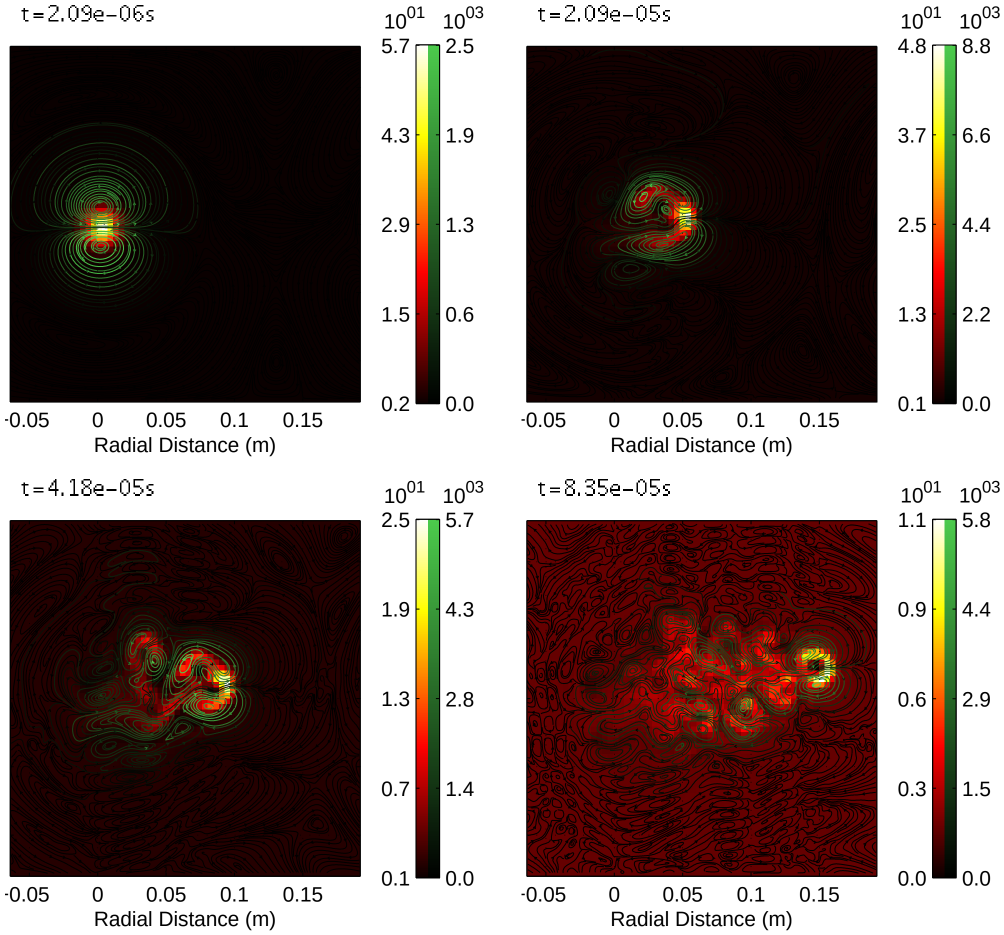

Figure 6.2: Simulation Designation: SI (6.18), Blob Size = 0.02m, Background = $10^{18}m^{-3}$, $10eV$, Blob Peak = $5 \times 10^{18}m^{-3}$, $50eV$, Parallel Model = Flute, Collisions = Classical, Sheath Potential Drop = 0, Ion Temperature = 0. Streamlines of velocity shown in green (kms^{-1}), plasma pressure shown in red-yellow (pA).

The standard interchange scenario, provided for reference, consists of the generation of vorticity leading to the radial advection of he blob.

Const-Target Interchange

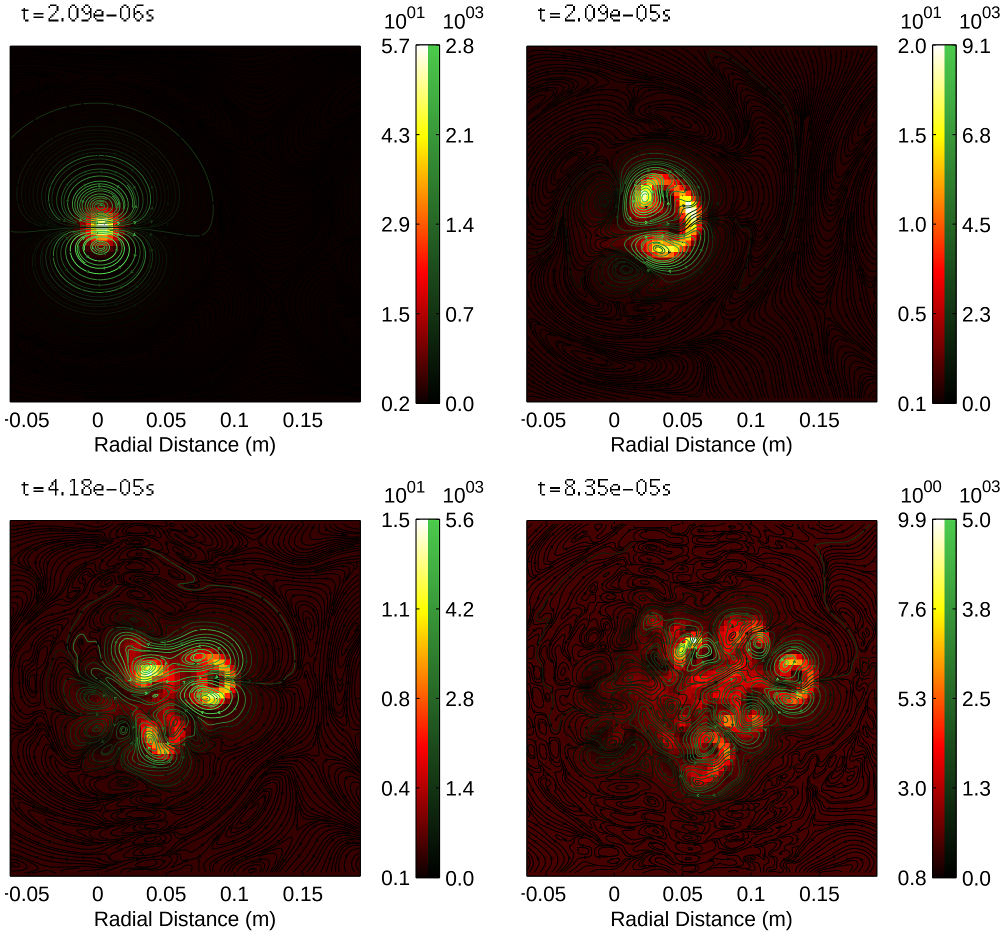

Figure 6.3: Simulation Designation: CTI (6.19), Blob Size = 0.02m, Background = $10^{18}m^{-3}$, $10eV$, Blob Peak = $5 \times 10^{18}m^{-3}$, $50eV$, Parallel Model = Constant Target (MAST Profiles), Collisions = Classical, Sheath Potential Drop = 0, Ion Temperature = 0. Streamlines of velocity shown in green (kms^{-1}), plasma pressure shown in red-yellow (pA).

Under constant target boundary conditions, set to the experimentally measured values on MAST, there is an increased radial velocity at early times accompanied by an increased disruption of the structure and a reduced travel distance of the filament at later times. This may be due to the reduction in sheath current magnitude as opposed to its structure.

Const-Target with Pfirsch Schlter Diffusion

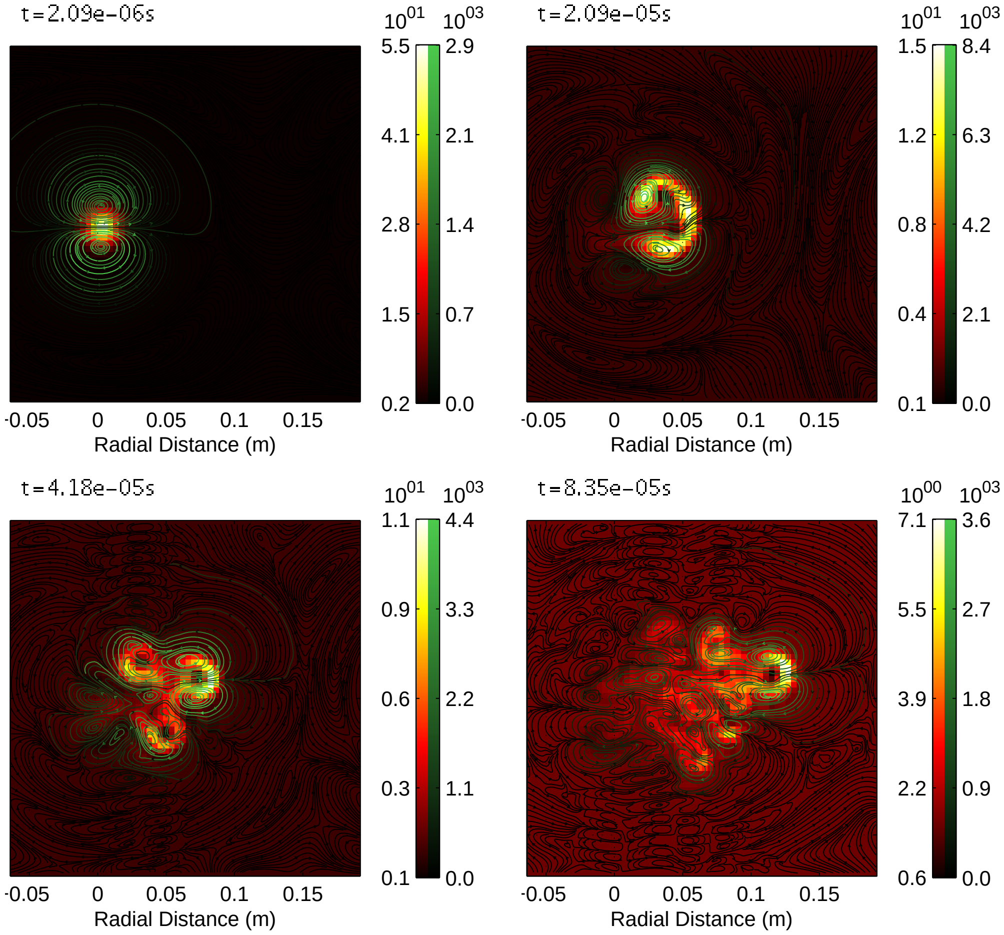

Figure 6.4: Simulation Designation: CTI-PS (6.20), Blob Size = 0.02m, Background = $10^{18}m^{-3}$, $10eV$, Blob Peak = $5 \times 10^{18}m^{-3}$, $50eV$, Parallel Model = Constant Target (MAST Profiles), Collisions = Neo-Classical, Sheath Potential Drop = 0, Ion Temperature = 0. Streamlines of velocity shown in green (kms^{-1}), plasma pressure shown in red-yellow (pA).

Including the neoclassical diffusion, we find a reduction in the radial velocity, which must be linked to the two dimensional structure of the blob vorticity since the neoclassical diffusion acts in the radial direction.

6.3.2 Const-Target and PS Effects on Sheath Potential Interchange

The effect of the Bohm sheath potential drop on the plasma filaments, as discussed, is to generate a spin centred on the centre of the blob. This leads, as already reported Myra et al. [2004], to a reduction in the radial velocity and the generation of a polodial velocity for the blob. This blob also becomes far more stable, replacing flow-shear instabilities for centrifugal instabilities.

Standard Interchange with FPV=3.0

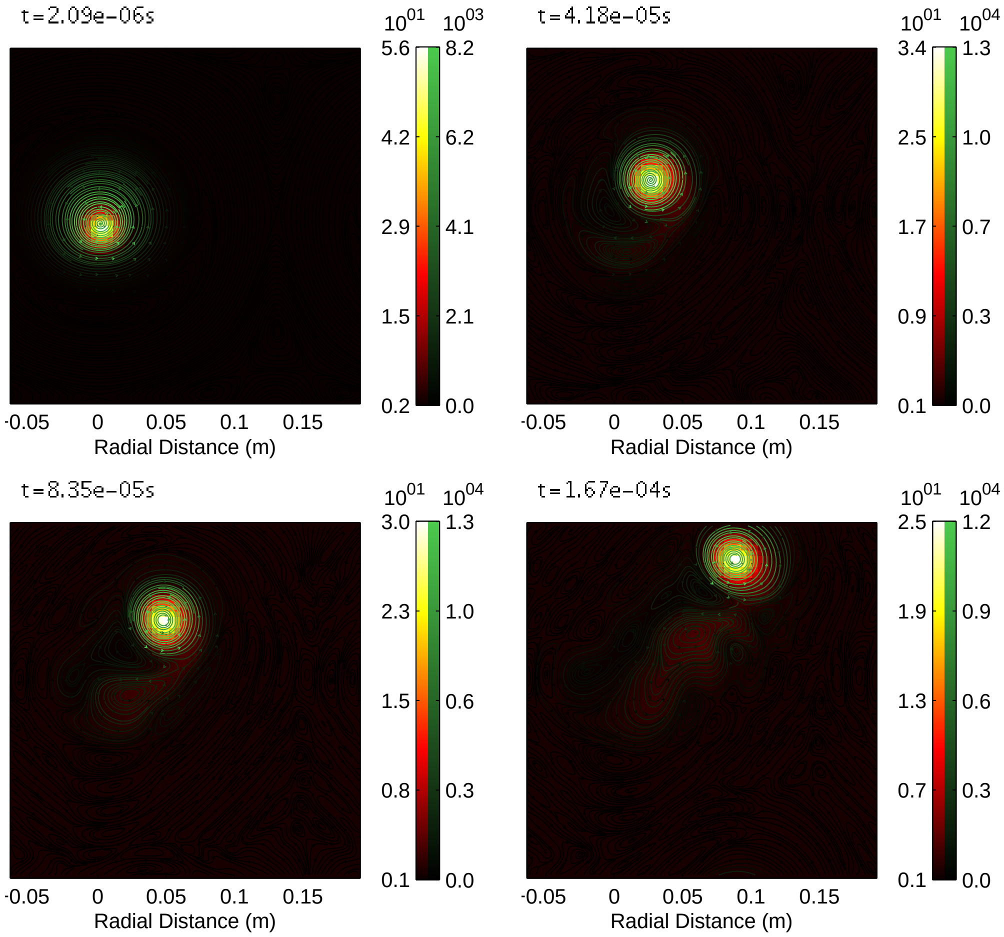

Figure 6.5: Simulation Designation: SI-FP3 (6.21), Blob Size = 0.02m, Background = $10^{18}m^{-3}$, $10eV$, Blob Peak = $5 \times 10^{18}m^{-3}$, $50eV$, Parallel Model = Flute, Collisions = Classical, Sheath Potential Drop = $3.0\frac{T_e}{e}$, Ion Temperature = 0. Streamlines of velocity shown in green (kms^{-1}), plasma pressure shown in red-yellow (pA).

The standard case of blob advection with the action of a Bohm sheath potential drop in the vorticity equation is given for reference. The blob size and amplitude chosen is stable to the centrifugal instability, remaining a coherent structure for a long period.

Const-Target Interchange with FPV=3.0

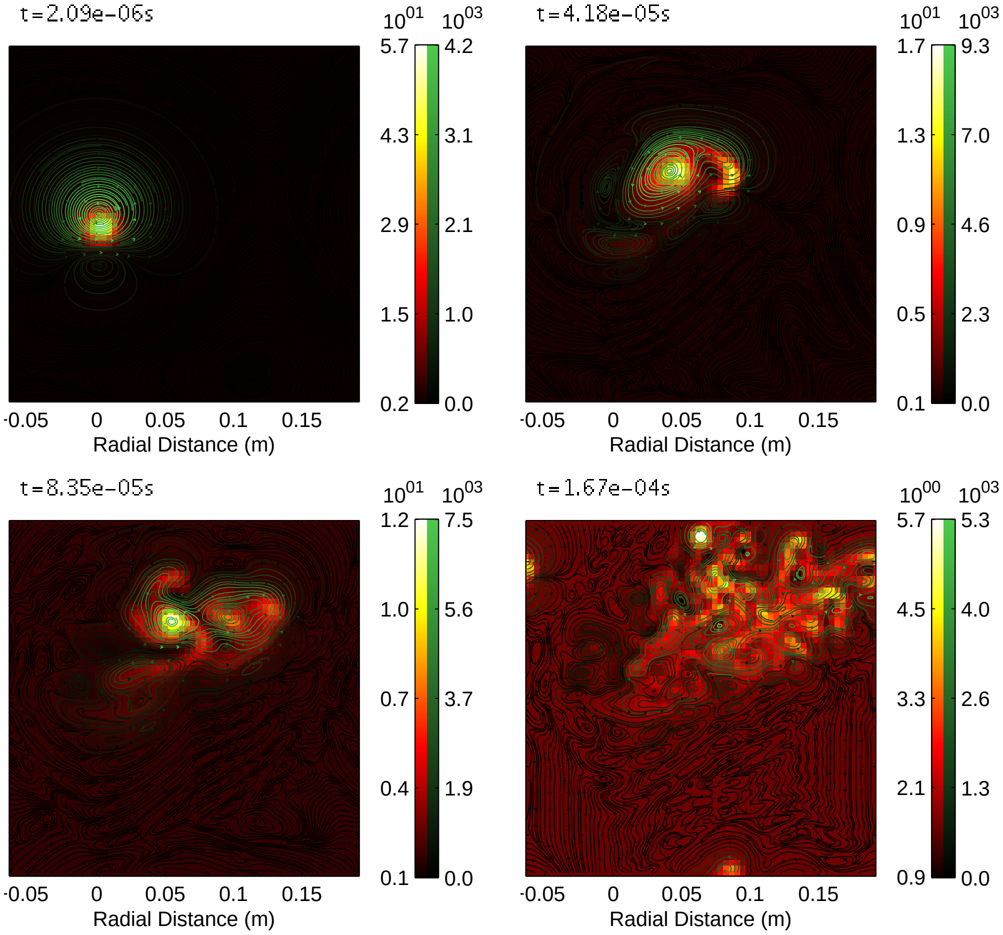

Figure 6.6: Simulation Designation: CTI-FP3 (6.22), Blob Size = 0.02m, Background = $10^{18}m^{-3}$, $10eV$, Blob Peak = $5 \times 10^{18}m^{-3}$, $50eV$, Parallel Model = Constant Target (MAST Profiles), Collisions = Classical, Sheath Potential Drop = $3.0\frac{T_e}{e}$, Ion Temperature = 0. Streamlines of velocity shown in green (kms^{-1}), plasma pressure shown in red-yellow (pA).

Under constant target boundary conditions, the stability of the blob is reduced, due to an increase of interchange potential generated in the blob. Again, this may be primarily due to the drop in sheath current magnitude by one order over the standard case, as opposed to any spatial changes in the sheath currents.

Standard Interchange with PS Diffusion and FPV=3.0

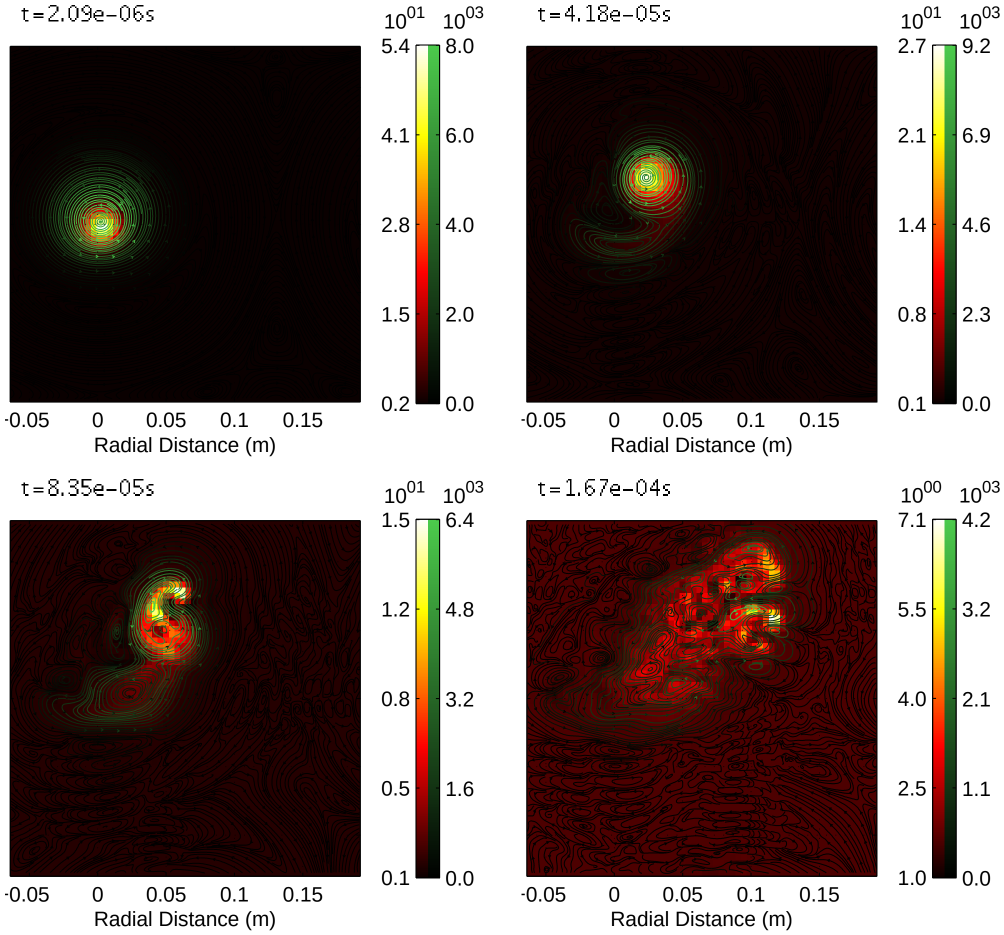

Figure 6.7: Simulation Designation: SI-PS-FP3 (6.23), Blob Size = 0.02m, Background = $10^{18}m^{-3}$, $10eV$, Blob Peak = $5 \times 10^{18}m^{-3}$, $50eV$, Parallel Model = Flute, Collisions = Neo-Classical, Sheath Potential Drop = $3.0\frac{T_e}{e}$, Ion Temperature = 0. Streamlines of velocity shown in green (kms^{-1}), plasma pressure shown in red-yellow (pA).

Pfirsch Schulter diffusion also appears to destabilise the rotational stability of the blob, causing a breakdown compared to the base case at late times.

6.3.3 Warm Ion Effects and Interaction with Const-Target, Pfirsch-Schulter Diffusion and Bohm potential Interchange

The approximate inclusion of the warm ion effects in the vorticity equation, given by (6.17) compared to (6.16), leads to the rotation of the interchange potential into the polodial direction. This, to first order, can be considered as a secondary interchange generated by the gradient of vorticity in the polodial direction that was generated by the initial interchange, comparing terms 1 and 4 of (6.17).

Standard Interchange with Warm Ion Effects

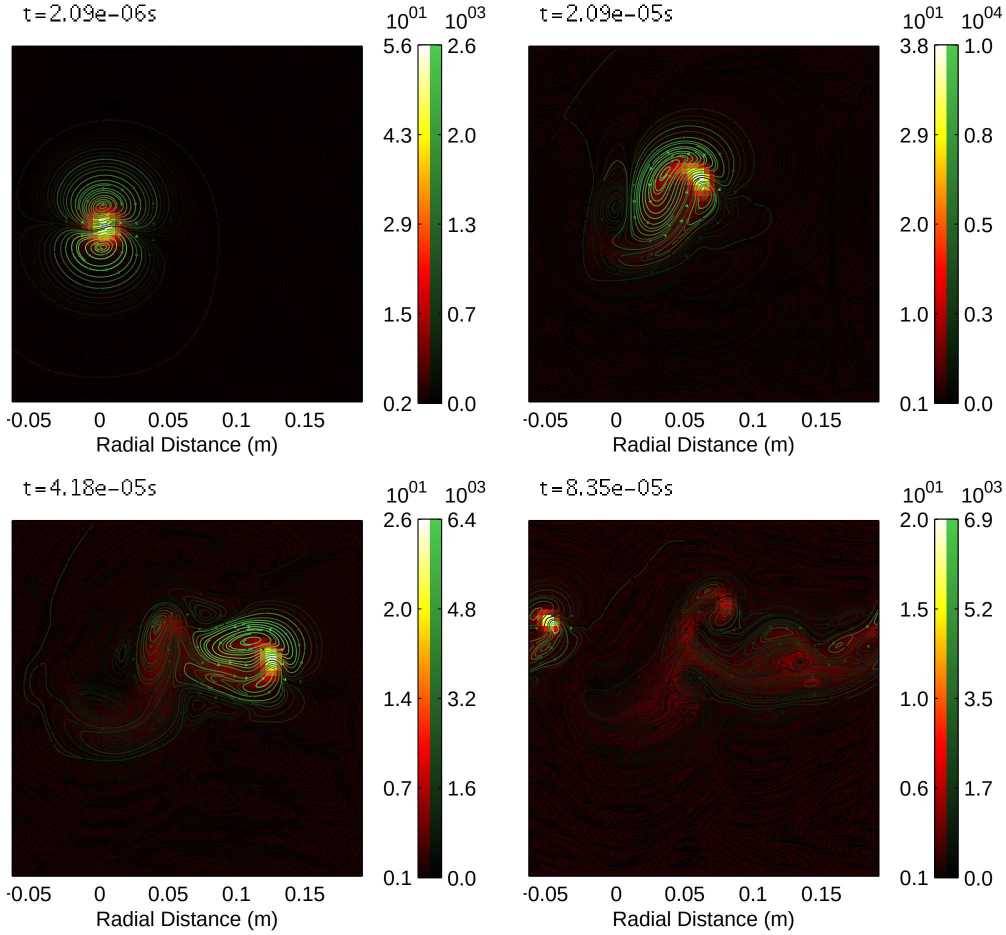

Figure 6.8: Simulation Designation: SI-FTI (6.24), Blob Size = 0.02m, Background = $10^{18}m^{-3}$, $10eV$, Blob Peak = $5 \times 10^{18}m^{-3}$, $50eV$, Parallel Model = Flute, Collisions = Classical, Sheath Potential Drop = 0, Ion Temperature = Electron Temperature. Streamlines of velocity shown in green (kms^{-1}), plasma pressure shown in red-yellow (pA).

The base case including the warm ion effects leads to advection of the blob in the polodial direction, which is an inherently dynamic process since this polodial velocity depends explicitly on the radial velocity generated by the interchange due to the term proportional to $[\nabla_\perp^2\phi, nT]$. Also, the effects have stabilised the blob, and it remains a coherent structure for a long period, with a very large displacement.

Standard Interchange with Warm Ion Effects and FPV=3.0

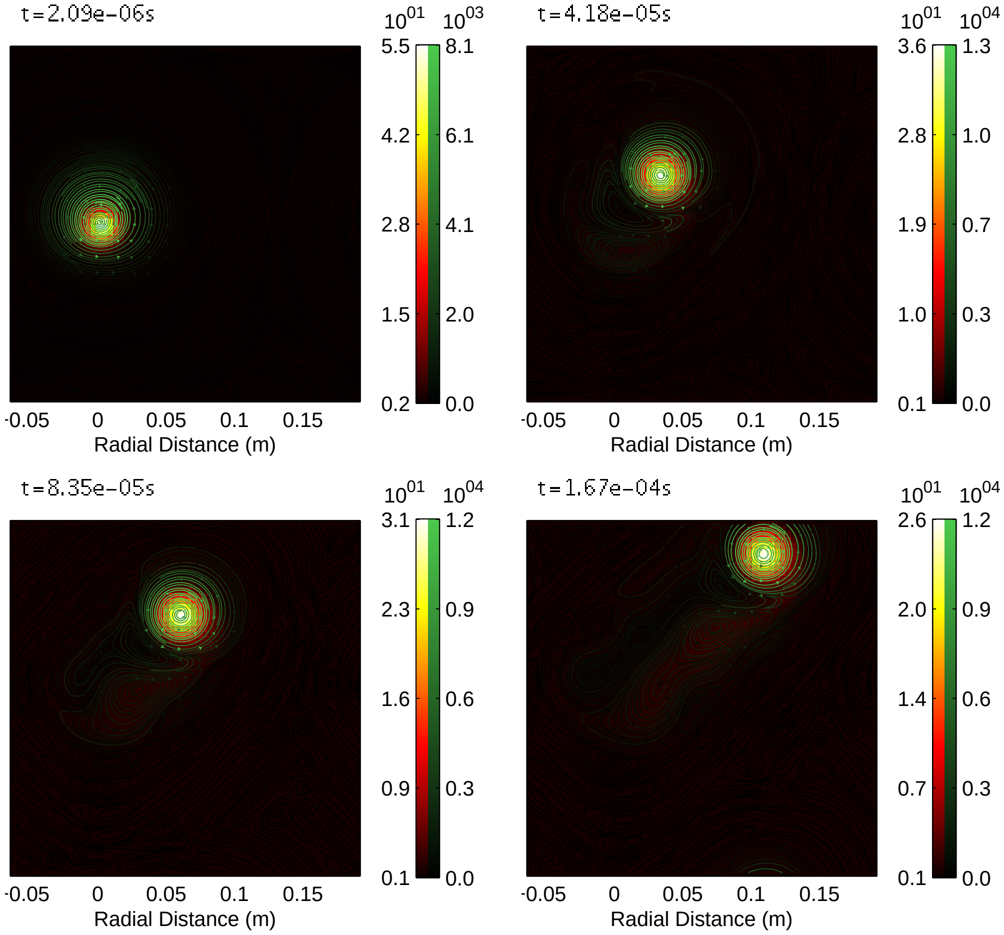

Figure 6.9: Simulation Designation: SI-FP3-FTI (6.25), Blob Size = 0.02m, Background = $10^{18} m^{-3}$, $10eV$, Blob Peak = $5 \times 10^{18} m^{-3}$, $50eV$, Parallel Model = Flute, Collisions = Classical, Sheath Potential Drop = $3.0\frac{T_e}{e}$, Ion Temperature = Electron Temperature. Streamlines of velocity shown in green (kms^{-1}), plasma pressure shown in red-yellow (pA).

The interaction of the warm ion effects and the Bohm sheath potential does not appear to destabilise the blob. Indeed, the structure of the blob appears if anything more stabilised in the presence of warm ions.

Const-Target Interchange with Warm Ion Effects and FPV=3.0

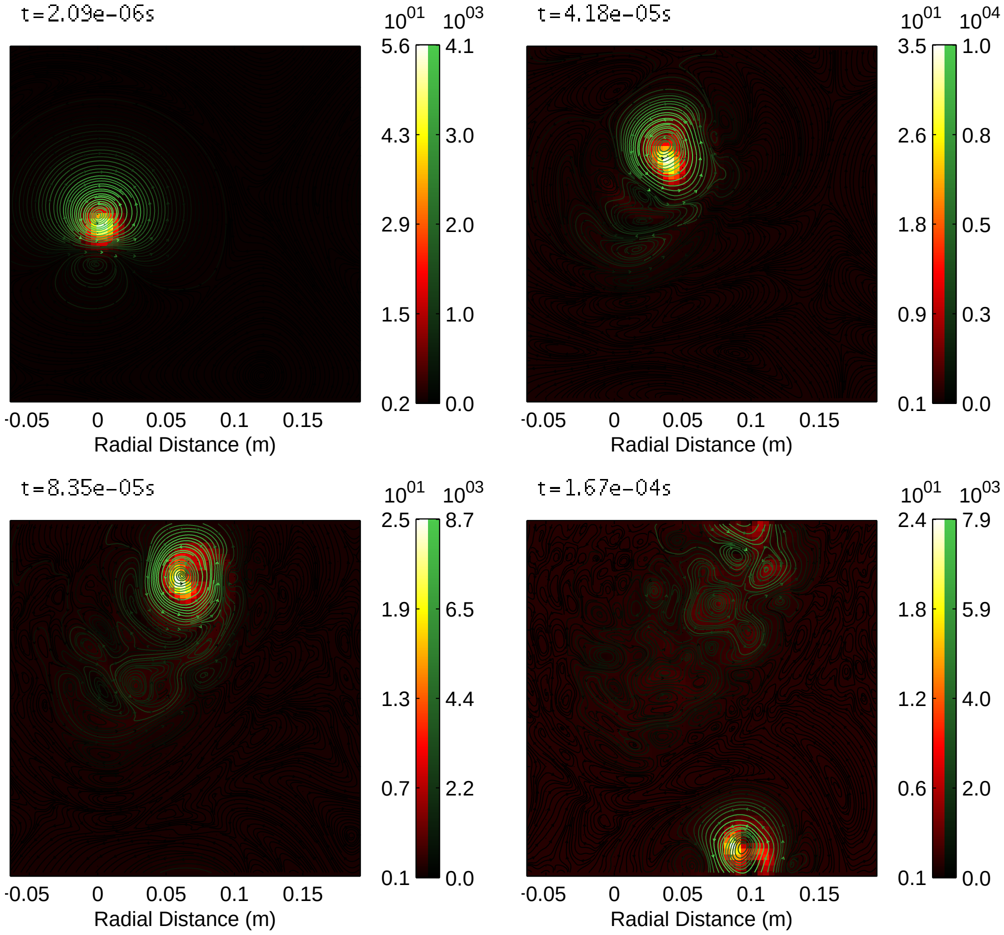

Figure 6.10: Simulation Designation: CTI-FP3-FTI (6.26), Blob Size = 0.02m, Background = $10^{18}m^{-3}$, $10eV$, Blob Peak = $5 \times 10^{18}m^{-3}$, $50eV$, Parallel Model = Constant Target (MAST Profiles), Collisions = Classical, Sheath Potential Drop = $3.0\frac{T_e}{e}$, Ion Temperature = Electron Temperature. Streamlines of velocity shown in green (kms^{-1}), plasma pressure shown in red-yellow (pA).

The const target case with Bohm sheath effects was unstable for our blob parameter choice with cold ions, and since the warm ions were predicted to add to the stability of rotation blobs, we might expect to see an increased stability with their inclusion to the blob dynamics. The blob shows increased stability, however, the velocity field does not seems as regular as compared to SI-FP3-FTI.

6.3.4 Const-Target Interchange with equivalent target values

The const-target blob simulations from the previous section are computed again with the modification that the divertor quantities are completely uniform and take for each timestep the averaged values of the simulated values, so that spatial structure is removed from the simulations while preserving the approximate magnitude of the sheath current in the standard case. This is in order to examine the effect of the spatial invariance of the target quantities in the sheath currents on the blob stability, compared to the standard case. To clarify, we set

Const-Target Interchange

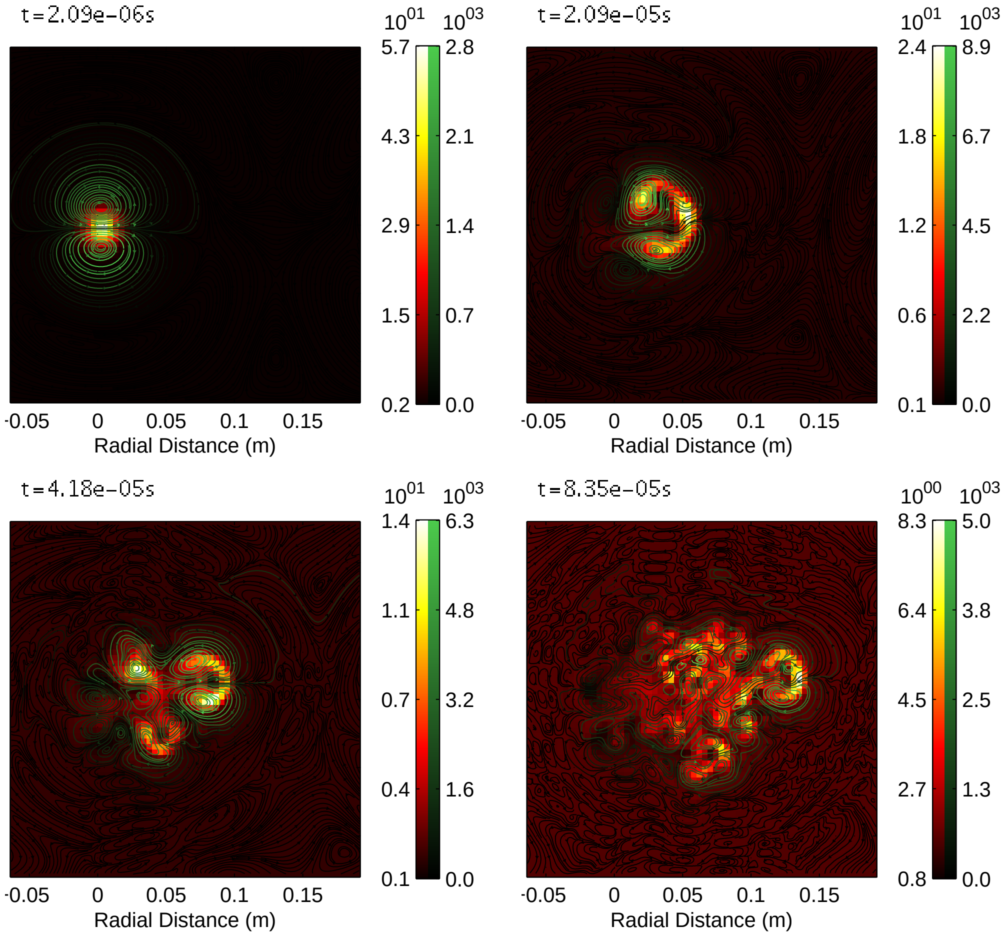

Figure 6.11: Simulation Designation: aCTI (6.27), Blob Size = 0.02m, Background = $10^{18}m^{-3}$, $10eV$, Blob Peak = $5 \times 10^{18}m^{-3}$, $50eV$, Parallel Model = Constant Target (Mean of Plasma), Collisions = Classical, Sheath Potential Drop = 0, Ion Temperature = 0. Streamlines of velocity shown in green (kms^{-1}), plasma pressure shown in red-yellow (pA).

There is a relatively small change the radial velocity as a result of the increased sheath current strength, however, the disruption of the blob structure, and the propagation distance are almost identical when compared to CTI (6.19).

Const-Target Interchange with FPV=3.0

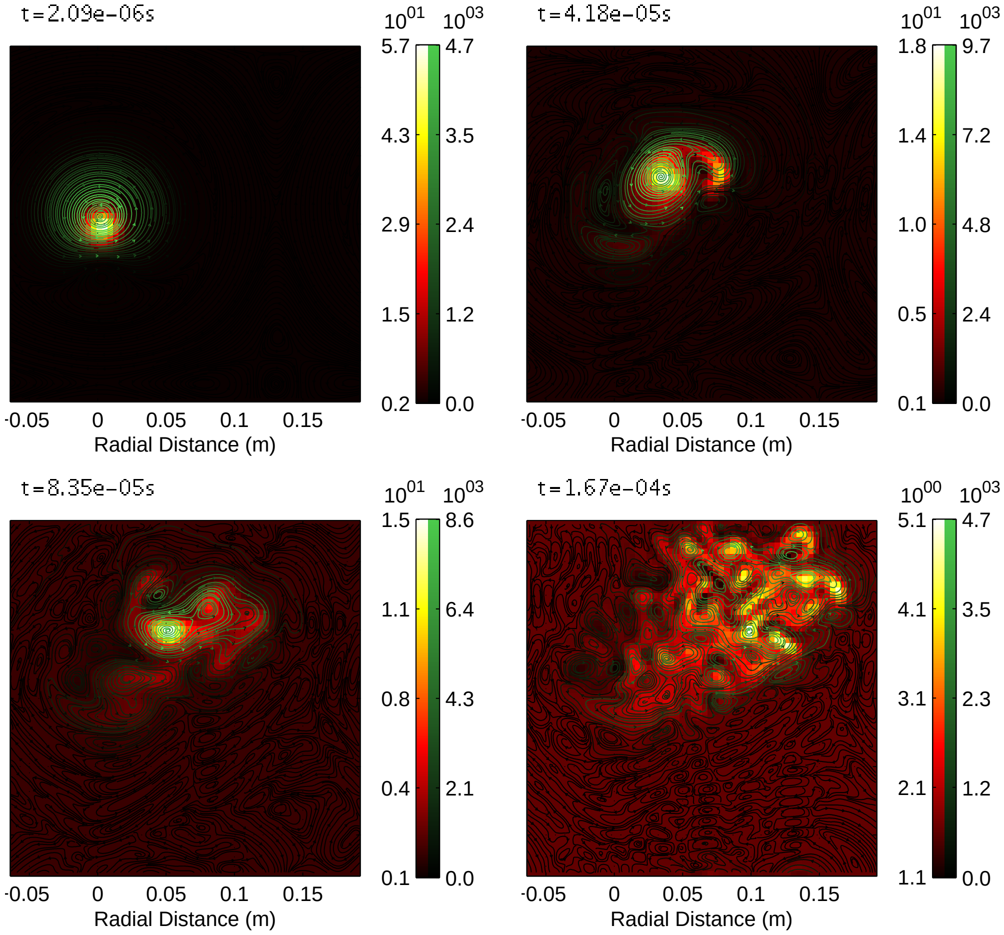

Figure 6.12: Simulation Designation: aCTI-FP3 (6.28), Blob Size = 0.02m, Background = $10^{18}m^{-3}$, $10eV$, Blob Peak = $5 \times 10^{18}m^{-3}$, $50eV$, Parallel Model = Constant Target (Mean of Plasma), Collisions = Classical, Sheath Potential Drop = $3.0\frac{T_e}{e}$, Ion Temperature = 0. Streamlines of velocity shown in green (kms^{-1}), plasma pressure shown in red-yellow (pA).

For target quantities with spatial structure comparable to CTI-FP3 (6.22) and the magnitude in SI-FP3 (6.21), the blob is destabilised at late times as it is in CTI-FP3 (6.22), implying that the structure of the target quantities is a key factor in the stability of blobs with vorticity affected by a sheath potential drop.

Const-Target Interchange with Warm Ion Effects and FPV=3.0

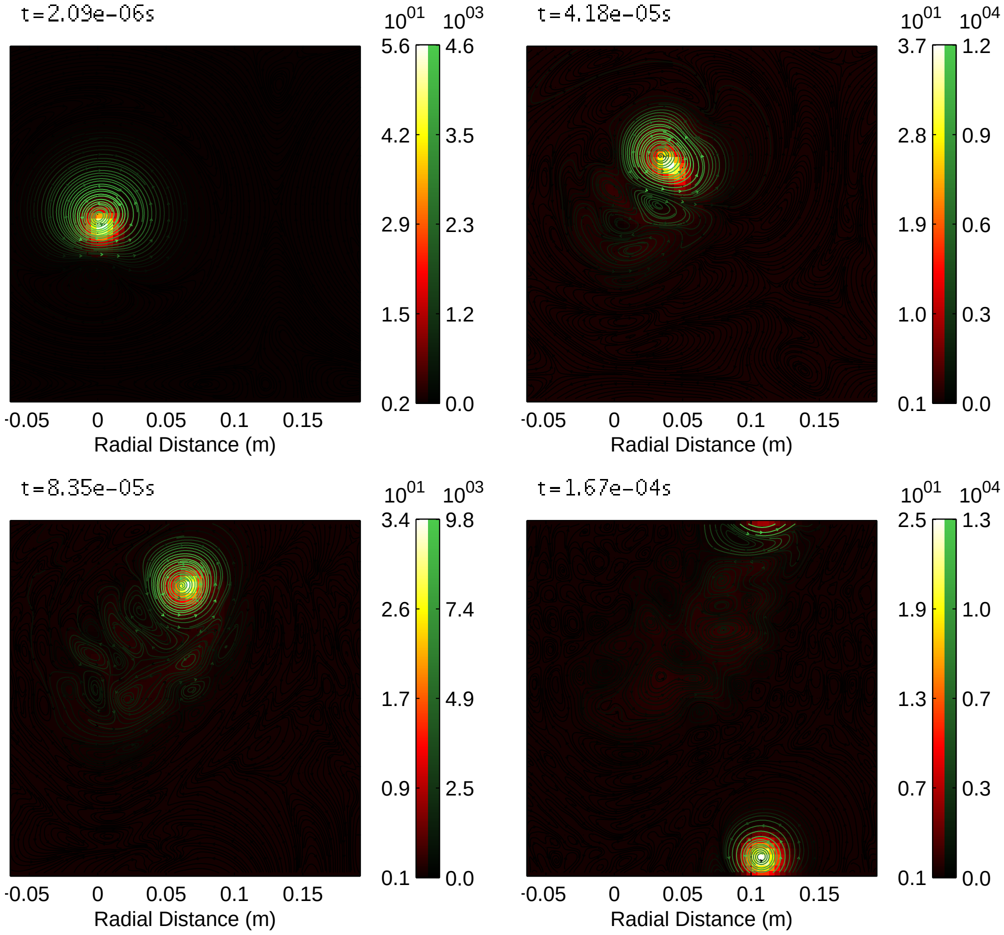

Figure 6.13: Simulation Designation: aCTI-FP3-FTI (6.29), Blob Size = 0.02m, Background = $10^{18} m^{-3}$, $10 eV$, Blob Peak = $5 \times 10^{18} m^{-3}$, $50 eV$, Parallel Model = Constant Target (Mean of Plasma), Collisions = Classical, Sheath Potential Drop = $3.0 \frac{T_e}{e}$, Ion Temperature = Electron Temperature. Streamlines of velocity shown in green (kms^{-1}), plasma pressure shown in red-yellow (pA).

With sheath current magnitude comparable to SI-FP3 (6.21) and spatial structure comparable to CTI-FP3 (6.22), stability is increased relative to aCTI-FP3 leading to an evolution more similar to SI-FP3. Whatever destabilising effect present in CTI-FP3 (6.22) and aCTI-FP3 (6.28), perhaps due to sheath current structure, is stabilised in both cases CTI-FP3-FTI (6.26) and aCTI-FP3-FTI (6.29) by finite ion temperature effects.

6.3.5 Standard Interchange with equivalent target values

It appears the spatial structure of the target quantities is a large factor in the stability of the simulated blobs. We therefore additionally check the standard cases (SI-FP3,SI-FP3-FTI), which appear to have a stabilising structure, in the case where target values are equal to a fraction of the bulk plasma values, to approximate the measured target values in MAST.

The fraction used was calculated at each timestep, so that the mean of the divertor density was equal to the mean in the constant target cases. The velocity fields created were substantially larger than the previous simulations, therefore the simulation domain was doubled in size.

Standard Interchange

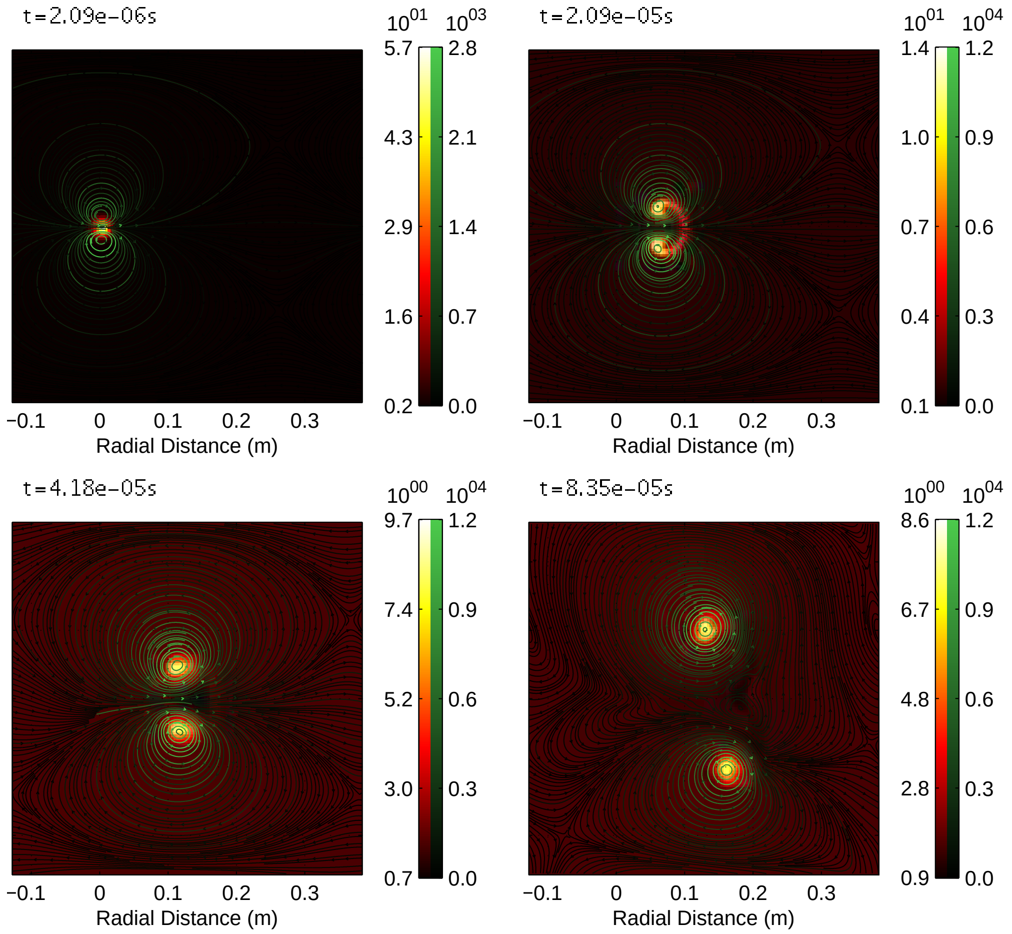

Figure 6.14: Simulation Designation: rtSI (6.30), Blob Size = 0.02m, Background = $10^{18}m^{-3}$, $10eV$, Blob Peak = $5 \times 10^{18}m^{-3}$, $50eV$, Parallel Model = Flute, Collisions = Classical, Sheath Potential Drop = 0, Ion Temperature = 0. Streamlines of velocity shown in green (kms^{-1}), plasma pressure shown in red-yellow (pA).

Similar to the counterparts SI (6.18) and CTI (6.19) in terms of propagation distance, excepting that there is a dominant dipolar vorticity structure in this case. This dipole splits into two separate blobs at late times.

Standard Interchange with FPV=3.0

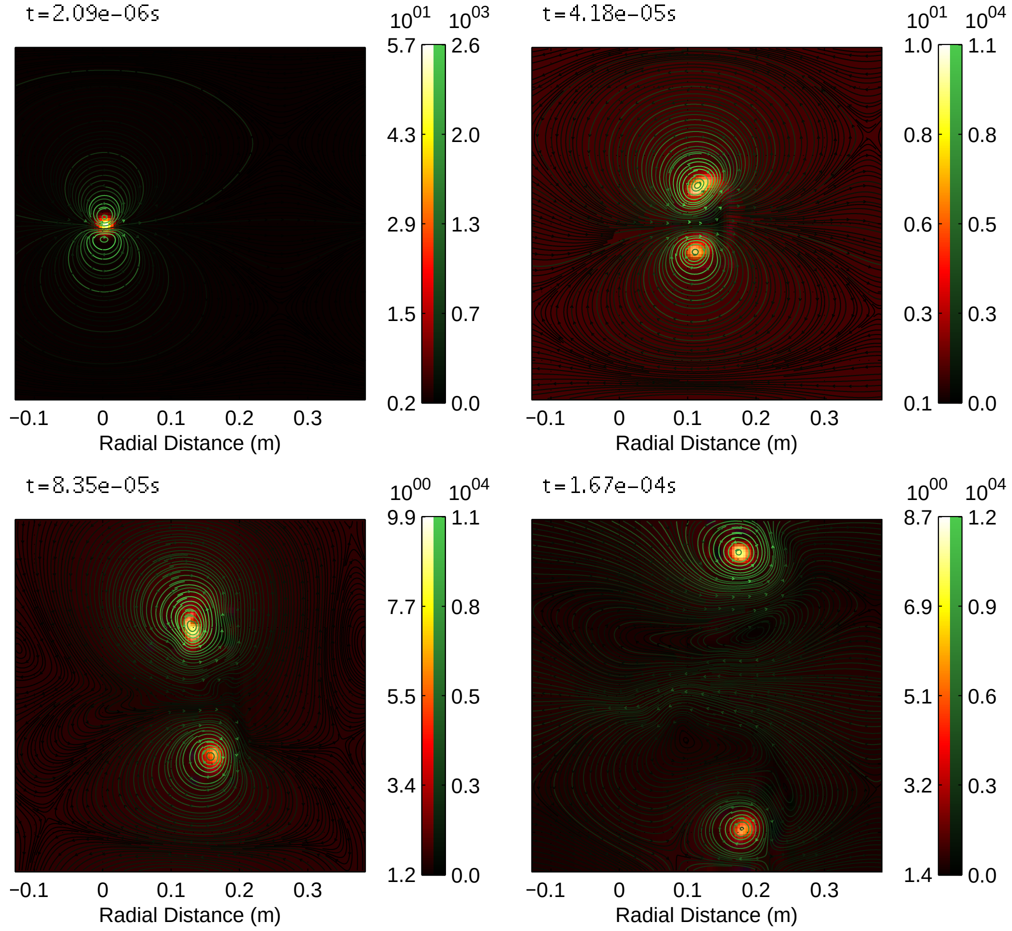

Figure 6.15: Simulation Designation: rtSI-FP3 (6.31), Blob Size = 0.02m, Background = $10^{18}m^{-3}$, $10eV$, Blob Peak = $5 \times 10^{18}m^{-3}$, $50eV$, Parallel Model = Flute, Collisions = Classical, Sheath Potential Drop = $3.0\frac{T_e}{e}$, Ion Temperature = 0. Streamlines of velocity shown in green (kms^{-1}), plasma pressure shown in red-yellow (pA).

Compared to CTI-FP3 (6.22) and aCTI-FP3 (6.28), structure is far more stable. The evolution is very similar to the case with no sheath potential drop (6.30). It seems that a uniform structure sheath current can interfere with the effects of the sheath potential drop, while even a weak sheath current with the flute like structure of SI-FP3 (6.21) may not.

Standard Interchange with Warm Ion Effects and FPV=3.0

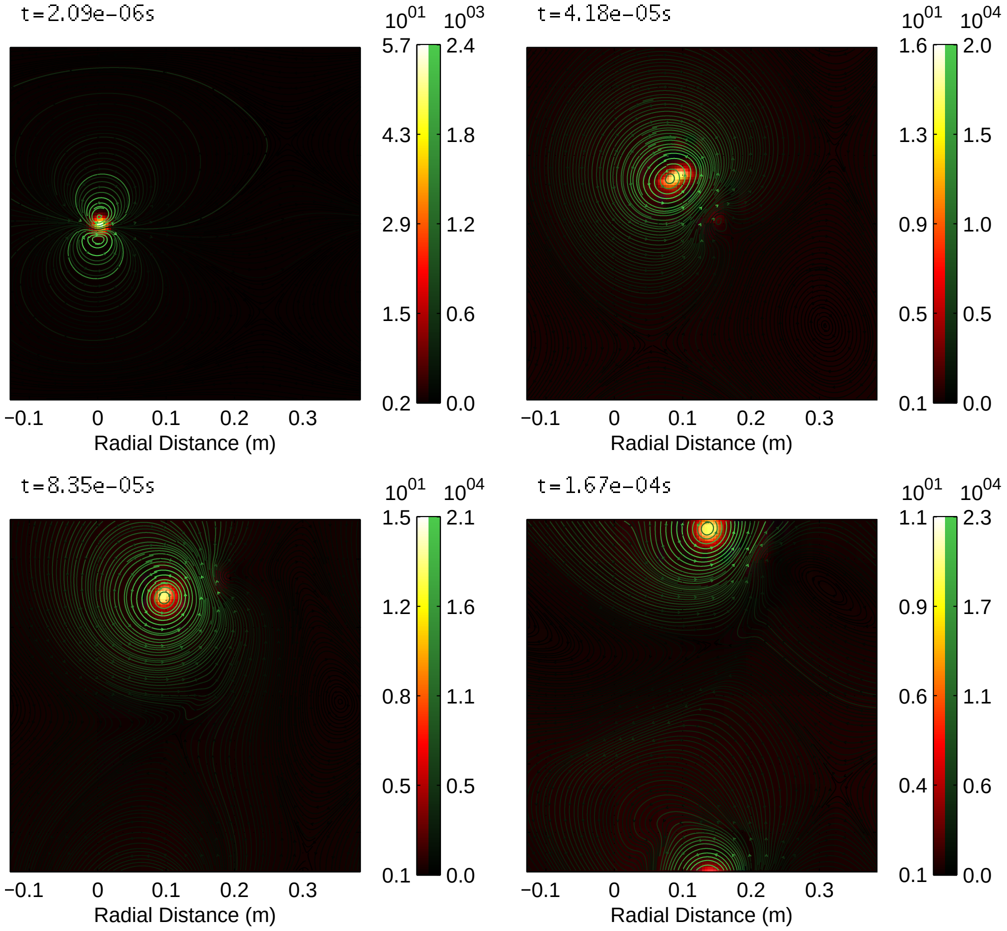

Figure 6.16: Simulation Designation: rtSI-FP3-FTI (6.32), Blob Size = 0.02m, Background = $10^{18}m^{-3}$, $10eV$, Blob Peak = $5 \times 10^{18}m^{-3}$, $50eV$, Parallel Model = Flute, Collisions = Classical, Sheath Potential Drop = $3.0\frac{T_e}{e}$, Ion Temperature = Electron Temperature. Streamlines of velocity shown in green (kms^{-1}), plasma pressure shown in red-yellow (pA).

This blob is similarly stable compared to both CTI-FP3-FTI (6.26) and aCTI-FP3-FTI (6.29), however, it has a larger spatial scale of the velocity field. It appears that the finite ion temperature effects are acting to improve the blob stability in all cases.

6.4 Sheath model and floating potential effects on SOL turbulence

Evidently, the differences between flute and const-target modelling of the parallel current lead to differences in blob advection. Additionally, consideration of the sheath potential drop leads to stabilised blobs with reduced radial advection that may or may not retain stability depending upon the model chosen for the target quantities. A SOL plasma simulation will therefore have power deposition characteristics that depend on these modelling considerations. We simulate 5 long-term SOL plasmas, using the MAST blob-source distributions and parameters in the interest of exploring the differences between the models. The SOL simulations have source and damping terms in the form of blobs picked from the distributions 6.1 and sheath dissipation of density and temperature. The dissipation terms for density and temperature always take the form $n\nabla_{\|}v_{\|}$ and $T\nabla_{\|}v_{\|}$, regardless of the parallel model so that purely the effects of the vorticity model are considered. Tables of parameters for the simulated plasmas are given in tables 6.1 and 6.2; characteristic snapshots of each simulation are shown in figures 6.17 to 6.21.

l_x	$1.024m$	l_y	$0.256m$
NX	512	NY	128
$l_{\|}$	$15m$	σ_t	$0.15m$
A_{nt}	$7.3 \times 10^{17} m^{-3}$	A_{Tt}	$13eV$
t_{sim}	$5 \times 10^4 \omega_0^{-1}$	Δt	$0.1\omega_0^{-1}$

Table 6.1: Parameters used in the hTOKER SOL simulations. The values l_x, l_y, NX, NY define the grid length and number of grid points in the x (radial) and y (polodial) directions respectively. The parallel length $l_{\|}$ was approximated as a constant, while the target values of temperature and density approximated as Gaussian functions centred about the LCFS, which itself is located at $x = NX/2$. The values A_{nt} and A_{Tt} are the amplitude of the Gaussian for target density and target temperature respectively. The width of the Gaussian is given by the length σ_t. Finally, with $\omega_0 = \frac{eB_0}{m_i}$, the parameter t_{sim} gives the run time of the simulation and Δt the time step.

Designation	Parallel Model	Λ	$T_{i\perp}$
SOL-SI-PS	Flute	0	0
SOL-SI-PS-FTI	Flute	0	T_e
SOL-SI-PS-FP3-FTI	Flute	$3.0\frac{T_e}{e}$	T_e
SOL-CTI-PS-FTI	Constant Target	0	T_e
SOL-CTI-PS-FP3-FTI	Constant Target	$3.0\frac{T_e}{e}$	T_e

Table 6.2: Simulations and designations. Flute model gives target quantities (temperature and density) equal to bulk plasma quantities, while constant target model has independent target quantities, given by measured target quantities on MAST.

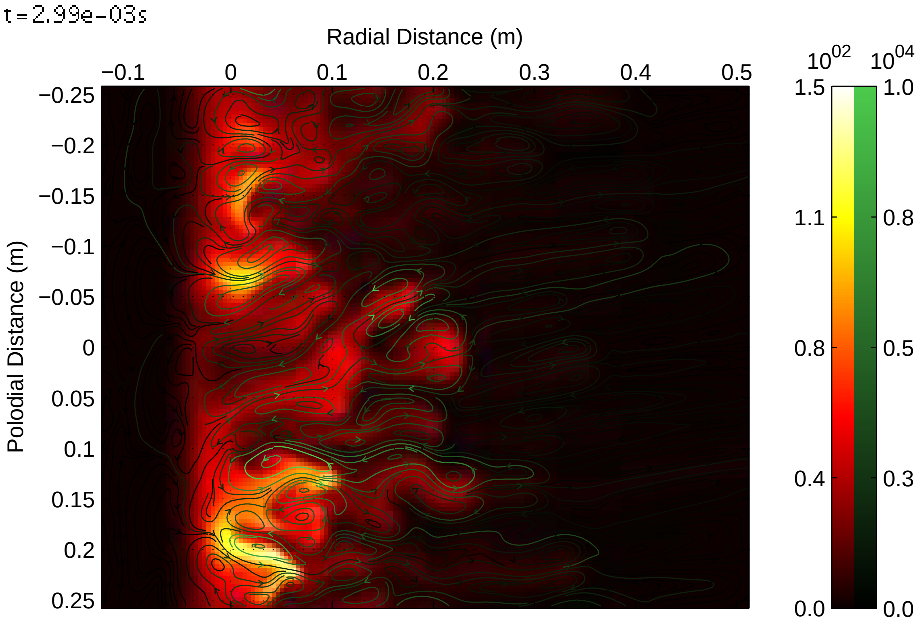

Figure 6.17: Snapshot of simulation SOL-SI-PS (6.33). Streamlines of velocity shown in green (kms^{-1}), plasma pressure shown in red-yellow (pA).

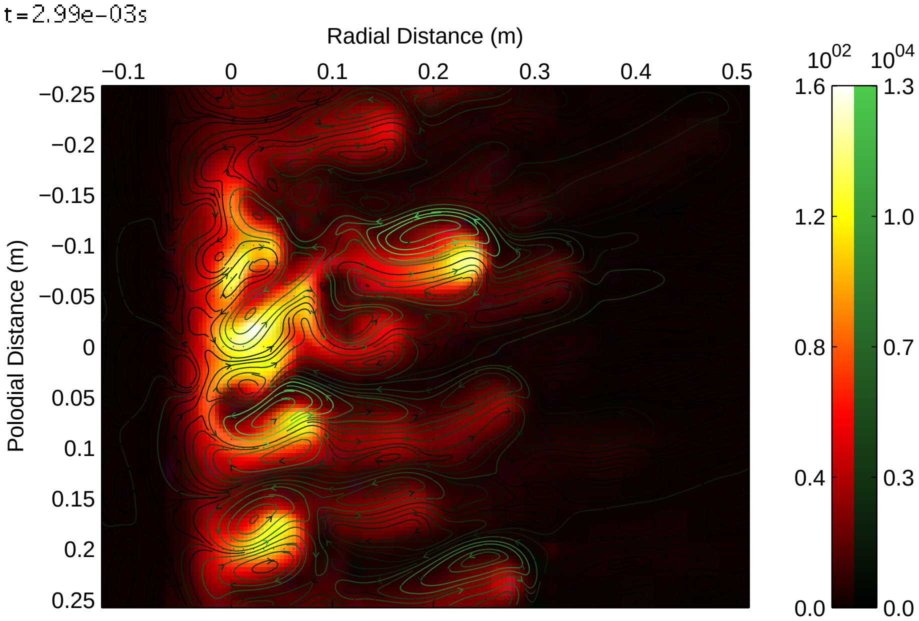

Figure 6.18: Snapshot of simulation SOL-SI-PS-FTI (6.34). Streamlines of velocity shown in green (kms^{-1}), plasma pressure shown in red-yellow (pA).

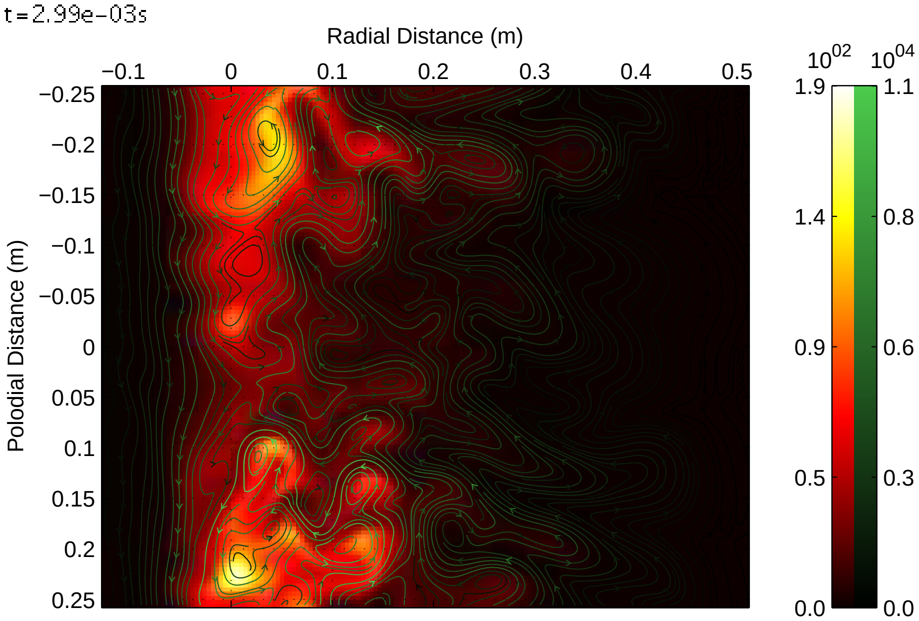

Figure 6.19: Snapshot of simulation SOL-SI-PS-FP3-FTI (6.36). Streamlines of velocity shown in green (kms^{-1}), plasma pressure shown in red-yellow (pA).

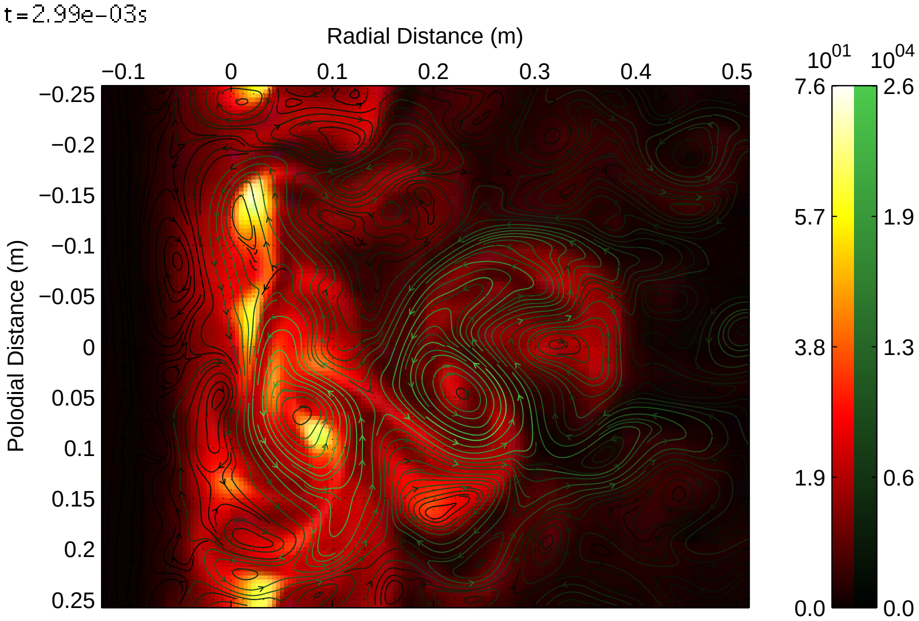

Figure 6.20: Snapshot of simulation SOL-CTI-PS-FTI (6.35). Streamlines of velocity shown in green (kms^{-1}), plasma pressure shown in red-yellow (pA).

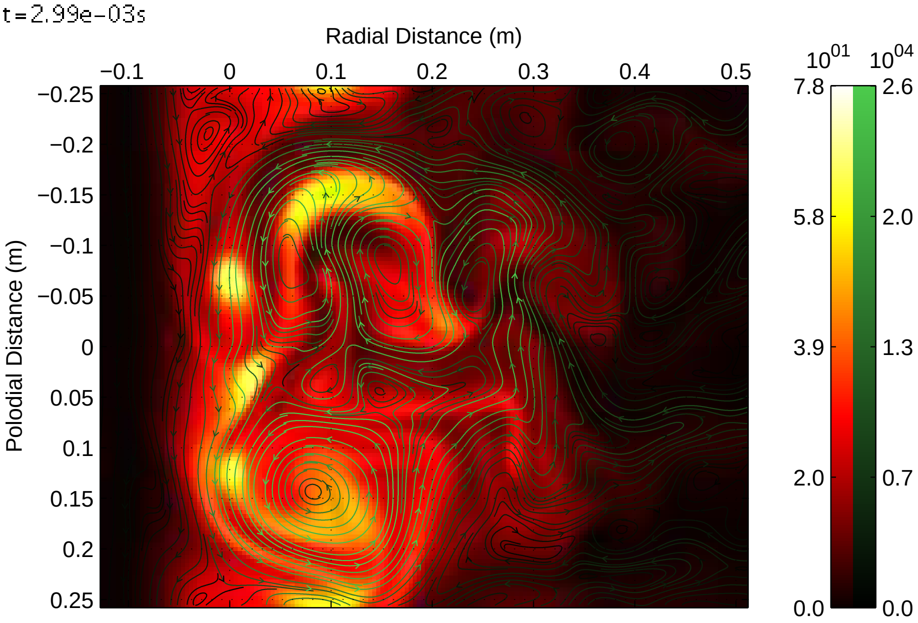

Figure 6.21: Snapshot of simulation SOL-CTI-PS-FP3-FTI (6.37). Streamlines of velocity shown in green (kms^{-1}), plasma pressure shown in red-yellow (pA).

6.4.1 SOL Widths

We may examine the effect of the parallel boundary conditions by looking at the plasma density and temperature of the simulation, averaged over the polodial direction and the duration of the simulation. From 6.22 it is evident that the finite ion temperature effects cause an increase in the radial transport, while the sheath potential drop causes a reduction in the radial transport. The constant target boundary conditions were seen to destabilise single blob structures in section 6.3, and, it was identified that the structure of the target quantities was more important than their magnitude, for determining the stability properties of the blob advection, however in all cases, finite ion temperature effects stabilised the blob. A single blob size was chosen in these investigations, whereas a wide range of structure sizes are present in the SOL simulations, and, the finite ion temperature stabilisation may be a function of the blob size.

Simulation SOL-CTI-PS-FTI (6.35) shows a much larger SOL width (w_{sol}) than SOL-SI-PS-FTI (6.34), and, SOL-CTI-PS-FP3-FTI (6.37) shows very little difference to SOL-CTI-PS-FTI (6.35), implying that the vortexes characteristic of the sheath potential drop are not being formed, or that they do not have enough stability to affect w_{sol}. Whereas the simulation SOL-SI-PS-FP3-FTI (6.36) shows a decrease in w_{sol} over SOL-SI-PS-FTI, indicative of reduction of radial transport due to the sheath potential drop.

It is not obvious if the invariance of w_{sol}, due to the suppression of sheath potential drop effects on w_{sol} between simulations SOL-CTI-PS-FTI (6.35) and SOL-CTI-PS-FP3-FTI (6.37) is due to the magnitude or structure of the target quantities. The spatial structure of SOL turbulence is not necessarily the same as it is for individual blobs, hence, the observed invariance may be simply due to the ideal interchange dominating over the sheath potential drop effects, as opposed to a destabilisation of individual blobs due to the spatial structure of the sheath current.

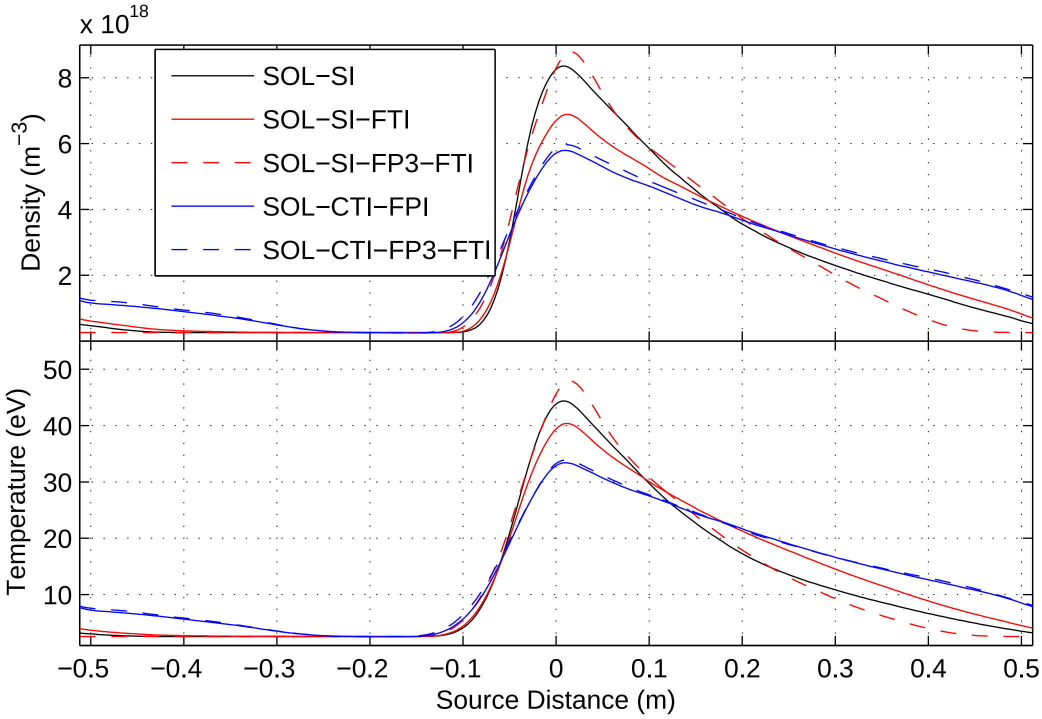

Figure 6.22: Averaged SOL profiles of density and temperature, showing the SOL width w_{sol}. Finite ion temperature effects increase w_{sol}, while the sheath potential drop decreases w_{sol}. SOL widths increase as target quantities are reduced as expected, and, sheath potential drop has little effect in the transition SOL-CTI-PS-FTI (6.35) to SOL-CTI-PS-FP3-FTI (6.37).

6.4.2 Flux and Phase Distributions

Here we examine the differences between the energy-particle flux, Γ_E, and the phase difference between density and velocity estimated by the peak-phase method 4.2 when floating potential $\phi_f = \phi_p - \Lambda$ is used to calculate the radial velocity instead of the plasma potential ϕ_p.

For all simulated SOL plasmas, there are three quantities that do not change, these are, an over-estimation of the radial flux as measured using floating potential by a factor of approximately two, a phase difference θ_{nv} measured using floating potential that peaks at approximately -30° and a real phase difference θ_{nv} that peaks at approximately 0°. These measurements of phase difference are approximately in agreement with the predictions of chapter 4.

Simulation SOL-SI-PS

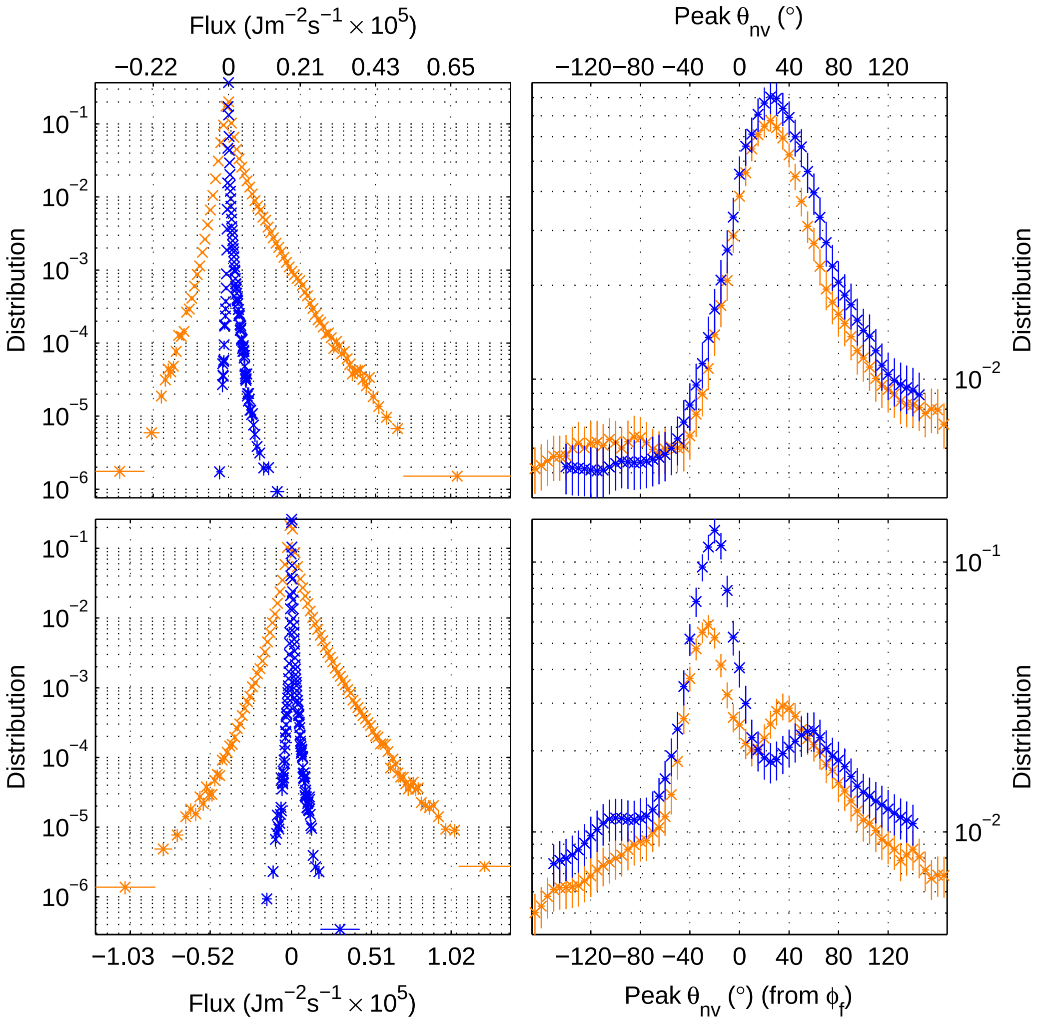

Figure 6.23: Simulation Designation: SOL-SI-PS (6.33), Parallel Model = Flute, Sheath Potential Drop = 0, Ion Temperature = 0. Red lined distributions are averaged over the near SOL ($0m$ to $0.128m$), blue lined distributions are averaged over the far SOL ($0.128m$ to $0.256m$).

Simulation SOL-SI-PS-FTI

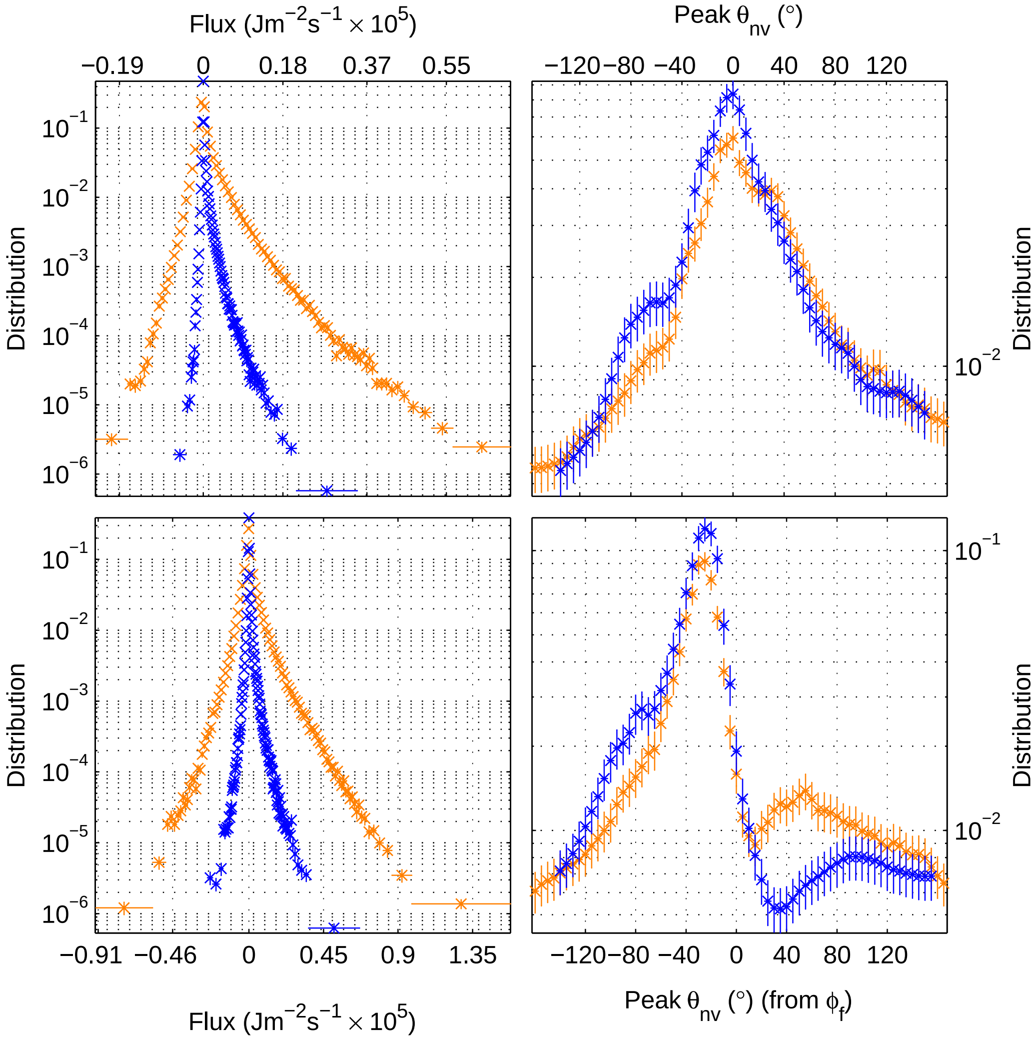

Figure 6.24: Simulation Designation: SOL-SI-PS-FTI (6.34), Parallel Model = Flute, Sheath Potential Drop = 0, Ion Temperature = Electron Temperature. Red lined distributions are averaged over the near SOL ($0m$ to $0.128m$), blue lined distributions are averaged over the far SOL ($0.128m$ to $0.256m$).

Simulation SOL-SI-PS-FP3-FTI

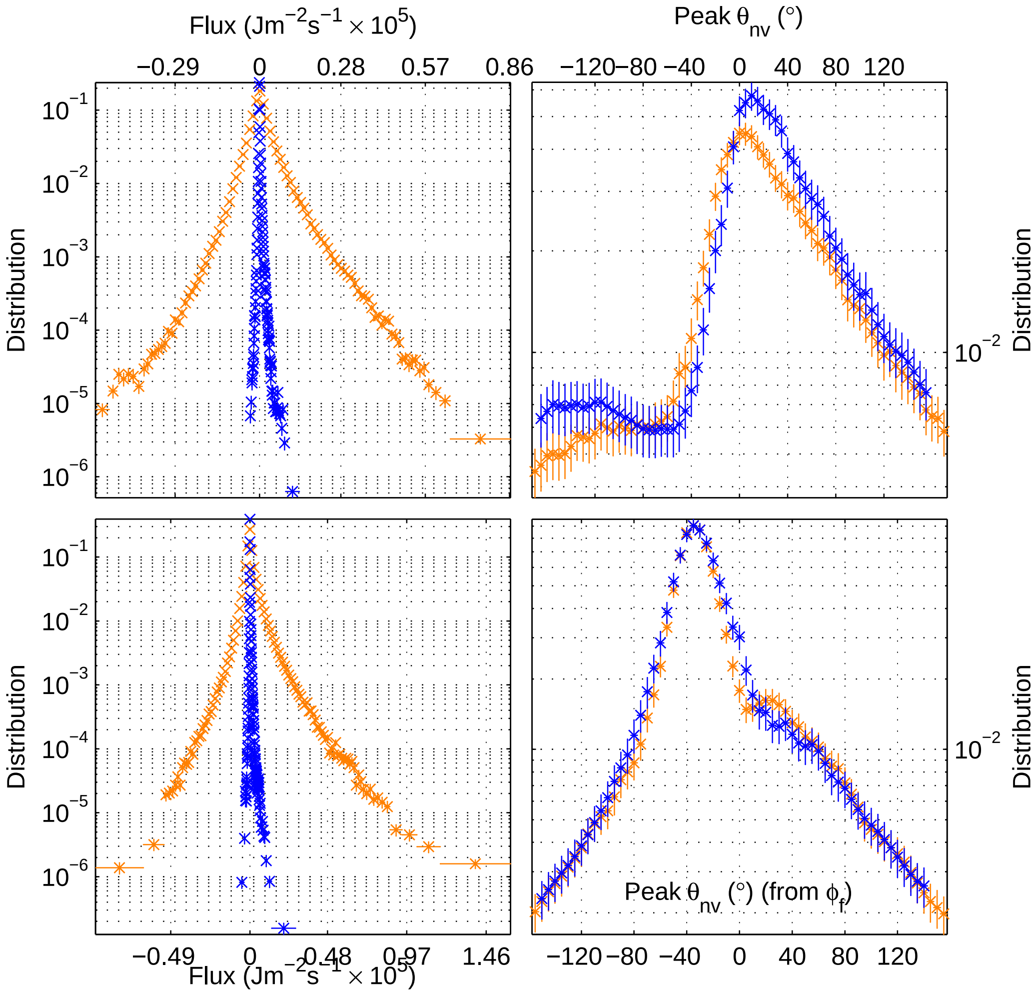

Figure 6.25: Simulation Designation: SOL-SI-PS-FP3-FTI (6.36), Parallel Model = Flute, Sheath Potential Drop = $3.0\frac{T_e}{e}$, Ion Temperature = Electron Temperature. Red lined distributions are averaged over the near SOL ($0m$ to $0.128m$), blue lined distributions are averaged over the far SOL ($0.128m$ to $0.256m$).

Simulation SOL-CTI-PS-FTI

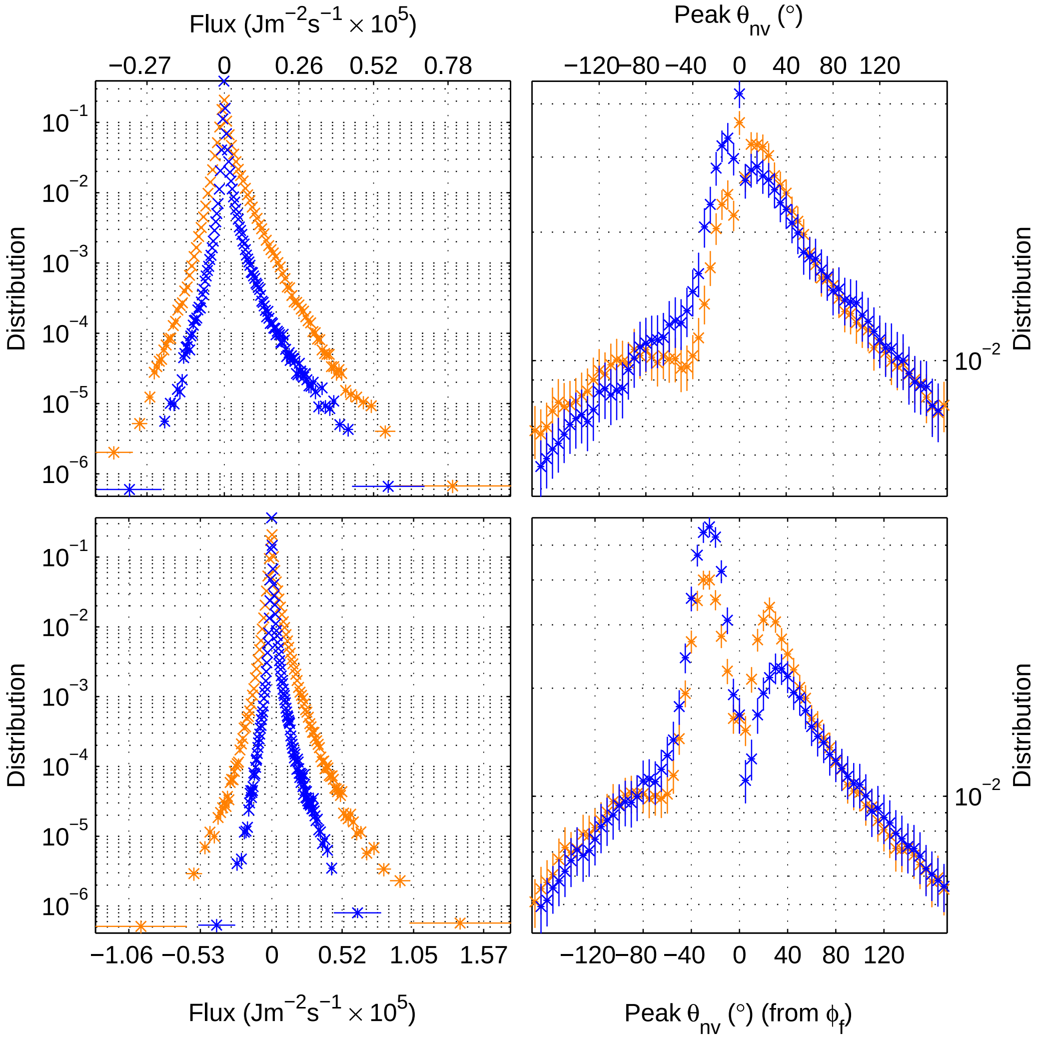

Figure 6.26: Simulation Designation: SOL-CTI-PS-FTI (6.35), Parallel Model = Constant Target, Sheath Potential Drop = 0, Ion Temperature = Electron Temperature. Red lined distributions are averaged over the near SOL ($0m$ to $0.128m$), blue lined distributions are averaged over the far SOL ($0.128m$ to $0.256m$).

Simulation SOL-CTI-PS-FP3-FTI

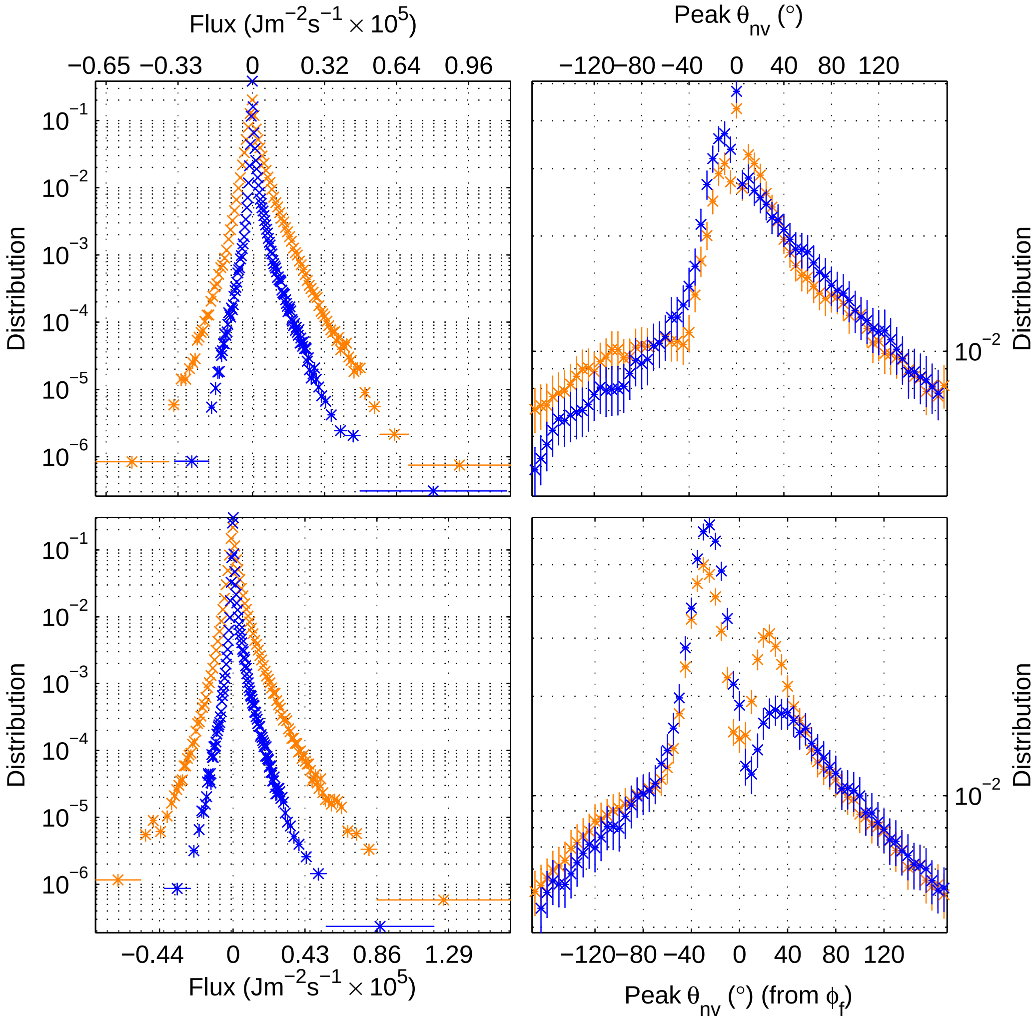

Figure 6.27: Simulation Designation: SOL-CTI-PS-FP3-FTI (6.37), Parallel Model = Constant Target, Sheath Potential Drop = $3.0\frac{T_e}{e}$, Ion Temperature = Electron Temperature. Red lined distributions are averaged over the near SOL ($0m$ to $0.128m$), blue lined distributions are averaged over the far SOL ($0.128m$ to $0.256m$).

6.4.3 HAWK Simulations of edge θ_{nv}

As a comparison to SOL phase differences simulated by the hTOKER code, data from the Hasegawa-Wakatani model HAWK Dewhurst et al. [2009], model equations (2.84) and (2.85), where the reader is reminded that $C = -\frac{\partial \ln B}{\partial x}$ is the curvature parameter. is taken with the effect of curvature included and neglected, and, RMS and peak phase distributions are then determined. The two measures of the phase difference of density and velocity give quite different results, however, it is clear that for the peak phase method, there is detected a very large swing toward zero θ_{nv} activity when the effect of curvature is included. While the structure of the θ_{nv} distribution is very different to the experimentally measured ones of 4.3, it does demonstrate the increased and indeed dominant zero phase activity visible in the peak phase results when curvature effects are included. Similar results are not recovered in the RMS method, and although it is not clear what the reason for this is, it could be due to the exclusive nature of the peak phase method, which weights heavily any peaked activity, which, the RMS method does not.

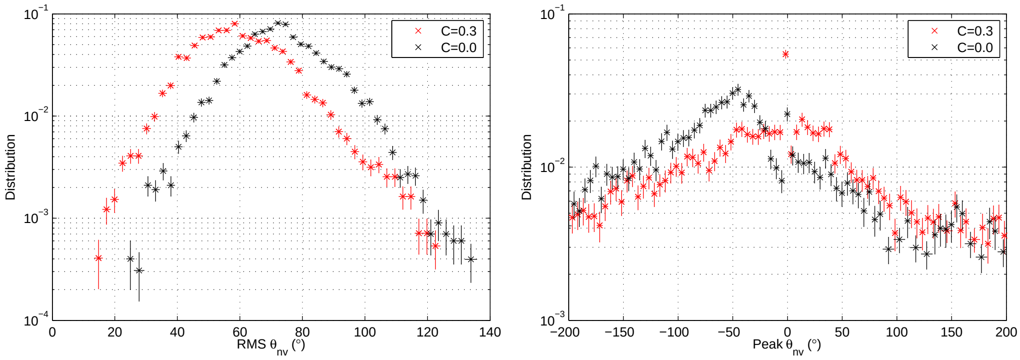

Figure 6.28: (left) Distribution of RMS phase in HAWK data with interchange term on or off. Phase calculated in the polodial y direction, and binned for each timestep. Distribution moved toward zero when curvature effects were included. (right) Peak phase distribution of HAWK data with interchange term of or off. Phase calculated from time series at a single point.

6.5 Summary

In this chapter we have used the hTOKER numerical model, derived in chapter 2, to evaluate the effects of the sheath potential drop and finite ion temperature, on the vorticity generated by both individual blobs, and by full SOL simulations. A subgrid model is employed based on the parametrised eddy viscosity of [Smith and Hammett, 1997], allowing the simulation to run at a grid spacing above the ion Larmor radius (which it must in order to preserve the validity of the model), while retaining a physical realisation of the turbulent cascade through the wavenumber associated with the grid spacing.

We examine the differences between the constant target (CT) and flute mode (SI) boundary conditions (6.18) to (6.32). The CT conditions remove spatial structure and reduce the magnitude by a factor ~ 10 of the sheath terms in the vorticity equation, compared to the SI conditions. The CT conditions tend to destabilise individual blobs compared to the SI conditions, in the case of cold ions and an active sheath potential drop. Warm ions in all cases are found to be stabilising to the blob structure, and to produce a polodial velocity in the structure; these effects are also observed in gyro-fluid simulations of blob interchange [Madsen et al., 2011]. Although the most obvious effect of the CT conditions, since sheath currents generally act to reduce vorticity to values set by the sheath potential drop, is to increase the strength of the plasma interchange and associated turbulence, the destabilisation in the CT case of blobs rotating with the sheath potential drop is found to be primarily due to the spatial structure of the sheath term.

SOL simulations (6.33) to (6.37) show that the stabilising effect of finite ion temperature effects leads to an increase SOL width in the SI case, and the sheath potential drop leads to a reduction of SOL width in the SI case. In the CT case, SOL widths are significantly larger, and, no change in SOL width is observed due to the sheath potential drop. We find that measurements of the radial flux using floating potential measurements tends to overestimate the values by a factor of ~ 2 for the simulated cases. Phase differences between density and radial velocity are evaluated in each case and found to peak strongly at $0°$, while in the case of a radial velocity approximated by the floating potential, the peak is found at $\sim -30°$; these phase measurements agrees with the results of chapter 3. Since the effort of chapter 3 was to differentiate between drift and interchange activity in the analysed datasets, we provide measurements using the standard RMS phase method 4.6 and the peak phase method 4.8 for the HAWK code [Dewhurst et al., 2009]. We find that without curvature terms, the phase difference peaks very broadly at $50°$. The sign has been reversed since the flow is in the electron diamagnetic direction in the code, but it is in the ion diamagnetic direction in the analysed MAST data of chapter 3. However, when activating the interchange effects in the HAWK code, results for the peak phase are extremely strongly peaked at $0°$, which is again in agreement with the results of chapter 3.

Chapter 7

Conclusions

Determining the causes of wear to plasma facing devices during tokamak plasma discharges is a key physics challenge for understanding, and optimising, the performance of future devices [Loarte et al., 2007]. Any plasma impinging on the material surfaces of a tokamak must first travel through the scrape off layer, and, there is a considerable body of evidence to support the idea that coherent filaments of plasma, with density and temperature considerably larger than their surroundings in the plane perpendicular to the magnetic field and elongated along the magnetic field, are responsible for the bulk of the wear [D'Ippolito et al., 2011]. This wear occurs in two distinct dimensions, firstly, dissipative flows along the to the material surfaces known as "divertors" or "limiters" (or often, "target plate") along filament axis, and secondly, advective flows of the filament structure away from the core plasma toward the material surface known as the "first wall". The advective transport toward the first wall in the plane perpendicular to the magnetic field is often refereed to a "blob" transport, and, the advective properties of these structures has a direct impact on the fluxes that cause wear to the material surfaces; this thesis is concerned with these advective properties.

7.1 Results

Linear theory of plasma interchange and drift waves give distinct predictions for the phase difference between density and radial velocity fluctuations, which if measurable, offers an ideal measure to discriminate between the active physics at play. The use of such measurements of this phase are complicated by violations of the local approximation used in the linear theory and further obscured when using the typically available floating potential diagnostic to determine the plasma velocity. In chapter

3 we tackle these issues by quantifying the effects using simple predictive modelling, and, developing peak detection methodology that makes best use of the predictive models and the available data from the MAST tokamak. Ideal interchange activity is detected in the SOL in two cases, one of which appears with the a predicted shift due to floating potential measurements, while another appears to have no shift at all. Interchange activity is also strongly indicated in the edge region. Examining inward velocity pulses reveals a phase structure that is characteristic of sheath limited blob advection mechanisms.

Blob advection mechanisms give differing predictions for the radial velocity based on the parameters of the blob. We take advantage of the parametric differences in plasma density of the advective models of chapter 2. For two plasma discharges with differing density, we determine the statistical change in the blob velocity relative to the blob density, using the peak detection method developed in chapter 3 which is most appropriate for comparing the blob models to the data. Results give the scaling index α as a function of the radial direction. The index appears in terms of the advective models as $v = n^{\alpha}$ from which each model takes a distinct value of α, and, the results give α corresponding to different models depending on the radial distance. In particular, the sheath limited model with constant target density developed in chapter 2, giving $\alpha = 1$ is found in the scaling results for radii in the SOL very near the LCFS. MAST plasmas are simulated in chapter 5 using the TOKER equations that treat the constant target density case for a variety of plasma powers, in order to investigate the effect of measuring the α index with the pin separation of the probe used on MAST. Values of α are found to differ very weakly between the ideal pin separation and the one used on MAST. For the range of simulations the α index is found to strongly depend on the input plasma power, however, the experimental scaling result is reproduced for some parameters. These results are published in [Higgins et al., 2012].

The hTOKER model developed in chapter 2 is numerically implemented in chapter 6. Unlike the isothermal counterpart TOKER, dissipation scales are generally smaller than the ion Larmor radius. Electric field and gyro-centre density are assumed to be the same concept for both electrons and ions in the two-fluid theory developed in chapter 2, which is only valid when collisional dissipation occurs at scales larger than the ion Larmor radius. This problem is tackled by employing a subgrid model that terminates the simulated fluctuations at a scale larger than the ion Larmor radius, while retaining a spectral characteristic identical to the fully resolved counterpart. The spectral index for the dissipation, as well as the basis for the model, is taken from the investigation [Smith and Hammett, 1997] which addresses finite Larmor radius drift-wave turbulence, which we find to be sufficient to stabilise simulations run with grid spacing of the order of the ion Larmor radius. Effects of neoclassical diffusion, sheath potential drop and finite ion temperature effects, and, their interactions with the constant target plasma model are investigated. It is found that the constant target plasma boundary condition may destabilise blobs that are otherwise stable under flute mode boundary conditions, and, that the destabilisation occurs as a result of the change in structure of the target quantities as opposed to the change in magnitude. However, finite ion temperature effects are able to stabilise these blobs in all of the investigated cases. Long term simulations of SOL plasmas are performed for a range of the same effects, and, we take advantage of the evolved electron temperature to study the effect of measuring the plasma fluxes and the phase difference of density and velocity using the floating potential (which, is affected by electron temperature as well as plasma potential). Fluxes are found to be overestimated by floating potential measurements by a factor of two in the simulated plasmas. Phase differences are found to vary only slightly between models, and, for floating potential derived phases to give a peak at approximately $-40°$, while the real phase peaks at approximately $0°$. Phase measurements are additionally made using the HAWK model [Dewhurst et al., 2009] with interchange enabled/disabled, and, with enabled interchange terms the phase is found to peak strongly at $0°$, indicative of strong interchange activity.

Bibliography

Justin R. Angus, Sergei I. Krasheninnikov, and Maxim V. Umansky. Effects of parallel electron dynamics on plasma blob transport. *Phys. Plasmas*, 19(8):082312, 2012. doi: 10.1063/1.4747619.

Akio Arakawa. Computational design for long-term numerical integration of the equations of fluid motion: Two-dimensional incompressible flow. part i. *Journal of Computational Physics*, 1(1):119 – 143, 1966. doi: 10.1016/0021-9991(66)90015-5.

N Ben Ayed, A Kirk, B Dudson, S Tallents, R G L Vann, H R Wilson, and the MAST team. Inter-elm filaments and turbulent transport in the mega-amp spherical tokamak. *Plasma Physics and Controlled Fusion*, 51(3):035016, 2009. doi: 10.1088/0741-3335/51/3/035016.

D. Bohm. *The Characteristics of Electrical Discharges in Magnetic Fields.* New York: MacGraw-Hill, 1949.

S. I. Braginskii. Transport processes in a plasma. *Reviews of Plasma Physics*, 1: 205, 1965.

B. A. Carreras, C. Hidalgo, E. Sánchez, M. A. Pedrosa, R. Balbín, I. García-Cortés, B. van Milligen, D. E. Newman, and V. E. Lynch. Fluctuation-induced flux at the plasma edge in toroidal devices. *Phys. Plasmas*, 3(7):2664–2672, 1996. doi: 10.1063/1.871523.

Zuoyang Chang and J. D. Callen. Generalized gyroviscous force and its effect on the momentum balance equation. *Physics of Fluids B: Plasma Physics*, 4(7):1766–1771, 1992. doi: 10.1063/1.860032. URL `http://0-link.aip.org.pugwash.lib.warwick.ac.uk/link/?PFB/4/1766/1`.

J. M. Dewhurst, B. Hnat, and R. O. Dendy. The effects of nonuniform magnetic field strength on density flux and test particle transport in drift wave turbulence. *Phys. Plasmas*, 16(7):072306, 2009. doi: 10.1063/1.3177382.

D. A. D'Ippolito, J. R. Myra, and S. J. Zweben. Convective transport by intermittent blob-filaments: Comparison of theory and experiment. *Physics of Plasmas*, 18(6): 060501, 2011. doi: 10.1063/1.3594609.

M. Frigo and S. G. Johnson. The design and implementation of FFTW3. *Proceedings of the IEEE*, 93(2):216–231, 2005. doi: 10.1109/JPROC.2004.840301.

Uriel Frisch. *Turbulence: The Legacy of A. N. Kolmogorov.* Cambridge University Press, 1995.

W. Fundamenski, O.E. Garcia, V. Naulin, R.A. Pitts, A.H. Nielsen, J. Juul Rasmussen, J. Horacek, J.P. Graves, and JET EFDA contributors. Dissipative processes in interchange driven scrape-off layer turbulence. *Nuclear Fusion*, 47(5): 417, 2007. doi: 10.1088/0029-5515/47/5/006.

I Furno, C Theiler, D Lanon, A Fasoli, D Iraji, P Ricci, M Spolaore, and N Vianello. Blob current structures in torpex plasmas: experimental measurements and numerical simulations. *Plasma Phys. Control. Fusion*, 53(12):124016, 2011.

O E Garcia. Collective motions in non-uniformly magnetized plasmas. *Eur. J. Phys.*, 24(331), 2003. doi: 10.1088/0143-0807/24/4/351.

O E Garcia. Blob transport in the plasma edge: a review. *Plasma and Fusion Research*, 4(019), 2009. doi: 10.1585/pfr.4.019.

O. E. Garcia, V. Naulin, A. H. Nielsen, and J. Juul Rasmussen. Turbulence and intermittent transport at the boundary of magnetized plasmas. *Phys. Plasmas*, 12(6):062309, 2005. doi: 10.1063/1.1925617.

O. E. Garcia, N. H. Bian, and W. Fundamenski. Radial interchange motions of plasma filaments. *Phys. Plasmas*, 13(8):082309, 2006a. doi: 10.1063/1.2336422.

O E Garcia, J Horacek, R A Pitts, A H Nielsen, W Fundamenski, J P Graves, V Naulin, and J Juul Rasmussen. Interchange turbulence in the tcv scrape-off layer. *Plasma Phys. Control. Fusion*, 48(1):L1, 2006b.

Akira Hasegawa and Masahiro Wakatani. Plasma edge turbulence. *Phys. Rev. Lett.*, 50:682–686, 1983. doi: 10.1103/PhysRevLett.50.682.

P. Helander and D. J. Sigmar. *Collisional Transport in Magnetized Plasmas.* New York: Cambridge University Press, 2002.

D Higgins, B Hnat, A Kirk, P Tamain, N Ben Ayed, and the MAST Team. Determining advection mechanism of plasma filaments in the scrape-off layer of mast. *Plasma Phys. Control. Fusion*, 54(1):015002, 2012.

W. Horton. Drift waves and transport. *Rev. Mod. Phys.*, 71:735–778, Apr 1999. doi: 10.1103/RevModPhys.71.735.

J. D. Huba. NRL plasma formulary. Naval Research Laboratory, Washington, D.C., 2006.

S. S. Krasheninnikov, D. A. D'Ippolito, and J. R. Myra. Recent theoretical progress in understanding coherent structures in edge and sol turbulence. *Journal of Plasma Physics*, 74(05):679–717, 2008. doi: 10.1017/S0022377807006940.

S.I. Krasheninnikov. On scrape off layer plasma transport. *Phys. Lett.A*, 283(56): 368 – 370, 2001. ISSN 0375-9601. doi: 10.1016/S0375-9601(01)00252-3.

R. Kube and O. E. Garcia. Velocity scaling for filament motion in scrape-off layer plasmas. *Phys. Plasmas*, 18(10):102314, 2011. doi: 10.1063/1.3647553.

L.D. Landau. On the vibrations of the electronic plasma. *J.Phys.(USSR)*, 10:25–34, 1946.

B. Lloyd, J-W. Ahn, R.J. Akers, L.C. Appel, E.R. Arends, K.B. Axon, R.J. Buttery, C. Byrom, P.G. Carolan, C. Challis, D. Ciric, N.J. Conway, M. Cox, G.F. Counsell, G. Cunningham, A. Darke, A. Dnestrovskij, J. Dowling, M.R. Dunstan, A.R. Field, S.J. Fielding, S. Gee, M.P. Gryaznevich, P. Helander, M. Hole, M.B. Hood, P.A. Jones, A. Kirk, I.P. Lehane, G.P. Maddison, S.J. Manhood, R. Martin, G.J. McArdle, K.G. McClements, M.A. McGrath, H. Meyer, A.W. Morris, S.K. Nielsen, M. Nightingale, A. Patel, T. Pinfold, M.N. Price, J. Qin, C. Ribeiro, C.M. Roach, D.C. Robinson, O. Sauter, V. Shevchenko, S. Shibaev, K. Stammers, A. Sykes, A. Tabasso, D. Taylor, M.R. Tournianski, G. Turri, M. Valovic, G. Voss, M.J. Walsh, S. Warder, J.R. Watkins, H.R. Wilson, Y. Yang, S. You, the MAST, and NBI teams. Overview of recent experimental results on mast. *Nuclear Fusion*, 43(12):1665, 2003.

A. Loarte, B. Lipschultz, A.S. Kukushkin, G.F. Matthews, P.C. Stangeby, N. Asakura, G.F. Counsell, G. Federici, A. Kallenbach, K. Krieger, A. Mahdavi, V. Philipps, D. Reiter, J. Roth, J. Strachan, D. Whyte, R. Doerner, T. Eich, W. Fundamenski, A. Herrmann, M. Fenstermacher, P. Ghendrih, M. Groth,

A. Kirschner, S. Konoshima, B. LaBombard, P. Lang, A.W. Leonard, P. Monier-Garbet, R. Neu, H. Pacher, B. Pegourie, R.A. Pitts, S. Takamura, J. Terry, E. Tsitrone, the ITPA Scrape-off Layer, and Divertor Physics Topical Group. Chapter 4: Power and particle control. *Nuclear Fusion*, 47(6):S203, 2007.

Cyrus S. MacLatchy, Claude Boucher, Deborah A. Poirier, and James Gunn. Gundestrup: A langmuir/mach probe array for measuring flows in the scrape-off layer of tdev. *Review of Scientific Instruments*, 63(8):3923–3929, 1992. doi: 10.1063/1.1143239.

Jens Madsen, Odd E. Garcia, Jeppe Stærk Larsen, Volker Naulin, Anders H. Nielsen, and Jens Juul Rasmussen. The influence of finite larmor radius effects on the radial interchange motions of plasma filaments. *Physics of Plasmas*, 18(11):112504, 2011. doi: 10.1063/1.3658033.

K. Miyamoto. *Controlled Fusion And Plasma Physics*. Series in Plasma Physics Series. CRC PressINC, 2007. ISBN 9781584887096.

MPI Forum. Message Passing Interface (MPI) Forum Home Page. `http://www.mpi-forum.org/` (Dec. 2012).

J. R. Myra, D. A. D'Ippolito, S. I. Krasheninnikov, and G. Q. Yu. Convective transport in the scrape-off-layer by nonthermalized spinning blobs. *Physics of Plasmas*, 11(9):4267, 2004. doi: 10.1063/1.1774168.

W.H. Press. *Numerical recipes in C: the art of scientific computing*. Numerical recipes series. Cambridge University Press, 1992. ISBN 0521431085.

K U Riemann. The bohm criterion and sheath formation. *Journal of Physics D: Applied Physics*, 24(4):493, 1991. doi: 10.1088/0022-3727/24/4/001.

V Rozhansky and A Kirk. Possible mechanism for filament motion in the sol of a tokamak. *Plasma Physics and Controlled Fusion*, 50(2):025008, 2008.

E. Sánchez, C. Hidalgo, D. López-Bruna, I. García-Cortés, R. Balbín, M. A. Pedrosa, B. van Milligen, C. Riccardi, G. Chiodini, J. Bleuel, M. Endler, B. A. Carreras, and D. E. Newman. Statistical characterization of fluctuation wave forms in the boundary region of fusion and nonfusion plasmas. *Physics of Plasmas*, 7(5):1408–1416, 2000. doi: 10.1063/1.873958.

Y. Sarazin and Ph. Ghendrih. Intermittent particle transport in two-dimensional edge turbulence. *Physics of Plasmas*, 5(12):4214–4228, 1998. doi: 10.1063/1.873157.

S. A. Smith and G. W. Hammett. Eddy viscosity and hyperviscosity in spectral simulations of 2d drift wave turbulence. *Physics of Plasmas*, 4(4):978–990, 1997. doi: 10.1063/1.872210.

Satoru Sugita, Masatoshi Yagi, Sanae-I. Itoh, and Kimitaka Itoh. Bohm-like dependence of transport in scrape-off layer plasmas. *J. Phys. Soc. Japan*, 81(4):044501, 2012. doi: 10.1143/JPSJ.81.044501.

P Tamain, A Kirk, E Nardon, B Dudson, B Hnat, and the MAST team. Edge turbulence and flows in the presence of resonant magnetic perturbations on mast. *Plasma Physics and Controlled Fusion*, 52(7):075017, 2010. doi: 10.1088/0741-3335/52/7/075017.

D. Tskhakaya, F. Subba, X. Bonnin, D. P. Coster, W. Fundamenski, R. A. Pitts, and JET EFDA Contributors. On kinetic effects during parallel transport in the sol. *Contributions to Plasma Physics*, 48(1-3):89–93, 2008. doi: 10.1002/ctpp.200810015.

Y. Uesugi, K. Hoshino, T. Yamamoto, H. Kawashima, S. Kasai, T. Kawakami, M. Maeno, T. Matoba, T. Matsuda, H. Matsumoto, Y. Miura, M. Mori, K. Odajima, H. Ogawa, T. Ogawa, K. Ota, H. Ohtsuka, S. Sengoku, T. Shoji, N. Suzuki, H. Tamai, S. Yamamoto, T. Yamauchi, and I. Yanagisawa. Control of plasma current during lower hybrid current drive in the jft-2m tokamak. *Nuclear Fusion*, 25(11):1611, 1985. doi: 10.1088/0029-5515/25/11/008.

M. J. Walsh, E. R. Arends, P. G. Carolan, M. R. Dunstan, M. J. Forrest, S. K. Nielsen, and R. O'Gorman. Combined visible and infrared thomson scattering on the mast experiment. *Review of Scientific Instruments*, 74(3):1663, 2003. doi: 10.1063/1.1537882.

J. Weiland. *Collective Modes in Inhomogeneous Plasma: Kinetic and Advanced Fluid Theory*. Plasma Physics Series. Inst. of Physics Publ., 2000. ISBN 9780750305891.

J Wesson. *Tokamaks*. Oxford University Press,New York, NY, 1987.

G.S. Xu, V. Naulin, W. Fundamenski, C. Hidalgo, J.A. Alonso, C. Silva, B. Gonalves, A.H. Nielsen, J. Juul Rasmussen, S.I. Krasheninnikov, B.N. Wan, M. Stamp, and JET EFDA Contributors. Blob/hole formation and zonal-flow generation in the edge plasma of the jet tokamak. *Nuclear Fusion*, 49(9):092002, 2009. doi: 10.1088/0029-5515/49/9/092002.

G. Q. Yu, S. I. Krasheninnikov, and P. N. Guzdar. Two-dimensional modelling of blob dynamics in tokamak edge plasmas. *Phys. Plasmas*, 13(4):042508, 2006. doi: 10.1063/1.2193087.